VIBRATION SUPPRESSION IN A PLATE USING IN-PLANE FORCES

By

Mahmoud Nabil Abdullatif

A THESIS

Submitted to
Michigan State University
in partial fulfillment of the requirements
for the degree of

Mechanical Engineering - Master of Science

2015

ABSTRACT

VIBRATION SUPPRESSION IN A PLATE
USING IN-PLANE FORCES

By

Mahmoud Nabil Abdullatif

Vibration suppression of flexible structures continues to be a subject of considerable interest due to the increasing demands of high precision space applications. Large phased array antennas, for example, which are used for space-based radar system to track and identify moving objects, require high dimensional stability. The Air Force is interested is exploiting tension mechanics in maintaining dimensional stability of large array structures. To this end, this research investigates the problem of vibration suppression in a thin plate using in-plane tensile forces acting on the boundary. Earlier work has shown that the vibration of a cantilever beam can be effectively suppressed by end-forces and this work investigates the extension of the control strategy to the plate problem. Two scenarios are considered: one where the end-forces are uniformly distributed, and the other where the end-forces are applied at discrete locations using a web-of-cables structure. For the problem with uniformly distributed end-forces, both the Rayleigh-Ritz method and the finite element method are used to obtain the state space model of the system in modal coordinates. Simulations are then used to show the efficacy of the control strategy in reducing vibration. The plate with web-of-cables structure is modeled using the finite element method alone. The effect of the web-of-cables structure on in-plane stress distribution in the plate is determined and the pre-stress information is used to obtain the out-of-plane vibration model. The control method requires the tension in the corner cables of the web-of-cable structure to be switched and the efficacy of the control method is investigated for different switching algorithms. Numerical simulations for these different algorithms show that the control method is effective in suppressing the vibration of all modes except the first mode. This is due to the fact that change in the corner tensions is not effective in producing a significant change in the fundamental frequency. To suppress the vibration of the first mode, future work will have to focus on redesign of the web-of-cables structure relative to the plate dimensions.

TABLE OF CONTENTS

LIST OF TABLES

LIST OF FIGURES

Chapter 1

Introduction

Vibration suppression of flexible structures has been investigated for decades due to its widespread engineering applications. The objective of vibration suppression is to prevent the structure from being damaged or prevent compromising its desired usability. Space structures, which may undergo vibration due to differential heating, can be seriously limited in their ability to acquire images. Therefore, it is desirable to suppress the undesired vibration and stabilize the space structure motions. Vibration suppression of flexible structures is an active field to research and various methods have been proposed to address the problem.

1.1. Motivation

Vibration suppression of space structure has become an important problem due to the increasing demand of high precision space applications. To reduce the payload, space structures are desired to have low mass and therefore low rigidity. In general, space structures are characterized by low damping; therefore, they are highly sensitive to external disturbances and are prone to

mechanical vibrations. Consequently, elimination or reduction of structural vibration has been extensively studied; these studies have focused on disturbance rejection controllers, which can eliminate the structural vibrations. Both passive and active controllers have been proposed. In passive vibration suppression approach, passive elements are mounted on the structure to change the structural characteristics such as damping and stiffness. This method is effective for attenuation of high frequencies, but is not effective for suppression of low frequency vibration. In addition, it is expensive and it increases the overall structure weight, which is unfavorable for space applications. In contrast, active vibration controllers are based on feedback of the vibration in the structure. In traditional active vibration control, the structure is modeled as a linear system using modal coordinates; certain modes of the structure are estimated and controlled using piezoelectric actuators and sensors. For a large flexible structure, a large number of actuators and sensors are required, which means the addition of a large number of hardware components such as amplifiers and data acquisition devices. This hardware adds significant weight and cost to the structure. To reduce the hardware requirements of active vibration control, Nudehi [48] proposed to use end forces in a flexible beam. This thesis presents an extension of the work done in [48] to control the vibration of a rectangular plate using piezoelectric transducers as sensors to estimate the modal displacements and in-plane cables that act as actuators. These in-plane cables provide in-plane tensions that alter the structural stiffness. By switching in-plane forces, the modal energy can be reduced and the vibration of the structure can be suppressed.

1.2. Literature review

The problem of thin plate vibration has been studied for several decades. Most of these studies have focused on investigating the dynamic behavior of the structure for a certain restraint condition along the edges. Leissa [38], for instance, provided very useful and comprehensive review for the plate vibration with different type of boundary conditions. The first observation of nodal patterns for a flat square plate is done by the German physicist, Ernst Chladni (published in 1787 in his book "Discoveries in the Theory of Sound"), by conducting experiments using sand on vibrating plate. Several years later (in the early 1800s), a French mathematician (Sophie Germain) obtained a differential equation for transverse deformation on plates. Her equation had an error due to neglecting the strain energy associated with warping of the plate midplane. Langrange's notes, found in 1813, revealed the correct version of the governing equation for a thin plate. However, the differential equation of rectangular plates with flexural resistance is derived by Navier (1785 – 1836). Navier also obtained the exact solution for simply supported rectangular plates in 1820. In 1850, Kirchhoff found the extended plate theory by combining the bending and stretching actions of the plate. The natural frequencies of vibrating structures using single admissible function were obtained by Rayleigh (1877). Ritz (1909) improved Rayleigh's theory by including more than a single admissible function and performing a minimization with respect to the unknown coefficients of these admissible functions. He obtained an approximate solution of a freely vibrating plate, which does not have an exact solution. This method is known as the Rayleigh-Ritz method. Finite element methods were developed in the mid-1950s by Tuner, Clough, Martin, and Topp. Their method obtained the numerical solution of complex plate problems in an efficient way.

Plate modeling (vibration analysis) has been studied for various boundary conditions using deferent method (e.g., Williams, [33]; Zhou and Ji, [34]; Farrel and Ryall, [35]; Frendi and Raliss, [36]; Chien-Ching Ma, [27]; Israr, [22]; Werfalli and Karound, [29]; Gupta, [28]). Some of these results used FEM to obtain the numerical solution. The vibration of plate with elastic foundations is documented in the literature, for instance, Hsu, [24], and Hatami, [31]. The dynamics of flexible structures (beams and plates) have been investigated under the application of end forces; these include the work by: Herrmann, [12]; Celep, [1]; Sasaki and Chonan, [2]; Higuchi and Dowell, [3]; Adali, [4]; Zuo and Schreyer, [5]; Kim and Park, [9]; Kim and Park, [10]; Langthjem and Sugiyama, [6]; and Arreol-Lucas, [13]. Most of these results are related to flutter instability due to the effects of the follower forces that have non-conservative nature.

Vibration suppression of plates has been achieved using traditional methods (active and passive vibration control) and they are well documented in the literature. For instance, Shirazi and Owji [21] investigated the vibration control of simply supported plate. Carra and Ambilli [20] controlled the vibration of a rectangular aluminum plate in contact with air or water. Some of the vibration control methods and stability analysis are presented in the following references: Khorshidi, [14]; Djanan, [15]; Hu and Jia, [16]; Qiu, [17]; Kucuk, [18]; Falangas, [23]; Ashour, [25]; Kovarova, [26]; Yaman, [30]; and Braghin and Cinquemani [41]. Active vibration control is used in the most of these studies.

In general, cables are used to increase the stiffness of lightweight structures. However, using cables to control the vibration has not been studied extensively. Achire and Preument [37] introduced multiple control strategies to control the vibration in cable-stayed bridges. Preumont and Bossens [48] propose tendons to create an active damping in truss structures. Skidmore and Hallauer [7] used multiple-actuator theory to actively control individual vibration modes of

beam-cable structure. Nudehi [Ref] used a cable to apply an end-force on a cantilever beam to suppress the vibration. Sakamoto and Park [43] and [44] presented structural and controller designs to attenuate vibration in large membrane using web-like perimeter cables around they membrane. The control of deployment of space structures using web-like structure has been studied by Gärdsback and Tibert, [42]; Lane A Murphey, [45]; and Keon and Murphey, [46]. Greschik and Mejia-Ariza [47] presented a numerical and theoretical study of control out-of-plane flatness and thermal warping via suspension tensions. Following Nudehi's work [48], in-plane forces are used in this thesis to control the vibration of a rectangular plate. The approach is extended by applying the in-plane forces through a web-of-cables structure.

1.3. Scope and content

This thesis is organized as follows. In chapter 2, a brief review of the dynamics of a thin plate is presented. Following [39], the theory of the elastic plate is used to derive the equation of motion for a plate, with and without in-plane boundary forces. In chapter 3, some analytical and approximate solutions are obtained for a plate subjected to different types of in-plane forces. Chapter 4 introduces a control strategy, following the work presented by Nudehi [48], to reduce the lateral vibration on a plate. We assumed that the plate is subjected to uniformly distributed in-plane forces. In chapter 5 a web-of-cables around the plate is proposed as a mechanism to suppress the vibration. This web-of-cables provides the boundary of the plate with in-plane forces that act at few discrete locations. As a result, non-uniform stress distributions are created. Using the pre-stress data, an out-of-plane vibration analysis is done to obtain the dynamic model of the structure. Simulations are carried out to examine the efficacy of the control strategy.

Chapter 2

Dynamics Of A Thin Rectangular Plate – A Review

A plate is a structure that consists of two surfaces separated by a small distance. The small distance is called the thickness of the plate, which is assumed to be smaller than the other dimensions of the two surfaces, namely the length and the width of the plate. A plate is considered to be thin if the ratio of its thickness to the other dimensions is less than *1/20*. A two-dimensional approximation to the elasticity theory is called the theory of the elastic plate, which considers the deformation of every point in the plate in terms of the midplane deformation. The theory of the elastic plate is used to derive the equation of motion for a thin rectangular plate, with and without in-plane forces acting at the boundary.

2.1 Classical Plate Theory

The Cartesian coordinate system (*x, y* and *z*) is used to define the coordinates of a thin rectangular plate that has has a length *a*, width *b,* and thickness *h* as shown in Fig. 2.1. The displacements in the *x* and *y* direction are defined as *u* and *v* respectively, and the transverse deformation of the midplane is defined as *w.* The derivation of the equation of motion for the transverse vibration is based on the following assumptions [39]:

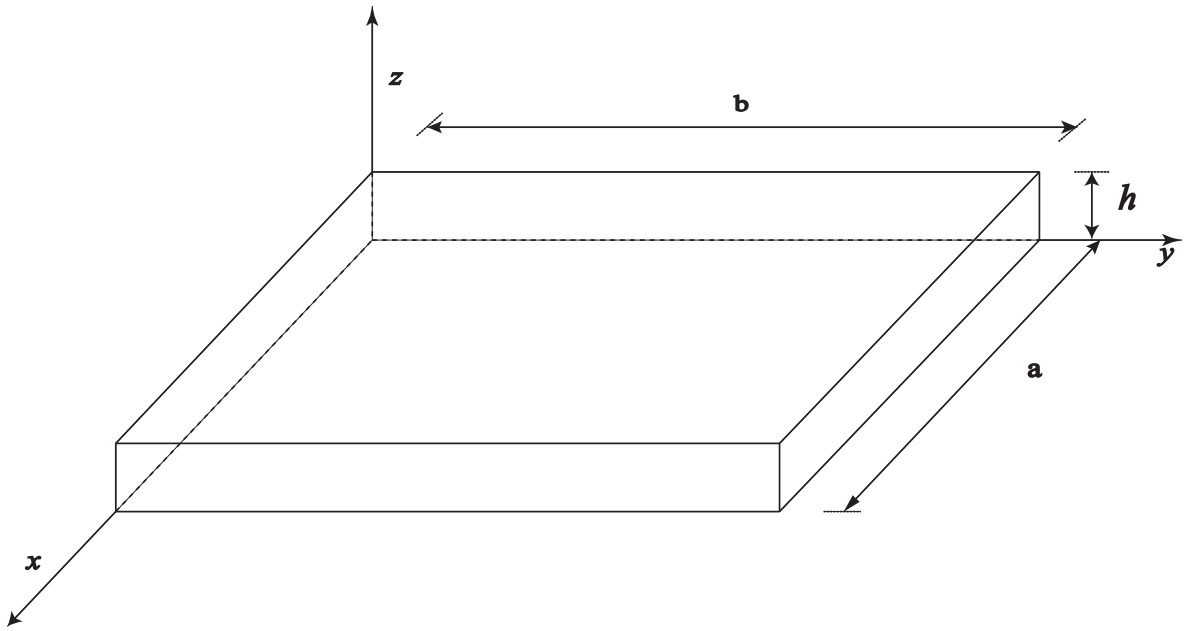

Figure 2.1. Thin Rectangular Plat

1. The thickness of the plate h is smaller than other physical dimensions, namely the length a and the width b; and usually the ratio of the thicknesses to the smaller dimension (length or width) is less than *1/20*.
2. The material of the plate is homogenous and linear elastic, and the stress-strain relationship follows Hooke's Law.
3. The midplane of the plate remains a neutral plane, i.e., the midplane does not experience stretching or contractions.
4. The transverse deformation of the midplane w is small compared to the thickness h.
5. The transverse shear deformation is negligible, i.e., a straight line normal to the midplane remains normal after the deformation. As a result, the transverse shear strains can be neglected.
6. The plate is assumed to have negligible rotary inertia.
7. The plate resists the in-plane forces through bending, and in-plane and out-of-plane displacement.

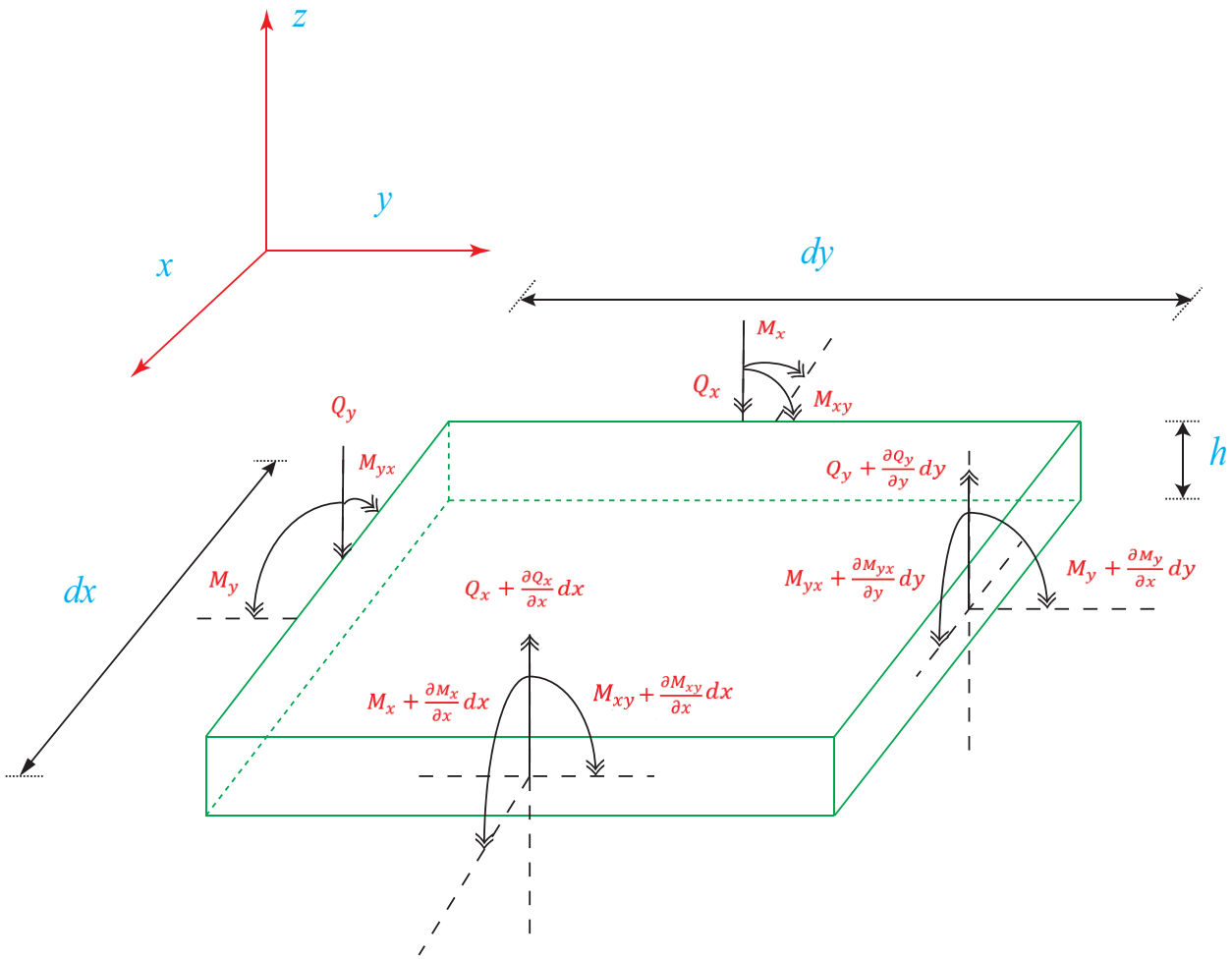

Figure 2.2. An infinitesimal element of the thin rectangular plate

Consider an infintismal element of the plate as shown in the Fig. 2.2, which has dimensions *dx, dy* and *h* in the *x*, *y* and *z* direction respectively. The element is subjected to bending moments, M_x and M_y, twisting moments, M_{xy} and M_{yx}, and shear forces, Q_x and Q_y due to internal stresses. M_x and M_y denote the bending moments per unit length about the *x* and *y* axes, respectively; M_{xy} and M_{yx} are the twisting moments per unit length about the *x* and *y* axes respectively and Q_x and Q_y are shear forces per unit length parallel to *y* and *x* axes respectively. Following the derivation in [39], the summation of the forces in the *z* direction yields

$$-Q_x\,dy + \left[Q_x + \frac{\partial Q_x}{\partial x}dx\right]dy - Q_y\,dx + \left[Q_y + \frac{\partial Q_y}{\partial y}dy\right]dy = \rho h\,dx\,dy\,\frac{\partial^2 w}{\partial t^2} \qquad (2.1)$$

where ρ is the density of the material of the plate. Dividing both sides by the area we get

$$\frac{\partial Q_x}{\partial x} + \frac{\partial Q_y}{\partial y} = \rho h \frac{\partial^2 w}{\partial t^2} \tag{2.2}$$

The sum of the moments of all the forces about the *y* axis gives

$$\begin{aligned} M_x dy - \left(M_x + \frac{\partial M_x}{\partial x} dx\right) dy + M_{yx} dx - \left(M_{yx} + \frac{\partial M_{yx}}{\partial y} dy\right) dx + Q_x dy \frac{dx}{2} \\ + \left(Q_x + \frac{\partial Q_x}{\partial x} dx\right) dy \frac{dx}{2} = \underbrace{\rho \left(\frac{h^3}{12} dx dy\right) \frac{\partial^2}{\partial t^2} \left(\frac{\partial W}{\partial x}\right)}_{inertia\ moment\ due\ to\ rotation} \end{aligned} \tag{2.3}$$

By dropping the inertia moment term (assumption 6), the equation can be reduced to

$$Q_x = \frac{\partial M_x}{\partial x} - \frac{\partial M_{yx}}{\partial y} \tag{2.4}$$

The sum of the moments about the *x* axis gives

$$\begin{aligned} M_y dx - \left(M_y + \frac{\partial M_y}{\partial x} dy\right) dx + M_{xy} dy + \left(M_{xy} + \frac{\partial M_{xy}}{\partial x} dx\right) dy + Q_y dx \frac{dy}{2} \\ + \left(Q_y + \frac{\partial Q_y}{\partial y} dy\right) dx \frac{dy}{2} = \underbrace{\rho \left(\frac{h^3}{12} dx dy\right) \frac{\partial^2}{\partial t^2} \left(\frac{\partial w}{\partial y}\right)}_{inertia\ moment\ due\ to\ rotation} \end{aligned} \tag{2.5}$$

and it can be reduced to

$$Q_y = \frac{\partial M_y}{\partial y} - \frac{\partial M_{xy}}{\partial x} \tag{2.6}$$

Following the method used in [39], the strain-displacement relationships are derived next. Assuming that the midplane is the *xy* plane, we consider the straight line AB oriented in the *z* direction normal to the midplane - see Fig. 2.3.

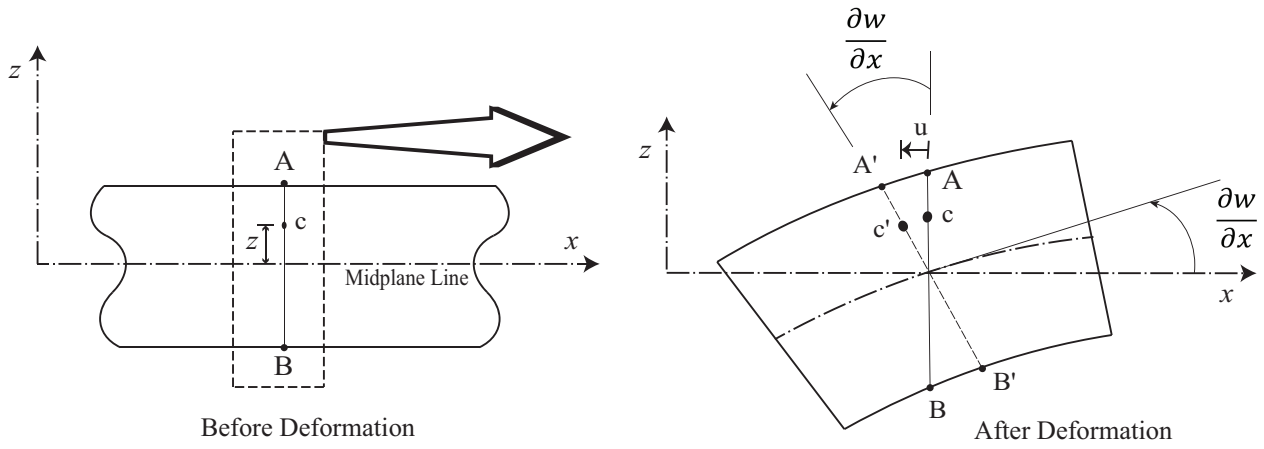

Figure 2.3. Rotation of a normal line after the deformation

After deformation, AB rotates to A′B′ due to bending and shear deformation. A point c at a distance *z* from the midplane on line AB will have a displacement u in the *x* direction after the deformation and could be defined as

$$u = -z\frac{\partial w}{\partial x} \tag{2.7}$$

where $(\partial w/\partial x)$ is the slope of the deformation surface in the *xz* plane. Similarlly, the displacement *v* in the *y* direction can be expressed

$$v = -z\frac{\partial w}{\partial y} \tag{2.8}$$

The normal strains using strain-displacement relationship can be defined as

$$\varepsilon_{xx} = \frac{\partial u}{\partial x}\,; \qquad \varepsilon_{yy} = \frac{\partial v}{\partial y} \tag{2.9}$$

The shear strain is

$$\varepsilon_{xy} = \frac{\partial v}{\partial x} + \frac{\partial u}{\partial y} \tag{2.10}$$

Substituting both Equations (2.7) and (2.8) into equations (2.9) and (2.10), we get

$$\varepsilon_{xx} = -z\frac{\partial^2 w}{\partial x^2}; \quad \varepsilon_{yy} = -z\frac{\partial^2 w}{\partial y^2}; \quad \varepsilon_{xy} = -2z\left(\frac{\partial^2 w}{\partial x \partial y}\right) \tag{2.11}$$

According to Hooke's law, the strain-stress relationship can be expressed as follows:

$$\varepsilon_{xx} = \frac{1}{E}\left(\sigma_{xx} - \sigma_{yy}\upsilon\right) \tag{2.12}$$

$$\varepsilon_{yy} = \frac{1}{E}\left(\sigma_{yy} - \sigma_{xx}\upsilon\right) \tag{2.13}$$

$$\varepsilon_{xy} = \frac{\tau_{xy}}{G} \tag{2.14}$$

where σ_{xx} and σ_{yy} are the normal stresses, τ_{xy} is the shear stress, and

$$G = \frac{E}{2(1+\upsilon)} \tag{2.15}$$

where G is the shear modulus, E is the Young Modulus and υ is the Poisson's ratio. Solving the above equations for the stresses results in

$$\sigma_{xx} = \frac{E}{(1-\upsilon^2)}\left(\varepsilon_{xx} + \upsilon\varepsilon_{yy}\right) \tag{2.16}$$

$$\sigma_{yy} = \frac{E}{(1-\upsilon^2)}\left(\varepsilon_{yy} + \upsilon\varepsilon_{xx}\right) \tag{2.17}$$

$$\tau_{xy} = \frac{E}{2(1+\upsilon)}\varepsilon_{xy} \tag{2.18}$$

By integrating the moment of the in-plane stresses over the plate thickness we get the bending and the twisting moments as follows:

$$M_x = \int_{-h/2}^{h/2} \sigma_{xx}\, z\, dz\,; \qquad M_y = \int_{-h/2}^{h/2} \sigma_{yy}\, z\, dz\,; \qquad M_{xy} = \int_{-h/2}^{h/2} \tau_{xy}\, z\, dz \tag{2.19}$$

Substituting the stress relationships given by (2.16) to (2.18) into the (2.19) and evaluating the integrals, we get

$$M_x = -D\left(K_{xx} + \upsilon K_{yy}\right); \quad M_y = -D\left(K_{yy} + \upsilon K_{xx}\right); \quad M_{xy} = -D(1-\upsilon)K_{xy} \tag{2.20}$$

where D is the flexural rigidity that is defined as

$$D = \frac{Eh^3}{12(1-\upsilon^2)} \tag{2.21}$$

and K_{xx}, K_{xy} and K_{yy} are the curvature of the deflected midplane that can be expressed by

$$K_{xx} = \frac{\partial^2 w}{\partial x^2} \tag{2.22}$$

$$K_{xy} = \frac{\partial^2 w}{\partial x \partial y} \tag{2.23}$$

$$K_{yy} = \frac{\partial^2 w}{\partial y^2} \tag{2.24}$$

Substituting (2.4) and (2.6) into (2.2) and replacing the moments using (2.20); produces

$$\frac{\partial^2}{\partial x^2}\{-D(K_{xx} + \upsilon K_{yy})\} + \frac{\partial^2}{\partial y^2}\{-D(K_{yy} + \upsilon K_{xx})\} + 2\frac{\partial^2}{\partial x \partial y}\{-D(1-\upsilon)K_{xy}\} = \rho h \frac{\partial^2 w}{\partial t^2} \tag{2.25}$$

Replacing K_{xx}, K_{yy} and K_{xy} in (2.25) by (2.22) to (2.24) can reduce it to

$$D\left(\frac{\partial^4 w}{\partial x^4} + 2\frac{\partial^4 w}{\partial x^2 \partial y^2} + \frac{\partial^4 w}{\partial y^4}\right) = -\rho h \frac{\partial^2 w}{\partial t^2} = \mathrm{D}\,\nabla^4 w \tag{2.26}$$

where ∇^4 is the biharmonic operator and can be found from Laplacian operator ∇^2. Equation (2.26) describes of the motion for a thin rectangular plate of thickness *h*.

2.2 Plate Dynamics with in-plane forces

In this section, all the assumptions in section 2.1 are valid except assumption 3. The plate is subjected to time dependent in-plane distributed forces that act on the boundary. These forces are $N_x(x,y,t)$, $N_y(x,y,t)$ and $N_{xy}(x,y,t) = N_{yx}(x,y,t)$ - see Fig. 2.4. The equation of motion for a thin rectangular plate with in-plane forces can be derived following [39].

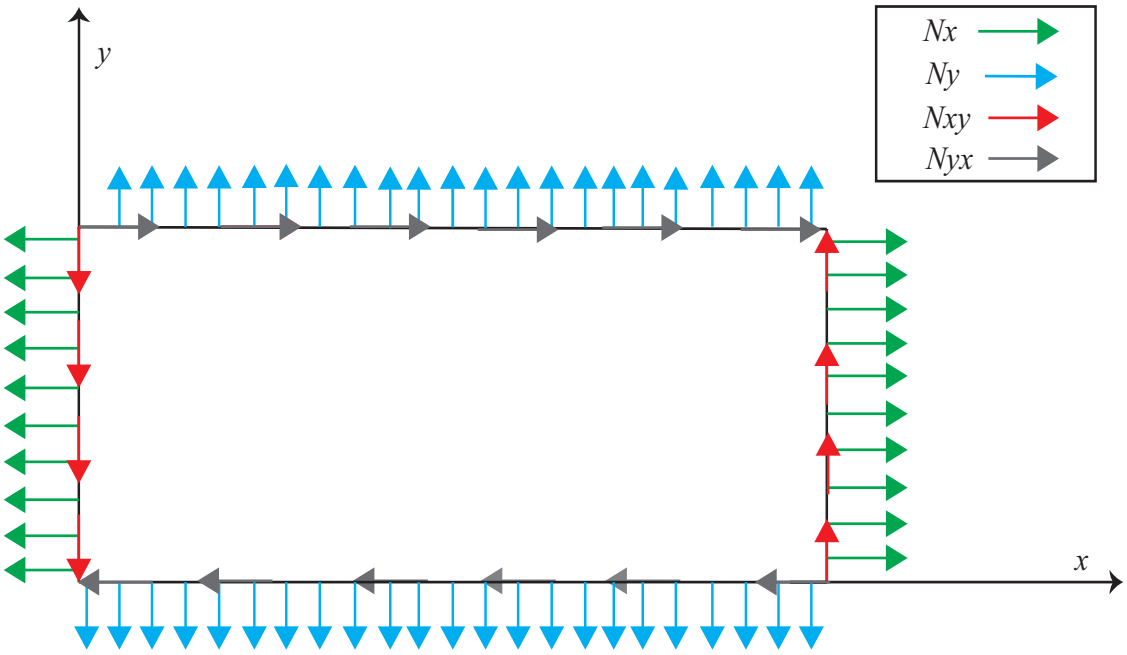

Figure 2.4. Thin rectangular plate with in-plane forces

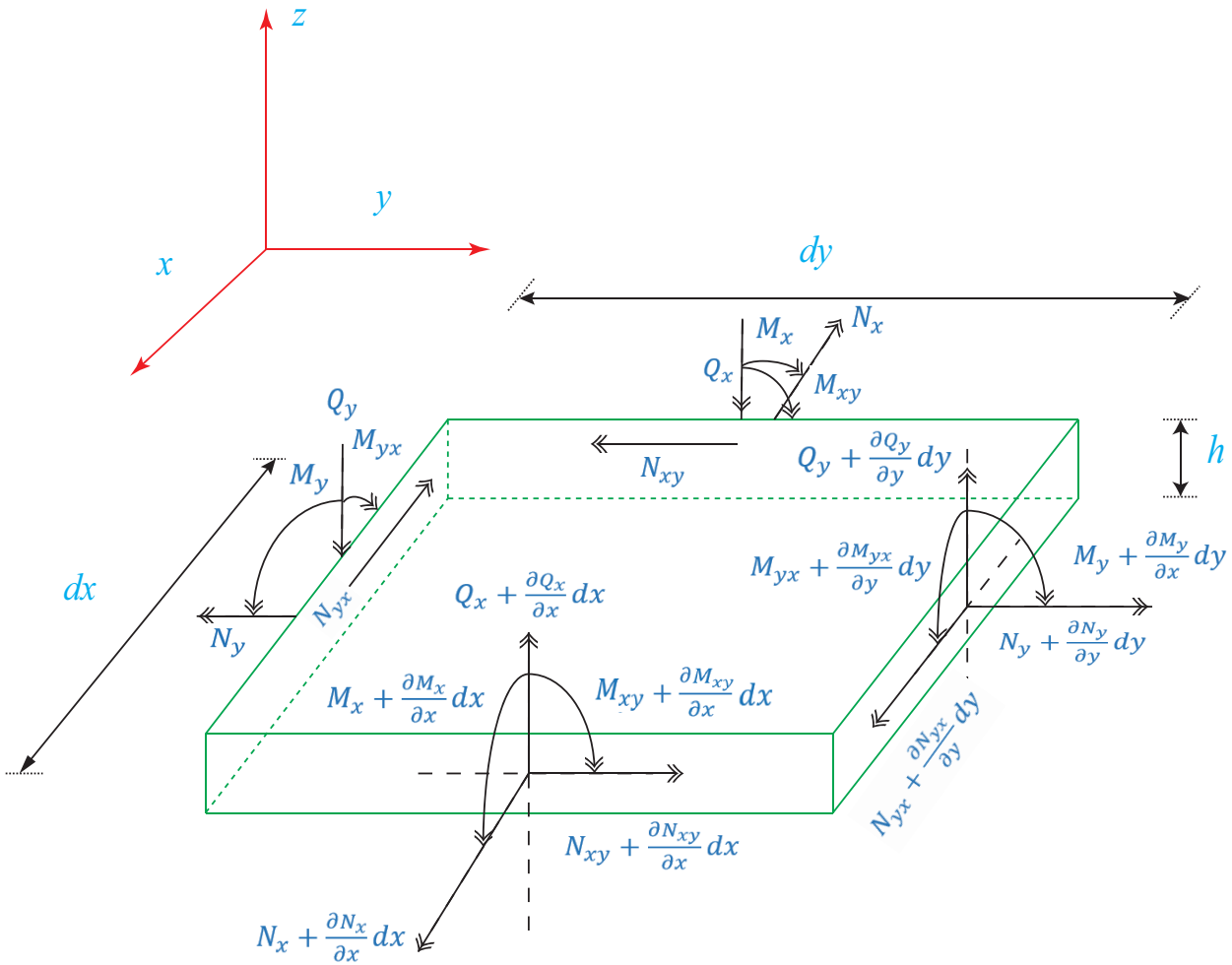

Figure 2.5. An element of the thin rectangular plate with in-plane forces

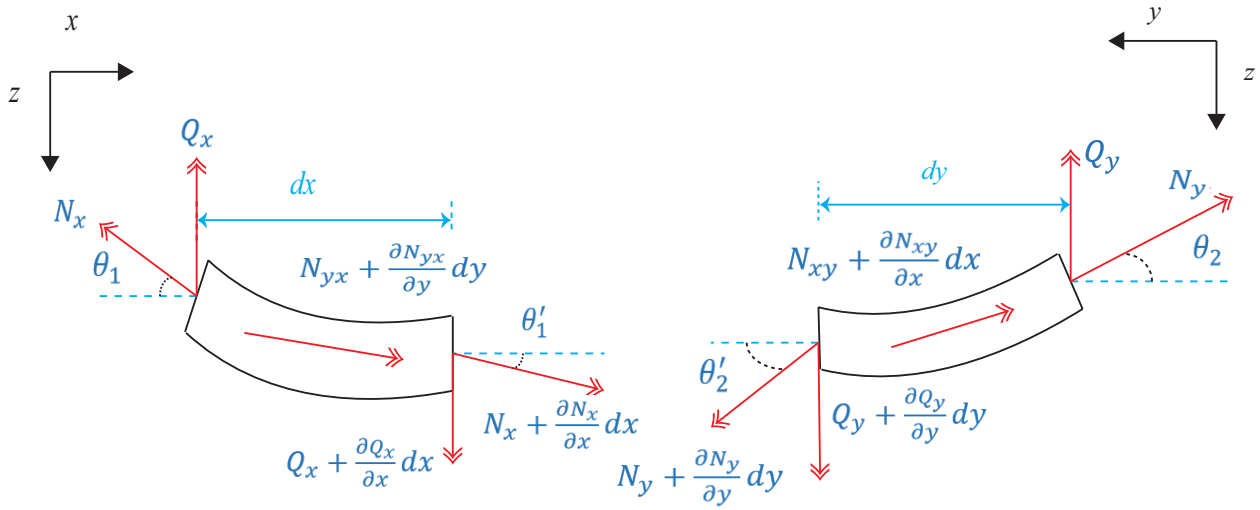

Figure 2.6. Side view for an element of the plate with in-plane forces

For an infinitesimal element as shown in Figs. 2.5 and 2.6, the sum of the forces in the x directions gives

$$(N_x + \frac{\partial N_x}{\partial x}dx)dy\{\cos\theta_1'\} + \left(N_{xy} + \frac{\partial N_{xy}}{\partial y}dy\right)dx\{\cos\frac{\theta_1+\theta_1^{'}}{2}\} - N_x\,dy\{\cos\theta_1\} - N_{xy}\,dy\{\cos\frac{\theta_1+\theta_1^{'}}{2}\} = 0 \tag{2.27}$$

For a small deflection (2.27) can be reduced to

$$\frac{\partial N_x}{\partial x} + \frac{\partial N_{xy}}{\partial y} = 0 \tag{2.28}$$

Similarly, summing the forces in the y direction gives

$$(N_y + \frac{\partial N_y}{\partial y}dy)dx\{\cos\theta_2'\} + \left(N_{xy} + \frac{\partial N_{xy}}{\partial x}dx\right)dy\{\cos\frac{\theta_2+\theta_2^{'}}{2}\} - N_y\,dx\{\cos\theta_2\} - N_{xy}\,dx\{\cos\frac{\theta_2+\theta_2^{'}}{2}\} = 0 \tag{2.29}$$

and for a small deflection the equation can be reduced to

$$\frac{\partial N_y}{\partial y} + \frac{\partial N_{xy}}{\partial x} = 0 \tag{2.30}$$

The sum of the forces in the z direction gives

$$\begin{aligned}(N_x + \frac{\partial N_x}{\partial x}dx)\,dy\{sin\,\theta_1'\} - N_x\,dy\{sin\,\theta_1\} + \left(N_y + \frac{\partial N_y}{\partial y}dy\right)dx\{sin\,\theta_2'\} - \\ N_y\,dx\{sin\,\theta_2\} + \left(N_{yx} + \frac{\partial N_{yx}}{\partial y}dy\right)dx\{sin\,\overline{\theta_1'}\} - N_{yx}\,dx\{sin\,\overline{\theta_1'}\} + \left(N_{xy} + \\ \frac{\partial N_{xy}}{\partial x}dx\right)dy\{sin\,\overline{\theta_2'}\} - N_{xy}\,dy\{sin\,\overline{\theta_2}\} + \left(Q_x + \frac{\partial Q_x}{\partial x}dx\right)dy - Q_x\,dy + \\ \left(Q_y + \frac{\partial Q_y}{\partial y}dy\right)dx - Q_y\,dx = 0\end{aligned} \tag{2.31}$$

For a small deflection and using the following approximations

$$sin\,\theta_1 = \theta_1 = \frac{\partial w}{\partial x};\qquad sin\,\theta_1' = \theta_1' = \theta_1 + \frac{\partial \theta_1}{\partial x}\,dx = \frac{\partial w}{\partial x} + \frac{\partial^2 w}{\partial x^2}\,dx \tag{2.32}$$

$$\sin\theta_2 = \theta_2 = \frac{\partial w}{\partial y}; \quad \sin\theta_2' = \theta_2' = \theta_2 + \frac{\partial \theta_2}{\partial y}\, dy = \frac{\partial w}{\partial y} + \frac{\partial^2 w}{\partial y^2}\, dy \tag{2.33}$$

$$\sin\overline{\theta_1} = \overline{\theta_1} = \frac{\partial w}{\partial x}; \quad \sin\overline{\theta_1'} = \overline{\theta_1'} = \overline{\theta_1} + \frac{\partial \overline{\theta_1}}{\partial x}\, dx = \frac{\partial w}{\partial x} + \frac{\partial^2 w}{\partial x^2}\, dx \tag{2.34}$$

$$\sin\overline{\theta_2} = \overline{\theta_2} = \frac{\partial w}{\partial y}; \quad \sin\overline{\theta_2'} = \overline{\theta_2'} = \overline{\theta_2} + \frac{\partial \overline{\theta_2}}{\partial y}\, dy = \frac{\partial w}{\partial y} + \frac{\partial^2 w}{\partial y^2}\, dy \tag{2.35}$$

Equation (2.31) can be reduced to

$$\frac{\partial Q_x}{\partial x} + \frac{\partial Q_y}{\partial y} = N_x \frac{\partial^2 w}{\partial x^2} + N_y \frac{\partial^2 w}{\partial y^2} + 2N_{xy} \frac{\partial^2 w}{\partial x \partial y} \tag{2.36}$$

Equation (2.36) represents a static equilibrium. By putting the inertia force in (2.36), i.e., d'Alembert's Principle; gives

$$\frac{\partial Q_x}{\partial x} + \frac{\partial Q_y}{\partial y} = -\rho h \frac{\partial^2 w}{\partial t^2} + N_x \frac{\partial^2 w}{\partial x^2} + N_y \frac{\partial^2 w}{\partial y^2} + 2N_{xy} \frac{\partial^2 w}{\partial x \partial y} \tag{2.37}$$

Equation (2.37) represents the dynamic equilibrium in the *z* direction. An important observation should be mentioned that the in-plane forces do not have any contribution to the moment along the edges of the element. Therefore, using the same derivation presented in the section 2.1 for summing the moments about the *x* and *y* axes, the equation of motion for a rectangular plate with in-plane forces can be expressed as

$$D\left(\frac{\partial^4 w}{\partial x^4} + 2\frac{\partial^4 w}{\partial x^2 \partial y^2} + \frac{\partial^4 w}{\partial y^4}\right) = -\rho h \frac{\partial^2 w}{\partial t^2} + N_x \frac{\partial^2 w}{\partial x^2} + N_y \frac{\partial^2 w}{\partial y^2} + 2N_{xy} \frac{\partial^2 w}{\partial x \partial y} \tag{2.38}$$

As mentioned in assumption 5 of section 2.1 for deriving the dynamic equation of a thin rectangular plate, the direct stress in *z* direction σ_{zz} is smaller than other stresses, which is usually neglected. Therefore, the nonzero stress components are only considered for bending

moments for the case of the thin rectangular plate without in-plane forces - see equation (2.19). On the other hand, in the case of a thin rectangular plate with in-plane forces the resulting forces in *x, y*, and in-plane share forces could be evaluated as

$$N_x = \int_{-h/2}^{h/2} \sigma_{xx}\, dz\,; \;\; N_y = \int_{-h/2}^{h/2} \sigma_{yy}\, dz\,; \quad N_{xy} = \int_{-h/2}^{h/2} \tau_{xy}\, dz \tag{2.39}$$

By introducing the Laplacian operator ∇^2, equation (2.38) could be reduced to the compact form

$$\nabla^4 w = \frac{1}{D}\{-\rho h \frac{\partial^2 w}{\partial t^2} + N_x \frac{\partial^2 w}{\partial x^2} + N_y \frac{\partial^2 w}{\partial y^2} + 2N_{xy} \frac{\partial^2 w}{\partial x \partial y}\} \tag{2.40}$$

Chapter 3

Dynamic Behavior of a Thin Rectangular Plate Subjected to In-Plane Forces

In the previous chapter, the equation of motion of a thin rectangular plate, with and without in-plane forces, was presented. In this chapter some analytical and approximate solutions are obtained for the plate subjected to defferent types of in-plane forces. An analytical solution for the plate, with and without in-plane force, is reviewed from the literature for simply supported boundary conditions. An approximate solution is obtained using the Rayleigh-Ritz method, which requires assumed mode shapes that satisfy the geometric boundary conditions. Another approximate solution is obtained using FEM analysis. In this method, a polynomial shape function is used. The methods are compared for a simply supported plate, with and without in-plane forces.

This chapter is divided into two sections based on the nature of the in-plane forces. The first section assumes that the plate is subjected to uniformly distributed in-plane forces that act on the boundary; this results in a uniform stress distribution in the plate. The second section deals with a plate that is subjected to in-plane forces acting at a few discrete locations; this results in a non-uniform stress distribution.

3.1 A Simply-Supported, Thin, Rectangular Plate Subjected To Uniformly Distributed In-Plane Forces

3.1.1 Analytic Solution

Consider the plate shown in Fig. 3.1. The solution to the dynamics of this plate is available in the literature [39]; it is reviewed here for convenience. The transverse vibration of a thin rectangular plate was presented in the last chapter in (2.43). Assuming zero shear forces ($N_{xy} = 0$), the equation can be written as:

$$\nabla^4 w = \left(\frac{\partial^4 w}{\partial x^4} + 2\frac{\partial^4 w}{\partial x^2 \partial y^2} + \frac{\partial^4 w}{\partial y^4}\right) = \frac{1}{D}(\rho h \frac{\partial^2 w}{\partial t^2} + N_x \frac{\partial^2 w}{\partial x^2} + N_y \frac{\partial^2 w}{\partial y^2}) \tag{3.1}$$

where N_x and N_y are the in-plane forces, shown in Fig. 3.1. The solution requires two boundary conditions at each edge. For instance, a simply supported boundary condition on all sides (as in Fig. 3.1) requires the deflection and bending moment to be zero.

$$w(0, y, t) = 0 \tag{3.2}$$

$$w(a, y, t) = 0 \tag{3.3}$$

$$w(x, 0, t) = 0 \tag{3.4}$$

$$w(x, b, t) = 0 \tag{3.5}$$

$$M_x|_{x=0} = -D\left(\frac{\partial^2 w}{\partial x^2} + \nu \frac{\partial^2 w}{\partial y^2}\right)|_{x=0} = 0 \tag{3.6}$$

$$M_x|_{x=a} = -D\left(\frac{\partial^2 w}{\partial x^2} + \nu \frac{\partial^2 w}{\partial y^2}\right)|_{x=a} = 0 \tag{3.7}$$

$$M_y|_{y=0} = -D\left(\frac{\partial^2 w}{\partial y^2} + \nu \frac{\partial^2 w}{\partial x^2}\right)|_{y=0} = 0 \tag{3.8}$$

$$M_y|_{y=b} = -D\left(\frac{\partial^2 w}{\partial y^2} + \nu \frac{\partial^2 w}{\partial x^2}\right)|_{y=b} = 0 \tag{3.9}$$

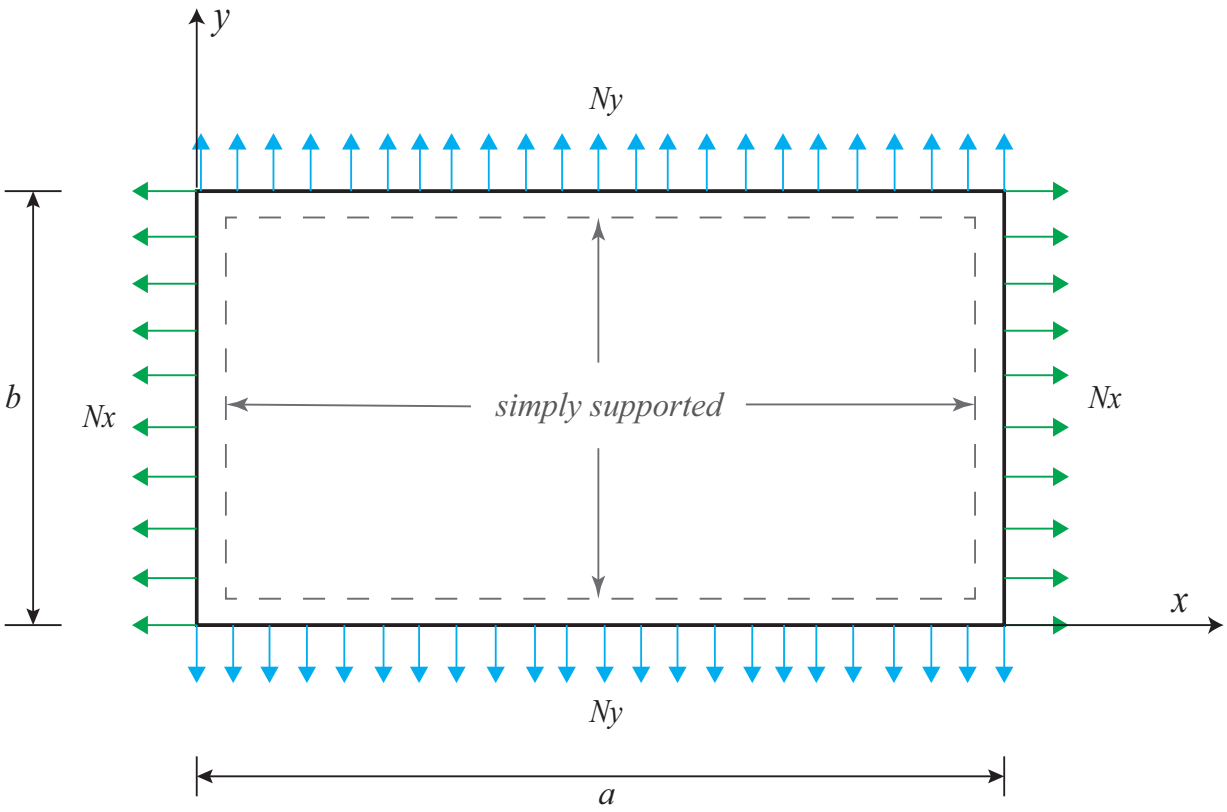

Figure 3.1. Simply supported plate with uniformly distributed in-plane forces

The solution to the governing equation in (3.1) is assumed to be of the form:

$$w(x,y,t) = W(x,y)\, e^{j\omega t} \tag{3.10}$$

Substituting (3.10) into (3.1) gives

$$\nabla^4 W\, e^{j\omega t} = \frac{-1}{D}\rho h\, W\omega^2\, e^{j\omega t} + \frac{N_x}{D}\frac{\partial^2 W}{\partial x^2}\, e^{j\omega t} + \frac{N_y}{D}\frac{\partial^2 W}{\partial y^2}\, e^{j\omega t} \tag{3.11}$$

Dividing both sides by $(e^{j\omega t})$ and assuming the $\lambda^4 = \frac{-\rho h\, \omega^2}{D}$ yields

$$\nabla^4 W - \lambda^4 W = \frac{N_x}{D}\frac{\partial^2 W}{\partial x^2} + \frac{N_y}{D}\frac{\partial^2 W}{\partial y^2} \tag{3.12}$$

In general, the solution for a simply supported plate that is not subjected to in-plane forces can be expressed as [39]

$$W(x,y) = \sum_{m,n=1}^{\infty} A_{mn} \sin\left(\frac{m\pi\, x}{a}\right) \sin\left(\frac{n\pi\, y}{b}\right) \tag{3.13}$$

where A_{mn} is a constant represents the amplitude. Because the in-plane forces will not affect the bending moment at the edges, we can substitute (3.13) into (3.12) to get (3.14)

$$\omega_{mn}^2 = \frac{D}{\rho h}\left\{\left(\frac{m\,\pi}{a}\right)^2 + \left(\frac{n\,\pi}{b}\right)^2\right\}^2 + \frac{1}{\rho h}\left\{N_x\left(\frac{m\pi}{a}\right)^2 + N_y\left(\frac{n\pi}{b}\right)^2\right\}; \quad \text{where } (m,n = 1,2,..\infty) \tag{3.14}$$

Equation (3.16) can be used to compute the frequencies of a thin rectangular plate with in-plane forces. When N_x and N_y are zero, (3.14) reduces to the form

$$\omega_{mn}^2 = \frac{D}{\rho h}\left\{\left(\frac{m\,\pi}{a}\right)^2 + \left(\frac{n\,\pi}{b}\right)^2\right\}^2 \tag{3.15}$$

3.1.2 Rayleigh-Ritz Approximation

In the Rayleigh-Ritz method, we assumed the solution of the equation of motion in the following form

$$w(x,y,t) = W(x,y)\, \cos\omega t \tag{3.16}$$

The maximum kinetic and potential energies for the plate shown in Fig. 3.1 can be evaluated from

$$T_{max} = \frac{1}{2}\omega^2 \iint \rho h\, W^2 dx\, dy \tag{3.17}$$

$$U_{max} = \frac{1}{2}\iint \left\{D\left[(\nabla^2 W) + 2(1-\upsilon)\left[{W_{xy}}^2 - W_{xx}W_{yy}\right]\right] + N_x(W_x)^2 + N_y(W_y)^2\right\} dx\, dy \tag{3.18}$$

The Rayleigh quotient, is defined as

$$R = \omega^2 = \frac{U_{max}}{T_{max}}$$

$$= \frac{\frac{1}{2}\iint \left\{D\left[(\nabla^2 W) + 2(1-\upsilon)\left[{W_{xy}}^2 - W_{xx}W_{yy}\right]\right] + N_x(W_x)^2 + N_y\left(W_y\right)^2\right\} dx\, dy}{\frac{1}{2}\iint \rho h\, W^2 dx\, dy} \tag{3.19}$$

where $D = (Eh^3)/12(1-\upsilon^2)$, $W_{xx} = \partial^2 W/\partial x^2$, $W_{yy} = \partial^2 W/\partial y^2$and $W_{xy} = \partial^2 W/\partial x \partial y$.

The *n*-terms approximation for $W(x,y)$ in (3.16) can be expressed as

$$\begin{aligned} W(x,y) &= \sum_{j=1}^{n} C_j \phi_j(x,y) \\ &= C_1\phi_1(x,y) + C_2\phi_2(x,y) + \cdots + C_n\phi_n(x,y) \end{aligned} \tag{3.20}$$

where $\phi_j(x,y)$ is a mode shape that satisfies the geometric boundary conditions, and C_j are the constants that will be determined. Letting

$$P = \frac{12\rho\,(1-\upsilon^2)}{E} \tag{3.21}$$

Equation (3.19) can be reduced to

$$\rho\omega^2 =$$

$$\frac{\frac{1}{2}\iint\left\{h^3\left[{W_{xx}}^2+{W_{yy}}^2+2\nu W_{xx}W_{yy}+2(1-\upsilon)\left[{W_{xy}}^2\right]\right]+\frac{N_x}{P}(W_x)^2+\frac{N_y}{P}(W_y)^2\right\}dx\, dy}{\frac{1}{2}\iint h\, W^2 dx\, dy} \tag{3.22}$$

Substituting (3.20) into (3.22), we get

$$\rho\omega^2 = \frac{1}{B}\left[\frac{1}{2}\iint h^3\left\{\left(\sum_{j=1}^{n} C_j\phi_j^{xx}\right)^2 + \left(\sum_{j=1}^{n} C_j\phi_j^{yy}\right)^2 + 2\nu\left(\sum_{j=1}^{n} C_j\phi_j^{xx}\right)\left(\sum_{j=1}^{n} C_j\phi_j^{yy}\right) + 2(1-\upsilon)\left(\sum_{j=1}^{n} C_j\phi_j^{xy}\right)^2 + \frac{N_x}{P}\left(\sum_{j=1}^{n} C_j\phi_j^{x}\right)^2 + \frac{N_y}{P}\left(\sum_{j=1}^{n} C_j\phi_j^{y}\right)^2\right\} dx\, dy\right] \tag{3.23}$$

where

$$B = \frac{1}{2}\iint h\left(\sum_{j=1}^{n} C_j\phi_j\right)^2 dx\, dy \tag{3.24}$$

and $\phi_j^{xx} = \partial^2\phi_j/\partial x^2$, $\phi_j^{yy} = \partial^2\phi_j/\partial y^2$ and $\phi_j^{xy} = \partial^2\phi_j/\partial x\partial y$. By minimizing (3.23) with respect to C_j as

$$\frac{\partial\rho\omega^2}{\partial C_j} = 0 \qquad i = 1,2,\ldots,n \tag{3.25}$$

we obtain

$$
\begin{aligned}
\iint h\Big(\sum_{j=1}^{n} C_j\phi_j\Big)^2\,dx\,dy \Bigg[\iint \{\, h^3 \Bigg(& \phi_j^{xx} \sum_{j=1}^{n} C_j\phi_j^{xx} \\
& + \phi_j^{yy} \sum_{j=1}^{n} C_j\phi_j^{yy} + v\phi_j^{xx} \sum_{j=1}^{n} C_j\phi_j^{yy} + v\phi_j^{yy} \sum_{j=1}^{n} C_j\phi_j^{xx} \\
& + 2(1-v)\phi_j^{xy} \sum_{j=1}^{n} C_j\phi_j^{xy} \Bigg) \\
& + \frac{N_x}{P}\phi_i^{x} \sum_{j=1}^{n} C_j\phi_j^{x} + \frac{N_y}{P}\phi_i^{y} \sum_{j=1}^{n} C_j\phi_j^{y} \Bigg] dx\,dy \\
& - \iint \phi_i \Big(\sum_{j=1}^{n} C_j\phi_j dx dy\Big) \Bigg[\iint \Bigg\{ h^3 \Bigg(\Big(\sum_{j=1}^{n} C_j\phi_j^{xx}\Big)^2 \\
& + \Big(\sum_{j=1}^{n} C_j\phi_j^{yy}\Big)^2 + 2v \Big(\sum_{j=1}^{n} C_j\phi_j^{xx}\Big)\Big(\sum_{j=1}^{n} C_j\phi_j^{yy}\Big) \\
& + 2(1-v)\Big(\sum_{j=1}^{n} C_j\phi_j^{xy}\Big)^2 \Bigg) + \frac{N_x}{P}\Big(\sum_{j=1}^{n} C_j\phi_j^{x}\Big)^2 \\
& + \frac{N_y}{P}\Big(\sum_{j=1}^{n} C_j\phi_j^{y}\Big)^2 \Bigg\} dx\,dy \Bigg] \\
& = 0
\end{aligned}
\tag{3.26}
$$

Substituting (3.23) back into the (3.26), we get

$$\iint h(\sum_{j=1}^{n} C_j\phi_j)^2\,dx\,dy\left[\iint\{h^3\left(\phi_j^{xx}\sum_{j=1}^{n} C_j\phi_j^{xx}\right.\right.$$
$$+\phi_j^{yy}\sum_{j=1}^{n} C_j\phi_j^{yy}+\upsilon\,\phi_j^{xx}\sum_{j=1}^{n} C_j\phi_j^{yy}+\upsilon\,\phi_j^{yy}\sum_{j=1}^{n} C_j\phi_j^{xx}$$
$$\left.+2(1-\upsilon)\phi_j^{xy}\sum_{j=1}^{n} C_j\phi_j^{xy}\right)$$
$$+\frac{N_x}{P}\phi_i^{x}\sum_{j=1}^{n} C_j\phi_j^{x}+\frac{N_y}{P}\phi_i^{y}\sum_{j=1}^{n} C_j\phi_j^{y}\Bigg]dx\,dy \qquad (3.27)$$
$$-\iint\phi_i\left(\sum_{j=1}^{n} C_j\phi_j dxdy\right)\left[\rho\omega^2 h\left(\sum_{j=1}^{n} C_j\phi_j\right)^2 dx\,dy\right]$$
$$=0$$

Dividing both sides by $\left\{\iint\left(\sum_{j=1}^{n} C_j\phi_j\right)^2 dx\,dy\right\}$, we get

$$\sum_{j=1}^{n} c_j\iint\left\{h^3\left(\phi_i^{xx}\phi_j^{xx}+\phi_i^{yy}\phi_j^{yy}+\upsilon\,\phi_i^{xx}\phi_j^{yy}+\upsilon\,\phi_i^{yy}\phi_j^{xx}\right.\right.$$
$$\left.+2(1-\upsilon)\phi_i^{xy}\phi_j^{xy}\right)+\frac{N_x}{P}\phi_i^{x}\phi_j^{x}+\frac{N_y}{P}\phi_i^{y}\phi_j^{y}\Bigg\}dx\,dy \qquad (3.28)$$
$$-\rho\omega^2\sum_{j=1}^{n} C_j\iint\phi_i\phi_j\,h\,dx\,dy=0$$

Denoting the first term in (3.31) as a_{ij} and the second term as b_{ij}, and $\zeta^2=\rho\omega^2$ we get

$$\sum_{j=1}^{n}(a_{ij}-\zeta^2 b_{ij})C_j=0 \qquad (3.29)$$

The eigenvalue problem (3.29) is used to solve the dynamic equation. To illustrate this method, an example is provided below:

The Rayleigh quotient can be expressed as

$$R = \omega^2 = \frac{U_{max}}{T_{max}} = \frac{N}{D} \tag{3.30}$$

where N and D can be expressed as follows:

$$N = U_{max} = \frac{1}{2}\sum_{i=1}^{n}\sum_{j=1}^{n} c_i c_j [\boldsymbol{k}_{ij}] = \frac{1}{2}\vec{C}^T \boldsymbol{K}\vec{C} \tag{3.31}$$

$$D = T_{max} = \frac{1}{2}\sum_{i=1}^{n}\sum_{j=1}^{n} c_i c_j [\boldsymbol{m}_{ij}] = \frac{1}{2}\vec{C}^T \boldsymbol{M}\vec{C} \tag{3.32}$$

where $\boldsymbol{K} = [k_{ij}]$ is the stiffness matrix, $\boldsymbol{M} = [m_{ij}]$ is the mass matrix and $\vec{C} = \begin{Bmatrix} c_1 \\ c_2 \\ \cdot \\ \cdot \\ c_n \end{Bmatrix}$. The elements of the stiffness and mass matrices are defined below:

$$\boldsymbol{K} = \iint \left[D\left(\varphi_{xx}^2 + \varphi_{yy}^2 + 2\upsilon\varphi_{xx}\varphi_{yy} + 2(1-\upsilon)\varphi_{xy}^2\right) + N_x\varphi_x^2 + N_y\varphi_y^2\right] dx\, dy \tag{3.33}$$

$$\boldsymbol{M} = \iint \rho h\, \varphi^2 dx\, dy \tag{3.34}$$

where $\varphi_{xx} = \partial^2\phi/\partial x^2$, $\varphi_{yy} = \partial^2\phi/\partial y^2$ and ϕ is the assumed mode shapes. We can express (3.30) as

$$R(c_1, c_2, \dots, c_n) = \frac{N(c_1, c_2, \dots, c_n)}{D(c_1, c_2, \dots, c_n)} \tag{3.35}$$

Minimizing (3.35) with respect to $c_{i's}$ $i = 1,2 \dots n$, we get

$$\frac{\partial R}{\partial c_i} = \frac{D\dfrac{\partial N}{\partial c_i} - N\dfrac{\partial D}{\partial c_i}}{D^2} = 0 \qquad i = 1,2, \dots, n \tag{3.36}$$

$$\frac{1}{D}\left(\frac{\partial N}{\partial c_i}-\frac{N}{D}\frac{\partial D}{\partial c_i}\right)=0$$

$$\left(\frac{\partial N}{\partial c_i}-\lambda^{(i)}\frac{\partial D}{\partial c_i}\right)=0 \qquad \lambda^{(i)} \triangleq \frac{N}{D}$$

where $\lambda^{(i)}$ are the eigenvalues. Form (3.31) and (3.32) we have $\frac{\partial N}{\partial \vec{c}_i} = \vec{C}\,\boldsymbol{K}$ and $\frac{\partial D}{\partial \vec{c}_i} = \vec{C}\,\boldsymbol{M}$,

(3.36) can be reduced to

$$\left(\boldsymbol{K}-\lambda^{(i)}\boldsymbol{M}\right)\vec{C}=0 \qquad i=1,2,\ldots.,n \tag{3.37}$$

The free vibration equation can be expressed as

$$-\omega^2\boldsymbol{M}\,W\,cos\omega t+\boldsymbol{K}\,W\,cos\omega t=0 \tag{3.38}$$

Dividing both sides by $(cos\omega t)$ gives

$$(\boldsymbol{K}-\omega^2\boldsymbol{M})W=0 \tag{3.39}$$

where the mass matrix, $\boldsymbol{M}$, can be evaluated from

$$\boldsymbol{M}=\int_0^a\int_0^b h\;\phi_i\phi_j\,dx\,dy \tag{3.40}$$

and the stiffness matrix, $\boldsymbol{K}$, can be obtained from

$$\boldsymbol{K}=\boldsymbol{K_b}+\boldsymbol{K_{fx}N_x}+\boldsymbol{K_{fy}N_y} \tag{3.41}$$

where

$$\boldsymbol{K_b}=\int_0^a\int_0^b\left\{D\left(\phi_{xx}^2+\phi_{yy}^2+2\upsilon\,\phi_{xx}\phi_{yy}+2(1-\upsilon)\phi_{xy}^2\right)\right\}dx\,dy \tag{3.42}$$

$$\boldsymbol{K_{fx}}=\int_0^a\int_0^b\phi_x^2\,dx\,dy$$

$$\boldsymbol{K_{fy}}=\int_0^a\int_0^b\phi_y^2\,dx\,dy \tag{3.43}$$

For the plate without in-plane forces, equations (3.43) are neglected. From (3.39) – (3.43) we can obtain the dynamics of the plate with and without the uniformly distributed in-plane forces using Rayleigh-Ritz method.

3.1.3 Finite Element Analysis

The finite element method use variation and interpolation methods to obtain the dynamics of a structure efficiently. Usually, the FEM method is used for complex structures with complex boundary conditions. In this method, the actual structure is divided into small finite parts that are called finite elements. These elements have nodes that surround and connect them to the neighboring elements. This combination is called the finite element mesh. The solution of the governing equation is found for each element individually using polynomial shape function that satisfies the geometrical boundary conditions of the structure. This solution is called a local solution. Then, the local solutions for all elements are assembled to find the global solution. In this section, the FEM analysis uses the kinetic energy and the potential energy to obtain the dynamics of the plate using the global solution after we applied the boundary conditions. The plate is discretized into finite quad elements as shown in Fig. 3.2 has four nodes and each node has three degree of freedoms, namely, one translational degree of freedom in the z direction, W_{ij}, and two rotational degrees of freedom, W_{xij} and W_{yij}, about the x and y axes respectively.

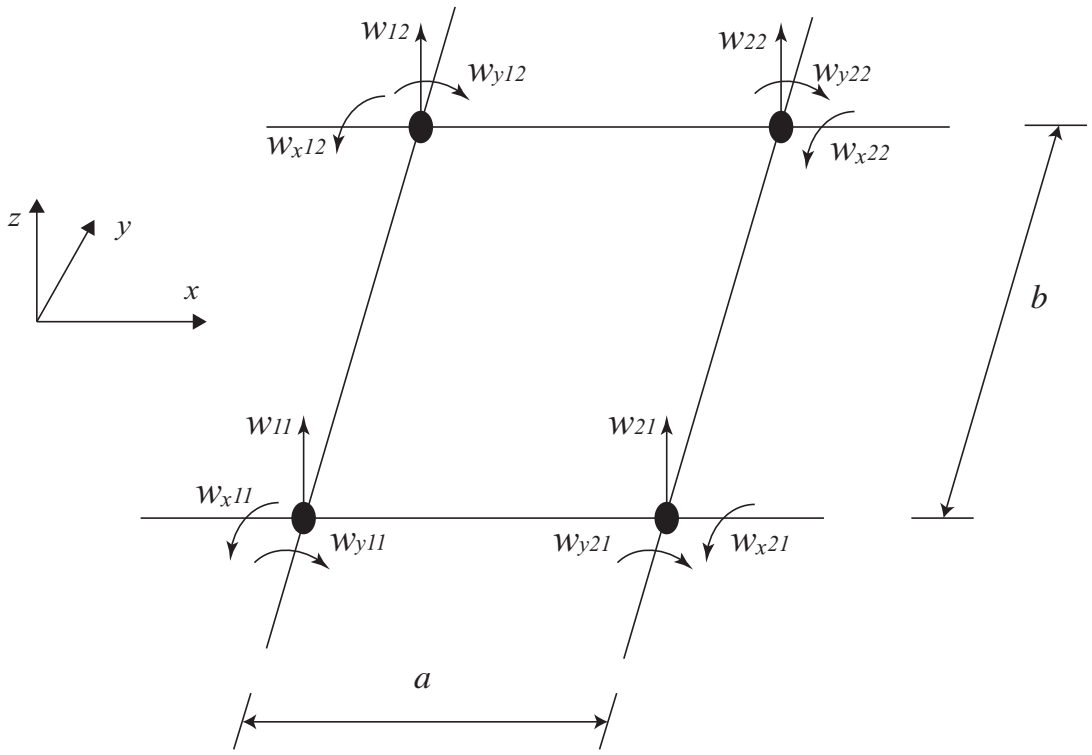

Figure 3.2. Four-node quad plate element with 12 DOF's

For the element shown in Fig. 3.2, the polynomial shape function can be assumed in the following form [49]:

$$W(x,y) = \sum_{i=1}^{2}\sum_{j=1}^{2}[H_{0i}^{(0)}(x)\,H_{0j}^{(0)}(y)\,w_{ij} + H_{1i}^{(1)}(x)\,H_{0j}^{(1)}(y)\,w_{xij} + H_{0i}^{(1)}(x)\,H_{1j}^{(1)}(y)\,w_{yij}] \tag{3.44}$$

where the functions in the x and y directions are

$$H_{01}^{(0)}(x) = \frac{-1}{a}(x-a) \tag{3.45}$$

$$H_{01}^{(0)}(y) = \frac{-1}{b}(y-b) \tag{3.46}$$

$$H_{02}^{(0)}(x) = \frac{x}{a} \tag{3.47}$$

$$H_{02}^{(0)}(y) = \frac{y}{b} \tag{3.48}$$

$$H_{01}^{(1)}(x) = \frac{1}{a^3}(2\,x^3 - 3\,a\,x^2 + a^3) \tag{3.49}$$

$$H_{01}^{(1)}(y) = \frac{1}{b^3}(2\,y^3 - 3\,b\,y^2 + b^3) \tag{3.50}$$

$$H_{02}^{(1)}(x) = \frac{-1}{a^3}(2\,x^3 - 3\,a\,x^2) \tag{3.51}$$

$$H_{02}^{(1)}(y) = \frac{-1}{b^3}(2\,y^3 - 3\,b\,y^2) \tag{3.52}$$

$$H_{11}^{(1)}(x) = \frac{1}{a^2}(x^3 - 2\,a\,x^2 + a^2\,x) \tag{3.53}$$

$$H_{11}^{(1)}(y) = \frac{1}{b^2}(y^3 - 2\,b\,y^2 + b^2\,y) \tag{3.54}$$

$$H_{12}^{(1)}(x) = \frac{1}{a^2}(x^3 - a\,x^2) \tag{3.55}$$

$$H_{12}^{(1)}(y) = \frac{1}{b^2}(y^3 - b\,y^2) \tag{3.56}$$

The polynomial shape function (3.44) is used to obtain the stiffness and mass matrices for each element using the potential and kinetic energies as presented in section 3.1.2. Equation (3.33) and (3.34) can be used to express the elemental stiffness and mass matrices as follows:

$$\boldsymbol{K}_e = \frac{1}{D}\iint \left[W_{xx}^2 + W_{yy}^2 + 2\upsilon W_{xx}W_{yy} + 2(1-\upsilon)W_{xy}^2\right]dx\,dy + \iint [N_x W_x^2 + N_y W_y^2]dx\,dy \tag{3.57}$$

$$\boldsymbol{M}_e = \iint \rho h\, W^2 dx\,dy \tag{3.58}$$

After we obtained the stiffness and mass matrices for each element, we assembled them to get the global stiffness and mass matrices. Then, the boundary conditions are applied to

obtain the reduced global matrices. These reduced matrices are used to obtain the frequencies and mode shapes of the plate.

$$\left(\boldsymbol{K}_G - \lambda^{(n)}\boldsymbol{M}_G\right)\varphi = 0 \tag{3.59}$$

where $\lambda^{(n)}$ is the eigenvalues and φ are the eigenvectors. $\boldsymbol{K}_G$ and $\boldsymbol{M}_G$ are the reduced global stiffness and mass matrices.

3.1.4 Comparisons

In order to examine the accuracy of the approximation methods, a comparison with the analytical solution is made for a simply supported plate, with and without in-plane forces. A plate with the dimensions shown in Fig. 3.3 is considered.

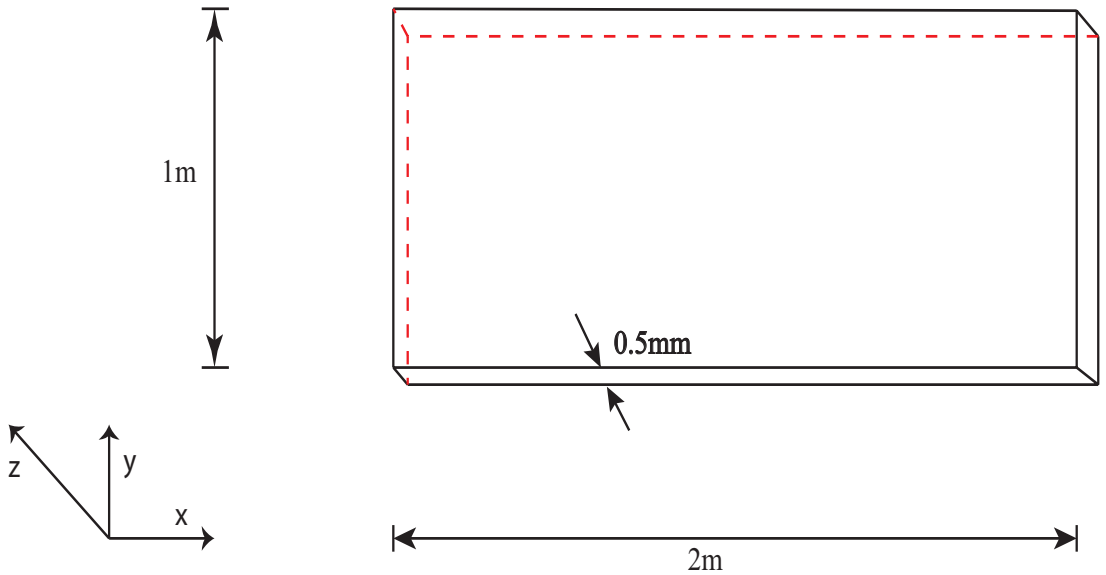

Figure 3.3. Thin rectangular plate dimensions

The material properties for the plate are assumed to be:

Material	Aluminum
Young's modulus	70 Gpa
Mass density	2730 kg/m^3

Table 3.1 shows the first five natural frequencies for the plate without in-plane forces and both approximation methods that presented in sections 3.1.2 and 3.1.3. In the finite element method, we used 20×10 elements meshing as shown in the Fig. 3.4.

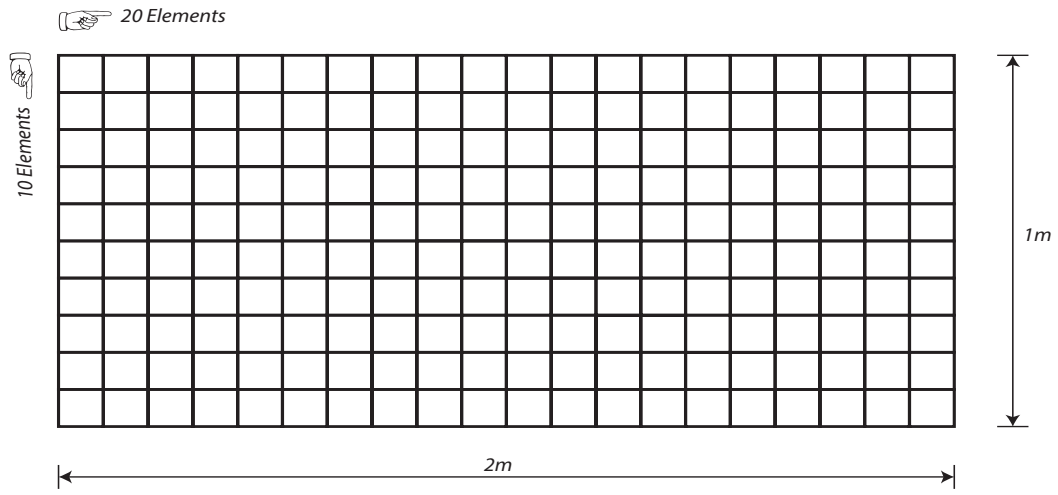

Figure 3.4. Finite element meshing for the plate

Table 3.1. Comparing the Solutions for Thin Rectangular Plate without In-Plane Forces

Mode	Analytical in Hz	FEM in Hz	Rayleigh-Ritz in Hz	% Error in FEM	% Error in Rayleigh-Ritz
1	1.532	1.5531	1.53088	2.22	0.073
2	2.4512	2.5045	2.44912	3.52	0.084
3	3.9832	4.0590	3.98001	3.19	0.08
4	6.1279	6.2190	6.12353	2.27	0.071
5	6.1279	6.2193	6.12353	2.60	0.071

Table 3.1 shows that the Rayleigh-Ritz approximation is closer to the analytical solution than the EFM method because it uses mode shapes instead of polynomial shape functions. However, the FEM solution could be improved by increasing the number of elements, i.e., by using finer meshing. The results show that the maximum error using FEM method is around 3.5%, however, the maximum error for the Rayleigh-Ritz method is 0.084%. In conclusion, using these approximations, we obtained solutions close to the analytical solution with acceptable level of accuracy.

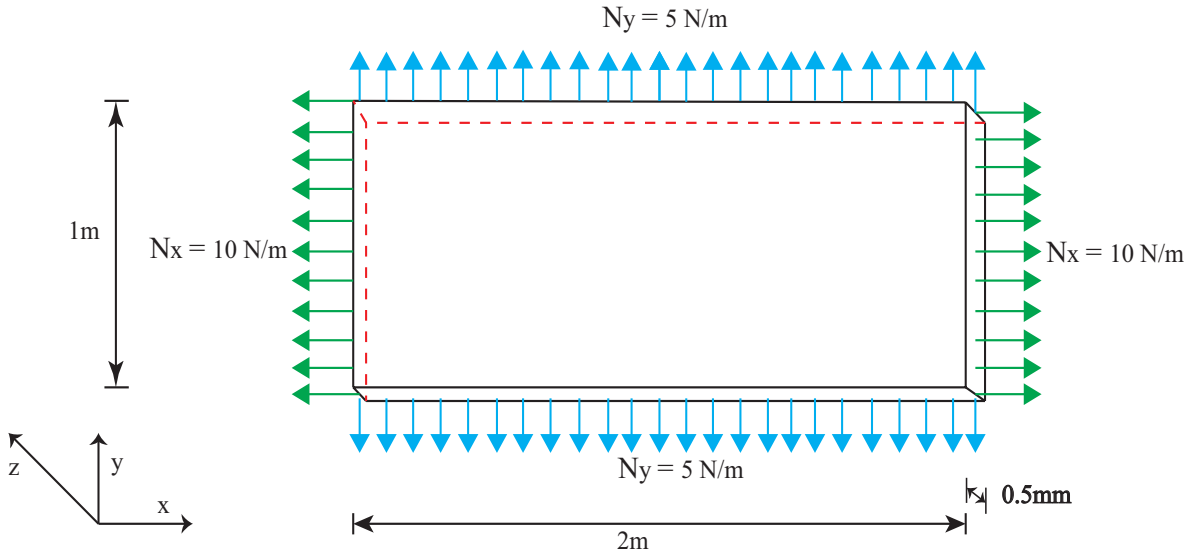

Figure 3.5. Thin rectangular plate with uniformly distributed in-plane forces

For a plate with similar material and geometrical properties, we added uniformly distributed in-plane forces along the boundaries as shown in Fig. 3.5. The forces along the x axis is denoted as $N_x = 10N/m$ and the forces along the y axis is $N_y = 5N/m$. The results are shown in Table 3.2 using the analytical and both approximation methods.

Table 3.2. Comparing the Solutions for Thin Rectangular Plate with In-Plane Distributed Forces

Mode	Analytical in Hz	FEM in Hz	Rayleigh -Ritz in Hz	% Error in FEM	% Error in Rayleigh -Ritz
1	1.9289	1.9456	1.92765	1.415	0.064
2	2.959	3.0032	2.9568	2.45	0.074
3	4.5719	4.6380	4.56859	2.44	0.072
4	6.5609	6.6461	6.55641	1.99	0.068
5	6.7671	6.8495	6.76247	2.15	0.068

As shown, the Rayleigh-Ritz method is more accurate compared with FEM. However, using the Rayleigh-Ritz method has the limitation that it depends on mode shapes that should satisfy the geometrical boundary conditions. In contrary, FEM method can solve more complex geometry and boundary conditions. Therefore, the FEM can handle problems where the in-plane forces are not uniformly distributed; in other words it can solve the problem where these in-plane forces are prescribed at arbitrary locations on the plate. With the maximum error reach around 2.4% using FEM, the results lie in the acceptable range of accuracy and can be considered as close to the analytical solution. Figure 3.6 shows the mode shapes associated with the frequencies listed in Table 3.2.

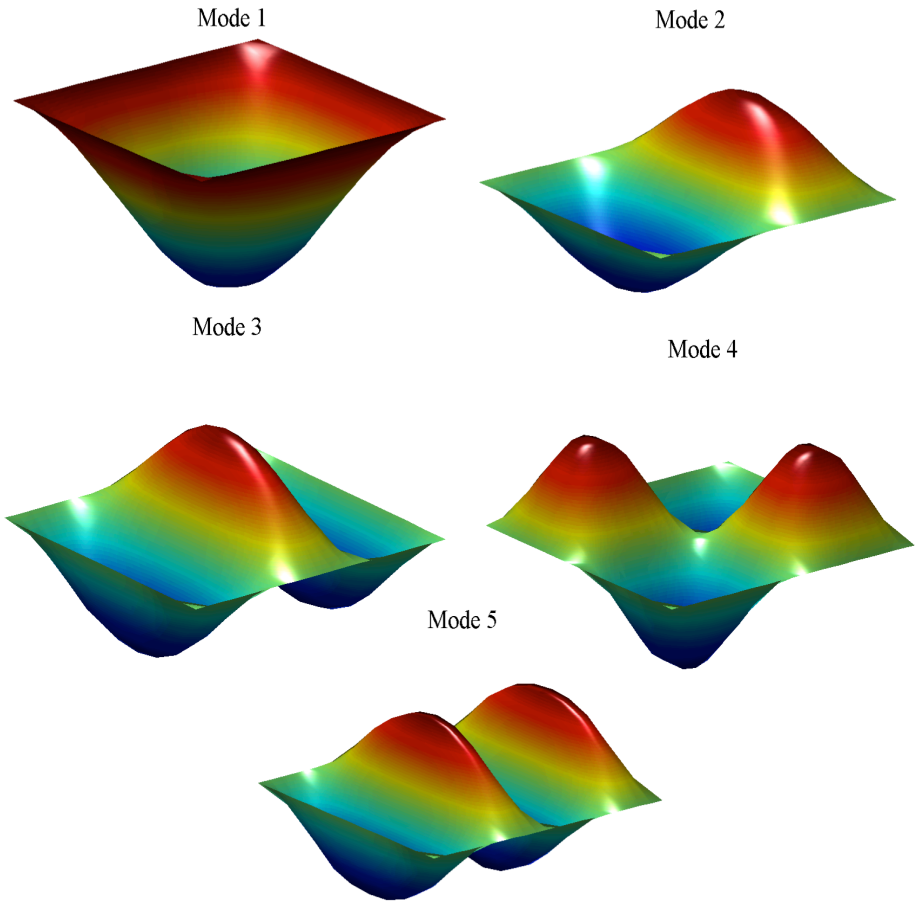

Figure 3.6. First five mode shapes for thin simply supported rectangular plate with uniformly distributed in-plane forces

3.2 A Simply-Supported Thin Rectangular Plate Subjected To In-Plane Forces At A Few Discrete Locations

In section 3.1, we presented three different ways to solve the governing equation, namely, the analytical method, the Rayleigh-Ritz method, and the finite elements method. For the case where there are in-plane forces at a few discrete locations, the analytical solution is not available in the literature and the Rayleigh-Ritz method become cumbersome because the mode shapes for such problems with non-uniform stress distributions are not readily

available. Therefore, the FEM is used to numerically solve the governing equation. We use a code we created using MATLAB and verify the results using commercial FEM software.

3.2.1 Finite Element Analysis

The analysis is divided into two steps: evaluating in-plane stress distributions and out-of-plane vibration analysis. The quad element shown in the Fig. 3.7 is used for in-plane stress distributions. The element has four nodes: one at each corner, and two degrees of freedom at each node. These degrees of freedom are the components of in-plane displacement, *u* and *v,* in the *x* and *y* directions respectively.

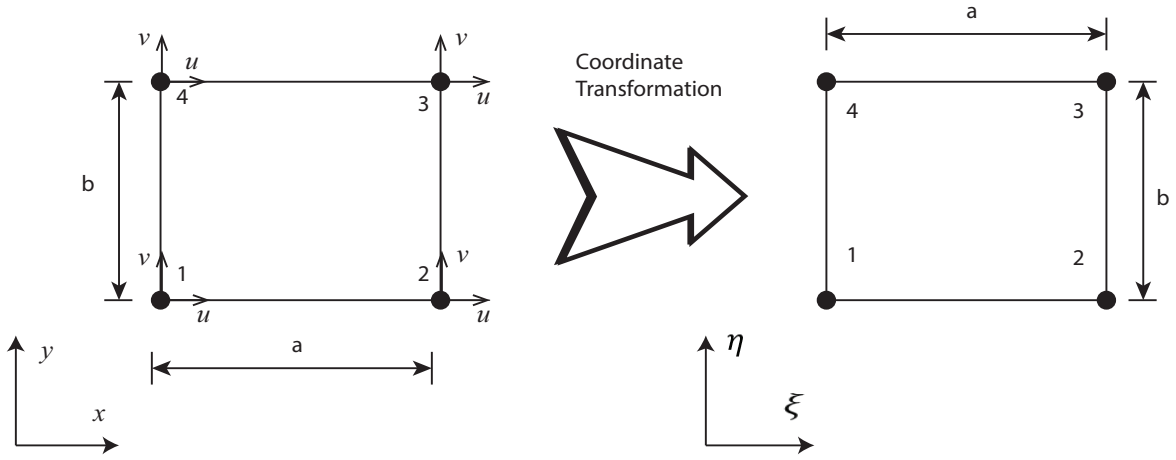

Figure 3.7. Dimensions of the plate's element and coordinate transformation

Each component of in-plane displacement can be defined in non-dimensional coordinates as

$$u = \sum_{j=1}^{4} N_j u_j \; ; \qquad v = \sum_{j=1}^{4} N_j v_j \tag{3.60}$$

where the shape function N_j can be written using the coordinate transformation shown in Fig. 3.7 as follows:

$$N_1 = \frac{1}{4}(1-\xi)(1-\eta) \tag{3.61}$$

$$N_2 = \frac{1}{4}(1+\xi)(1-\eta) \tag{3.62}$$

$$N_3 = \frac{1}{4}(1+\xi)(1+\eta) \tag{3.63}$$

$$N_4 = \frac{1}{4}(1-\xi)(1+\eta) \tag{3.64}$$

The displacement vector for each element can be written as

$$\{U\}_e^T = [u_1 \quad v_1 \quad u_2 \quad v_2 \quad u_3 \quad v_3 \quad u_4 \quad v_4] \tag{3.65}$$

and

$$[N] = \begin{bmatrix} N_1 & 0 & N_2 & 0 & N_3 & 0 & N_4 & 0 \\ 0 & N_1 & 0 & N_2 & 0 & N_3 & 0 & N_4 \end{bmatrix} \tag{3.66}$$

Combining (3.65) and (3.66), the in-plane displacements for each element can be expressed as

$$\begin{bmatrix} u \\ v \end{bmatrix} = \begin{bmatrix} N_1 & 0 & N_2 & 0 & N_3 & 0 & N_4 & 0 \\ 0 & N_1 & 0 & N_2 & 0 & N_3 & 0 & N_4 \end{bmatrix} \begin{bmatrix} u_1 \\ v_1 \\ u_2 \\ v_2 \\ u_3 \\ v_3 \\ u_4 \\ v_4 \end{bmatrix} = [N]\{U\}_e \tag{3.67}$$

The kinetic energy for a plate element can be obtained from

$$T_e = \frac{1}{2}\int \rho h \left\{\dot{U}\right\}_e dA = \frac{1}{2}\left\{\dot{U}\right\}_e^T \boldsymbol{M}_e \left\{\dot{U}\right\}_e \tag{3.68}$$

where $\boldsymbol{M}_e$ is the elemental mass matrix and can be evaluated from

$$\boldsymbol{M}_e = \int \rho\, [N]^T [N]\, dA \tag{3.69}$$

The potential energy for each element is given by the expression

$$U_e = \frac{1}{2}\int h\, \{\varepsilon\}_e{}^T [D_{mat}]\, \{\varepsilon\}_e\, dA \tag{3.70}$$

where

$$\{\varepsilon\}_e = \begin{bmatrix} \dfrac{\partial u}{\partial x} \\ \dfrac{\partial v}{\partial y} \\ \dfrac{\partial u}{\partial y} + \dfrac{\partial v}{\partial x} \end{bmatrix} \tag{3.71}$$

and $[D_{mat}]$ is the constituent matrix for in-plane stress analysis. $[D_{mat}]$ can be obtained from the relation

$$[D_{mat}] = \frac{E}{(1-\nu^2)} \begin{bmatrix} 1 & \nu & 0 \\ \nu & 1 & 0 \\ 0 & 0 & \dfrac{(1-\nu)}{2} \end{bmatrix} \tag{3.72}$$

Equation (3.70) can be expressed as

$$U_e = \frac{1}{2}\{U\}_e^T \boldsymbol{K}_e \{U\}_e \tag{3.73}$$

where $\boldsymbol{K}_e$ is the elemental stiffness matrix and has the from

$$\boldsymbol{K}_e = \int h\, \boldsymbol{B}^T [D_{mat}]\, \boldsymbol{B}\, dA \tag{3.74}$$

where

$$\boldsymbol{B} = \frac{1}{4} \begin{bmatrix} -\frac{(1-\eta)}{a} & 0 & \frac{(1-\eta)}{a} & 0 & \frac{(1+\eta)}{a} & 0 & -\frac{(1+\eta)}{a} & 0 \\ 0 & -\frac{(1-\xi)}{b} & 0 & -\frac{(1+\xi)}{b} & 0 & \frac{(1+\xi)}{b} & 0 & \frac{(1-\xi)}{b} \\ -\frac{(1-\xi)}{b} & -\frac{(1-\eta)}{a} & -\frac{(1+\xi)}{b} & \frac{(1-\eta)}{a} & \frac{(1+\xi)}{b} & \frac{(1+\eta)}{a} & \frac{(1-\xi)}{b} & -\frac{(1+\eta)}{a} \end{bmatrix} \tag{3.75}$$

For non-dimensional coordinates of node *j*, the elemental mass matrix can be found from

$$\begin{aligned} \boldsymbol{M}_e &= \rho h\, a\, b \int_{-1}^{1}\int_{-1}^{1} N_i N_j \det[\mathrm{J}]\, d\xi\, d\eta \\ &= \rho h\, a\, b \int_{-1}^{1}\int_{-1}^{1} [N]^T [N] \det[\mathrm{J}]\, d\xi\, d\eta \end{aligned} \tag{3.76}$$

By evaluating (3.76) the elemental mass matrix is obtained as

$$\boldsymbol{M}_e = \frac{\rho h\, a\, b}{9}\begin{bmatrix} 4 & 0 & 2 & 0 & 1 & 0 & 2 & 0 \\ 0 & 4 & 0 & 2 & 0 & 1 & 0 & 2 \\ 2 & 0 & 4 & 0 & 2 & 0 & 1 & 0 \\ 0 & 2 & 0 & 4 & 0 & 2 & 0 & 1 \\ 1 & 0 & 2 & 0 & 4 & 0 & 2 & 0 \\ 0 & 1 & 0 & 2 & 0 & 4 & 0 & 2 \\ 2 & 0 & 1 & 0 & 2 & 0 & 4 & 0 \\ 0 & 2 & 0 & 1 & 0 & 2 & 0 & 4 \end{bmatrix} \tag{3.77}$$

The elemental stiffness matrix for non-dimensional coordinates can be obtained from

$$\boldsymbol{K}_e = \int_{-1}^{1}\int_{-1}^{1} a\; b\; h\; [B]^T [D_{mat}]\, \boldsymbol{B}\; \det[\mathrm{J}]\, d\xi\; d\eta \tag{3.78}$$

where [J] is the Jacobian matrix and can be evaluated from

$$[\mathrm{J}] = \begin{bmatrix} \dfrac{\partial x}{\partial \xi} & \dfrac{\partial y}{\partial \xi} \\ \dfrac{\partial x}{\partial \eta} & \dfrac{\partial y}{\partial \eta} \end{bmatrix} \tag{3.79}$$

For stress distributions of a thin isotropic rectangular plate (see Fig. 3.8), Hooke's law is used to evaluate the stress-strain relationships as

$$\begin{bmatrix} \sigma_{xx} \\ \sigma_{yy} \\ \tau_{xy} \end{bmatrix} = \frac{E}{(1-\nu^2)}\begin{bmatrix} 1 & \nu & 0 \\ \nu & 1 & 0 \\ 0 & 0 & \dfrac{(1-\nu)}{2} \end{bmatrix}\begin{bmatrix} \varepsilon_{xx} \\ \varepsilon_{yy} \\ \varepsilon_{xy} \end{bmatrix} \tag{3.80}$$

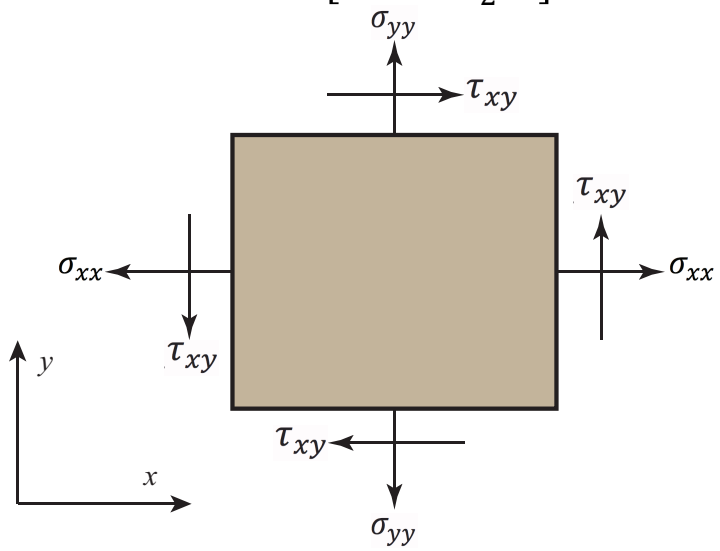

Figure 3.8. Thin Rectangular plate with in-plane stresses

The elemental forcing vector for exterior (boundary) forces can be obtained from

$$\{f\}^e = \int_{\Gamma_{\hat{t}}} h\,[N]^T\,\hat{t}\,d\Gamma_{\hat{t}} \tag{3.81}$$

where $\Gamma_{\hat{t}}$ is the boundary over which tractions are specified, and $\hat{t}$ is the boundary traction. After creating the global stiffness and forces matrices, the boundary conditions were applied to get the reduced global matrices. The boundary conditions were achieved by fixing three nodes in the central element: 6 DOF's, in the *x* and *y* directions. After applying the boundary conditions, the displacement, strain and stresses can be evaluated as follows:

$$\{f_{glob}\} = \boldsymbol{K}_{glob}\,\{U\} \;\Rightarrow\; \{U\} = \boldsymbol{K}_{glob}{}^{-1}\,\{f_{glob}\} \tag{3.82}$$

where $\{U\}$ is the total displacements and has two components of the displacement in the *x* and *y* directions – see (3.65) for one element. Then the strain and stress can be obtained from

$$\{\varepsilon\} = \boldsymbol{B}\,\{U\}, \qquad \{\sigma\} = [D_{mat}]\,\{\varepsilon\} \tag{3.83}$$

Comparing (3.83) with (3.80), the stress vector has the following elements $\sigma_x, \sigma_y\ and\ \tau_{xy}$. These elements represent the normal and shear stresses. They can be used in out-of-plane vibration analysis by evaluating N_x, N_y and N_{xy} (using the expressions below) for each elemental potential energy using (3.57).

$$N_x = \int_{-h/2}^{h/2} \sigma_{xx}\,dz\,;\;\; N_y = \int_{-h/2}^{h/2} \sigma_{yy}\,dz\,;\quad N_{xy} = \int_{-h/2}^{h/2} \tau_{xy}\,dz \tag{3.84}$$

Instead of using the same in-plane forces and uniform stress distributions for all elements, we used non-uniform pre-stress distribution information to evaluate the in-plane forces for each element.

3.2.2 Commercial Software

There are many commercial software based on finite element analysis that solve complex structure problems. One of the best-known commercial software is ANSYS. For out-of-plane vibration analysis, we used pre-stress analysis to examine the non-uniform stress distribution effects on the plate. A 3D shell element was used to mesh a simply supported plate of *2m* length and *1m* width, and a thickness of *0.5mm*. The plate was subjected to in-plane forces as shown in the Fig. 3.9.

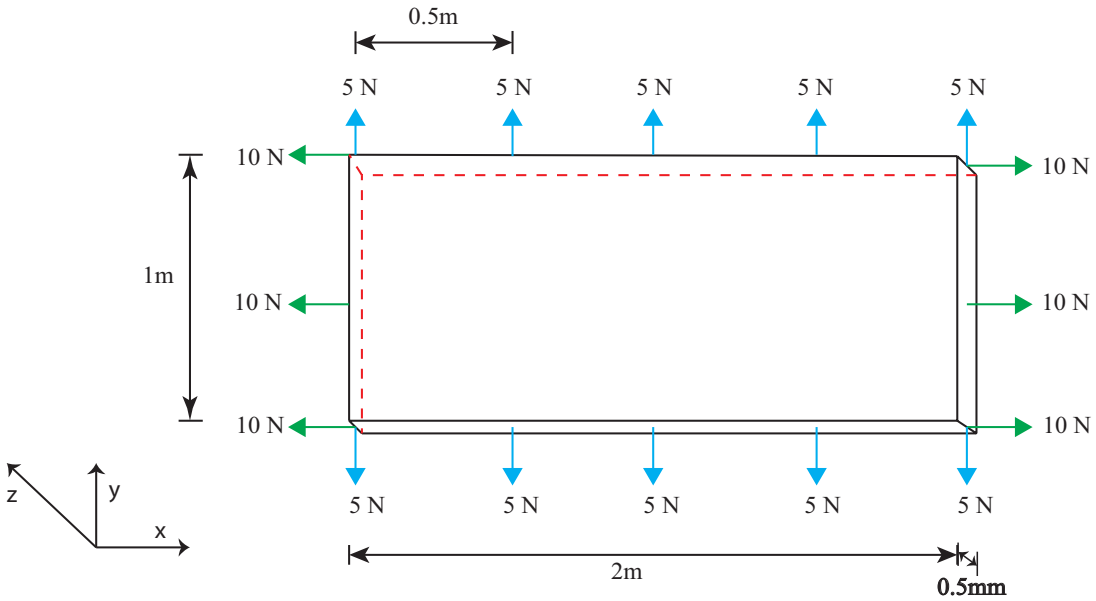

Figure 3.9. Meshing of thin rectangular plate with in-plane prescribed forces

3.2.3 Comparisons

The first five frequencies for the plate shown Fig. 3.9 are listed in Table 3.3. The table presents the results for the case where the in-plane forces are not uniformly distributed. Instead, few discrete in-plane loads are considered. We used commercial FEM software, ANSYS, to verify the results that we got from our MATLAB FEM code for the plate with the meshing shown in Fig. 3.4.

Table 3.3. The Non-Uniform stress distribution frequency results

Mode	ANSYS Hz	MATLAB Hz	% Difference
1	2.3964	2.2915	4.37
2	3.6437	3.5697	2.03
3	5.4468	5.3826	1.17
4	6.2627	5.9567	4.88
5	7.3659	7.0454	4.35

From Table 3.3, we can conclude that the maximum difference between the modal frequencies results was around 4.8%. This could be due to the fact that more DOF's are used in ANSYS discretization. Therefore, the results using our FEM MATLAB code has been proven using multiple methods and the errors remain in the low range, less than 5%, errors. In table 3.2, we saw that our FEM results were higher than the analytical solution. However, table 3.3 shows that our FEM results lower than what we got from the commercial software, which is a good indication that our FEM code has solved the problem with a good accuracy. As presented in sections 3.2.1 and 3.2.2 the solution procedure divided into two parts. In the first part, evaluations for the stress distributions are obtained for both FEM methods and the results are shown in figures below.

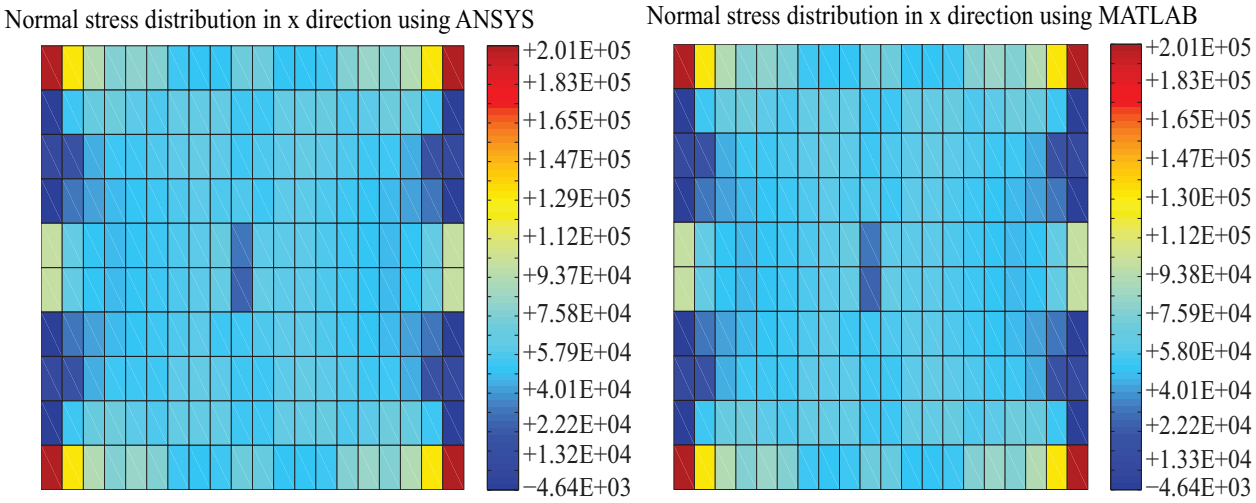

Figure 3.10. In-plane normal stress distribution in the *x* direction

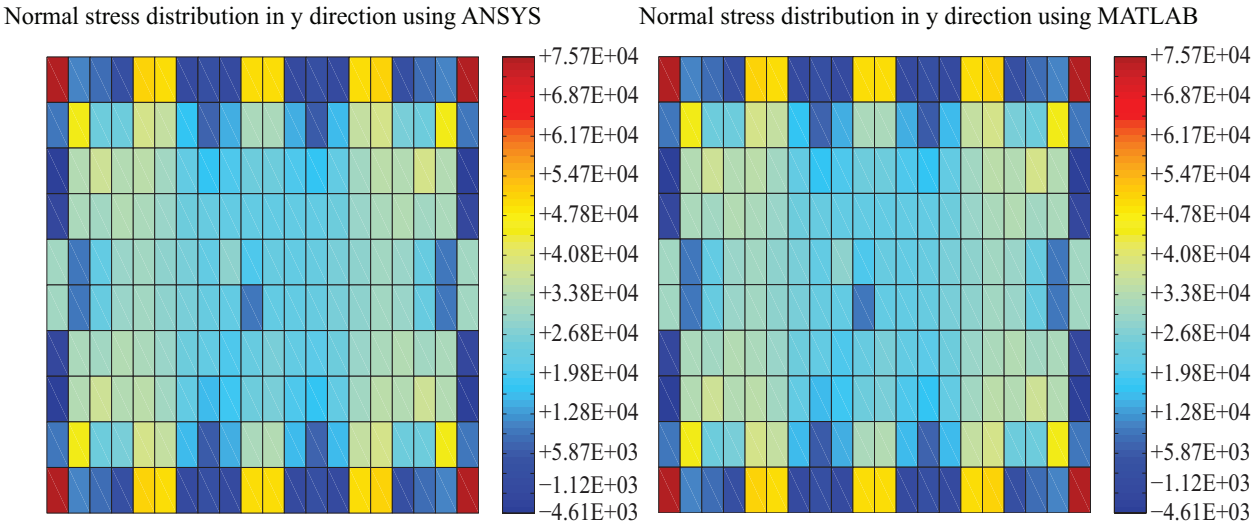

Figure 3.11. In-plane normal stress distribution in the *y* direction

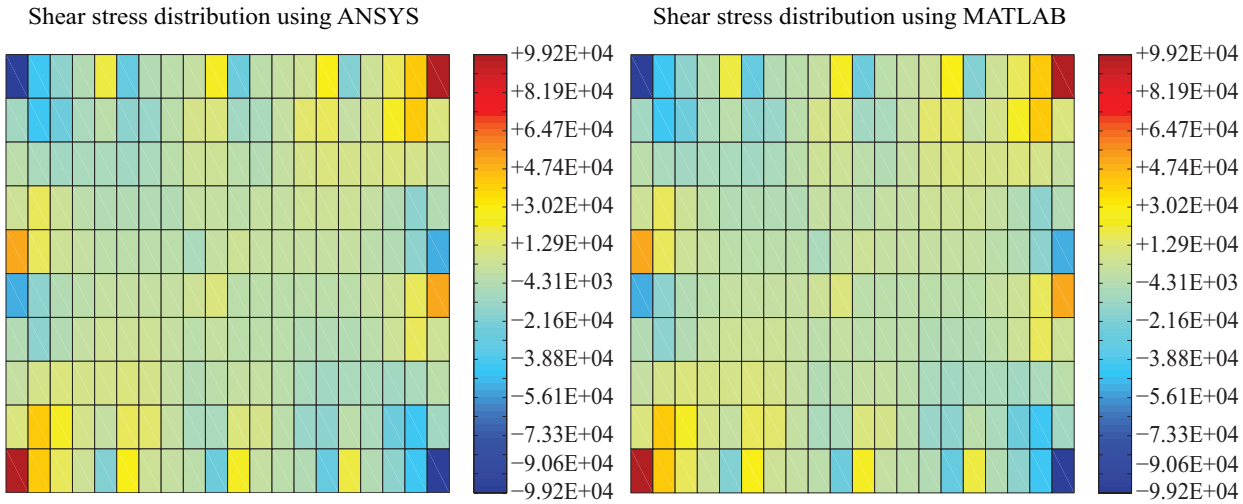

Figure 3.12. In-plane share stress distribution

The difference between our MATLAB Code and the commercial software are shown in the figures below

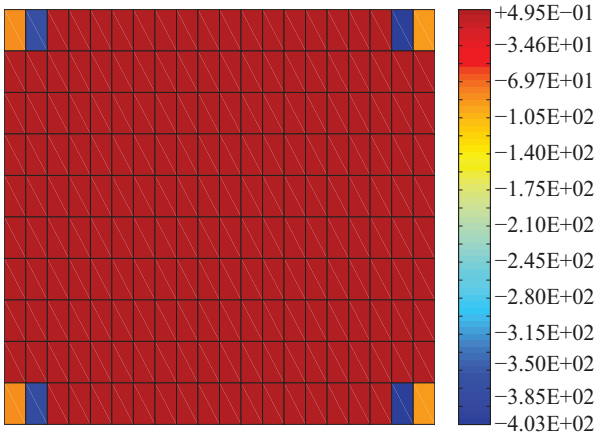

Figure 3.13. Difference between ANSYS and MATLAB Code for the *x* direction stress distribution

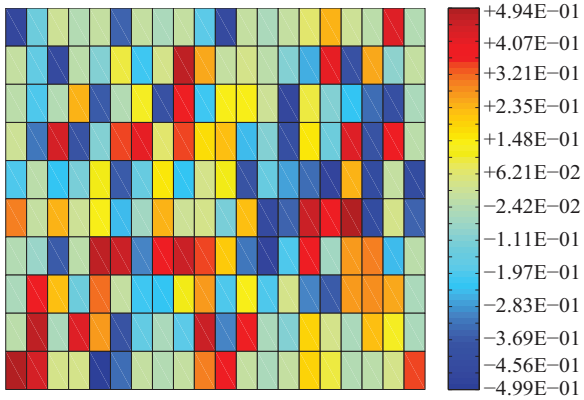

Figure 3.14. Difference between ANSYS and MATLAB Code for the *y* direction stress distribution

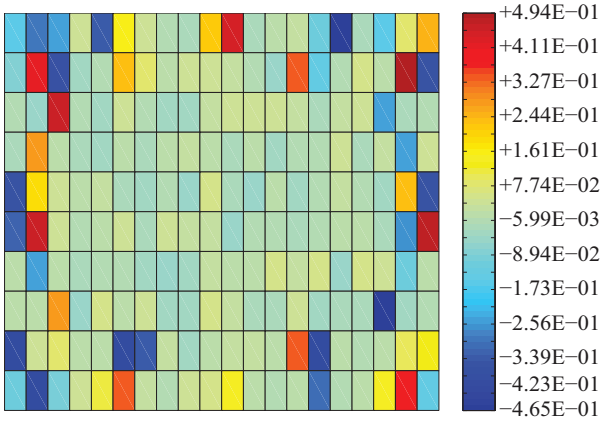

Figure 3.15. Difference between ANSYS and MATLAB Code for the share stress distribution

Figures 3.12, 3.12 and 3.14 show that the ratio between the maximum difference and the maximum normal stress evaluated in the x and y directions and shear stress in xy plane are 2.46×10^{-10}, 6.52×10^{-6} and 4.9798×10^{-6} respectively. These ratio are so small and can be neglected comparing with the maximum stress values that have been evaluated. Using these stress data, an out-of-plane vibration analysis has been made as discussed before and the mode shapes for the frequencies listed in table 3.3 are shown in Fig 3.16.

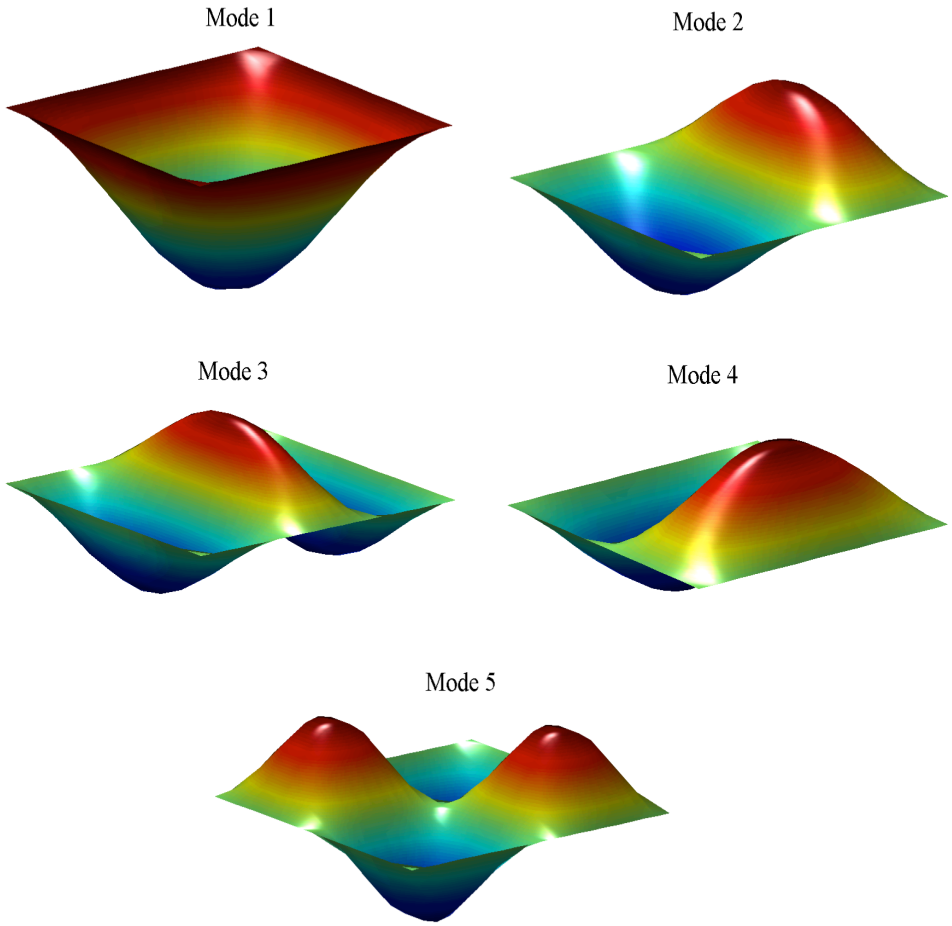

Figure 3.16. First Five modes shapes for thin plate with non-uniform stress distribution

Chapter 4

Vibration Control Of A Thin Rectangular Plate Using Uniformly Distributed In-Plane Forces

In the previous chapters we reviewed the dynamics of a thin rectangular plate with and without in-plane forces, and we showed some techniques to solve the dynamic equations. In this chapter, we introduce a control strategy to reduce the lateral vibration on the plate; it is assumed that the plate is subjected to uniformly distributed in-plane forces. The control strategy uses state feedback and switches the in-plane forces to suppress the vibration. The method presented is an extension of the work by Nudehi [48] where vibration of a beam was suppressed using an end force.

4.1 Control Design

In absence of damping, the equation of motion of a thin rectangular plate subjected to in-plane forces can be expressed in the form

$$\boldsymbol{M}\,\ddot{\mu} + \boldsymbol{K}\,\mu = 0 \tag{4.1}$$

where $\boldsymbol{M} = \rho h\,\boldsymbol{I} \in R^{n\times n}$ is the mass matrix, $\boldsymbol{I} \in R^{n\times n}$ is the identity matrix, $\boldsymbol{K} \in R^{n\times n}$ is the stiffness matrix, and $\mu \triangleq (\mu_1,\ \mu_2, \dots, \mu_n)^T$ are the modal displacements. Using Rayleigh-Ritz Approximation (see section 3.1.2), equation (4.1) can be written as

$$\boldsymbol{M}\,\ddot{\mu} + (\boldsymbol{K_b} + N_x\,\boldsymbol{K_{fx}} + N_y\,\boldsymbol{K_{fy}})\mu = 0 \tag{4.2}$$

where $\boldsymbol{K_b}$ is the stiffness matrix due to bending, and $\boldsymbol{K_{fx}}$ and $\boldsymbol{K_{fy}}$ are the geometric stiffness matrices due to the in-plane forces (N_x and N_y). Assuming the presence of proportional damping (Rayleigh damping), the damping matrix can be expressed as

$$\boldsymbol{D} = \alpha\,\boldsymbol{M} + \beta\,\boldsymbol{K_b} \tag{4.3}$$

Adding the damping effects to (4.2), we get

$$\boldsymbol{M}\,\ddot{\mu} + \boldsymbol{D}\,\dot{\mu} + (\boldsymbol{K_b} + N_x\,\boldsymbol{K_{fx}} + N_y\,\boldsymbol{K_{fy}})\,\mu = 0 \tag{4.4}$$

For the purpose of designing a controller, equation (4.4) is converted to the state space representation as follows:

$$\dot{x_1} = x_2 \tag{4.5}$$

$$\dot{x}_2 = \boldsymbol{M^{-1}}(-\boldsymbol{K_b}\,x_1 - \boldsymbol{D}\,x_2 - \boldsymbol{K_{fx}}\,x_1 u_x - \boldsymbol{K_{fy}}\,x_1 u_y) \tag{4.6}$$

where $x_1 \triangleq \mu \in R^n$ and $x_2 \triangleq \dot{\mu} \in R^n$ are the state variables, and $u_x \triangleq N_x \in R$ and $u_y \triangleq N_y \in R$ are the control inputs. The following choice of inputs

$$\begin{aligned} u_x &= \begin{cases} \overline{N}_x & if\ x_2^T\,\boldsymbol{M^{-1}K_{fx}}\,x_1 \geq 0 \\ 0 & if\ x_2^T\,\boldsymbol{M^{-1}K_{fx}}\,x_1 < 0 \end{cases} \\ u_y &= \begin{cases} \overline{N}_y & if\ x_2^T\,\boldsymbol{M^{-1}K_{fy}}\,x_1 \geq 0 \\ 0 & if\ x_2^T\,\boldsymbol{M^{-1}K_{fy}}\,x_1 < 0 \end{cases} \end{aligned} \tag{4.7}$$

guarantees asymptotic stability of the equilibrium $(x_1, x_2) = (0,0)$. In (4.7), $\overline{N}_x > 0$ and $\overline{N}_y > 0$ are predefined constant values. To verify asymptotic stability of the equilibrium, consider the energy of the plate as the Lyapunov function candidate;

$$V = \frac{1}{2}(x_1^T\boldsymbol{K}\,x_1 + x_2^T\boldsymbol{M}x_2) \tag{4.8}$$

Taking the first derivative of (4.8) and substituting (4.7) gives

$$\dot{V} = x_1^T \boldsymbol{M^{-1}K_b}\, x_2 + x_2^T \boldsymbol{M^{-1}}\left(-\boldsymbol{K_b}\, x_1 - \boldsymbol{D}\, x_2 - \boldsymbol{K_{fx}}\, x_1 u_x - \boldsymbol{K_{fy}}\, x_1 u_y\right)$$

$$= -x_2^T \boldsymbol{M^{-1}D}\, x_2 - x_2^T \boldsymbol{M^{-1}K_{fx}}\, x_1 u_x - x_2^T \boldsymbol{M^{-1}K_{fy}}\, x_1 u_y \qquad (4.9)$$

$$\leq - x_2^T \boldsymbol{M^{-1}D}\, x_2$$

The $\boldsymbol{D}$ and $\boldsymbol{M^{-1}}$ matrices in equation (4.9) are positive definite. As a result, it can be shown that $\dot{V} \leq 0$ and $\dot{V} = 0$ if $x_2 = 0$. Using LaSalle's Theorem we can claim that the origin is asymptotically stable. Furthermore, since V is radially unbounded, the origin is globally asymptotically stable. The control law in (4.7) implies that the in-plane forces will be applied to the system if they reduce the energy of the system; otherwise, they will be zero.

The control law in (4.7) can be used to control the desired modes; however, the control inputs will have high frequencies that can exceed the bandwidth of the actuators. To accommodate this problem following [48], a low-pass filter is used in the control loop to filter these high frequencies without affecting the stability of the system. The outputs of the system $y_1$and y_2 are first defined as follows (see Fig. 4.1)

$$y_1 = -x_2^T \boldsymbol{M^{-1}K_{fx}} x_1$$
$$y_2 = -x_2^T \boldsymbol{M^{-1}K_{fy}} x_1 \qquad (4.10)$$

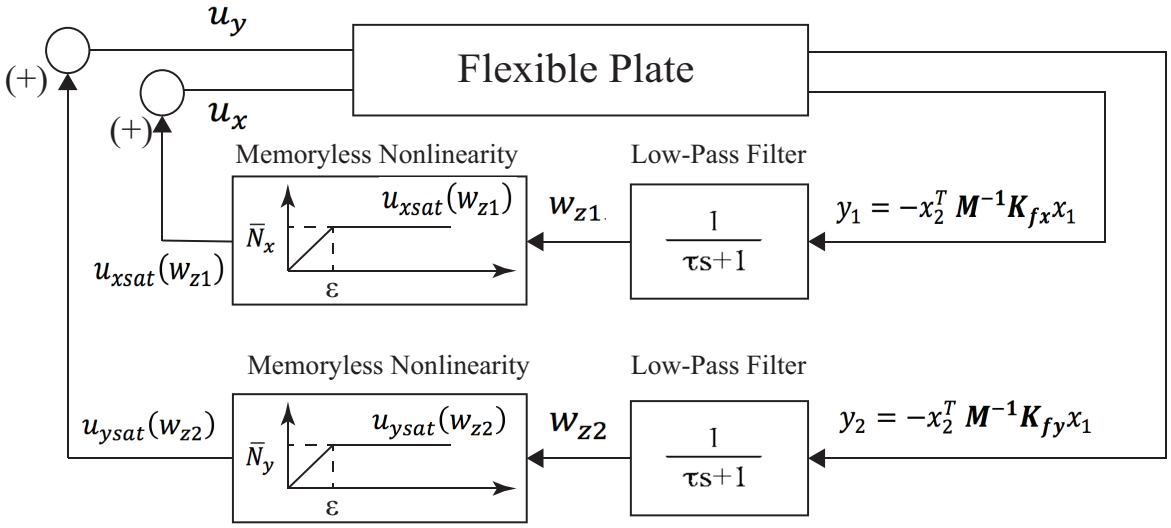

Figure 4.1. Control design based on filtered outputs

The outputs are fed back to the system after it passes through a low-pass filter that has a time constant τ. This filter eliminates the high frequency components of the outputs and provides a signal that does not exceed the actuator bandwidth. The outputs of the filter are denoted as w_{z1} and w_{z2}; therefore, the filter dynamics can be represented as

$$\begin{aligned} \dot{w}_{z1} &= \frac{1}{\tau}(y_1 - w_{z1}) \\ \dot{w}_{z2} &= \frac{1}{\tau}(y_2 - w_{z2}) \end{aligned} \tag{4.11}$$

The outputs of the filters, w_{z1} and w_{z2}, are passed through memoryless nonlinearities $u_{xsat}(\cdot)$ and $u_{ysat}(\cdot)$ respectively such that the control forces do not exceed their predefined maximum values. The saturated inputs can be defined as

$$\begin{aligned} u_{xsat}(w_{z1}) &= \begin{cases} \overline{N}_x & if\ w_{z1} \geq \varepsilon \\ \overline{N}_x \dfrac{w_{z1}}{\varepsilon} & if\ 0 < w_{z1} < \varepsilon \\ 0 & if\ w_{z1} < 0 \end{cases} \\ u_{ysat}(w_{z2}) &= \begin{cases} \overline{N}_y & if\ w_{z2} \geq \varepsilon \\ \overline{N}_y \dfrac{w_{z2}}{\varepsilon} & if\ 0 < w_{z2} < \varepsilon \\ 0 & if\ w_{z2} < 0 \end{cases} \end{aligned} \tag{4.12}$$

where ε is a positive constant. To prove that the dynamic system will remain asymptotically stable after we add the filter and the saturation, we consider the new Lyapunov function candidate;

$$V_{new}(x_1, x_2, w_{z1}, w_{z2}) = \frac{1}{2}(x_1^T \boldsymbol{K_b}\, x_1 + x_2^T M x_2) + \tau \int_0^{w_{z1}} u_{xsat}(\varsigma) d\varsigma \; + \tau \int_0^{w_{z2}} u_{ysat}(\varsigma) d\varsigma \tag{4.13}$$

Using (4.9), its derivative can be found as follows:

$$\dot{V}_{new}(x_1, x_2, w_{z1}, w_{z2}) = -x_2^T \boldsymbol{M^{-1}} \boldsymbol{D} x_2 - x_2^T \boldsymbol{M^{-1}}\, \boldsymbol{K_{fx}}\, x_1 u_x - x_2^T \boldsymbol{M^{-1}}\, \boldsymbol{K_{fy}}\, x_1 u_y + \tau\, u_{xsat}(w_{z1}) \dot{w}_{z1} + \tau\, u_{ysat}(w_{z2}) \dot{w}_{z2} \tag{4.14}$$

Using (4.11), equation (4.14) can be reduced to

$$\begin{aligned} \dot{V}_{new}(x_1, x_2, w_{z1}, w_{z2}) &= -x_2^T \boldsymbol{M^{-1}} \boldsymbol{D} x_2 - y_1 u_x - y_2 u_y + u_{xsat}(w_{z1})(y_1 - w_{z1}) + \\ &\quad u_{ysat}(w_{z2})(y_2 - w_{z2}) \\ &= -x_2^T \boldsymbol{M^{-1}} \boldsymbol{D} x_2 - w_{z1} u_{xsat}(w_{z1}) - w_{z2} u_{ysat}(w_{z2}) \\ &\leq -x_2^T \boldsymbol{M^{-1}} \boldsymbol{D} x_2 \leq 0 \end{aligned} \tag{4.15}$$

Since $\boldsymbol{D}$ and $\boldsymbol{M^{-1}}$ are positive definite, $\dot{V}_{new} \leq 0$. $\dot{V}_{new}$ is equal to zero when $x_2 = 0$. When $x_2 \equiv 0$, we have $y_1 = y_2 = -x_2^T\, \boldsymbol{M^{-1}} \boldsymbol{K_{fx}} x_1 = -x_2^T\, \boldsymbol{M^{-1}} \boldsymbol{K_{fy}} x_1 = 0$, which implies $w_{z1} = w_{z2} = 0$ and $u_{sat}(w_{z1}) = u_{sat}(w_{z2}) = 0$. Using LaSalle's Theorem [Ref], we can therefore claim that the origin is asymptotically stable. To illustrate this control scheme, the state space representation can be rewritten as:

$$\dot{x} = \boldsymbol{A} x \tag{4.16}$$

where

$$\boldsymbol{A} = \begin{bmatrix} 0 & \boldsymbol{I} \\ -\boldsymbol{M^{-1}} \boldsymbol{K_b} - \boldsymbol{M^{-1}} \boldsymbol{K_{fx}}\, u_x - \boldsymbol{M^{-1}} \boldsymbol{K_{fy}}\, u_y & -\boldsymbol{M^{-1}} \boldsymbol{D} \end{bmatrix} \tag{4.17}$$

Equation (4.16) can be expressed as

$$\begin{bmatrix} \dot{x_1} \\ \dot{x_2} \end{bmatrix} = \begin{bmatrix} 0 & I \\ -\boldsymbol{M^{-1}} \boldsymbol{K_b} - \boldsymbol{M^{-1}} \boldsymbol{K_{fx}}\, u_x - \boldsymbol{M^{-1}} \boldsymbol{K_{fy}}\, u_y & -\boldsymbol{M^{-1}} \boldsymbol{D} \end{bmatrix} \begin{bmatrix} x_1 \\ x_2 \end{bmatrix} \tag{4.18}$$

Therefore, the basic system that describes the control scheme is shown below.

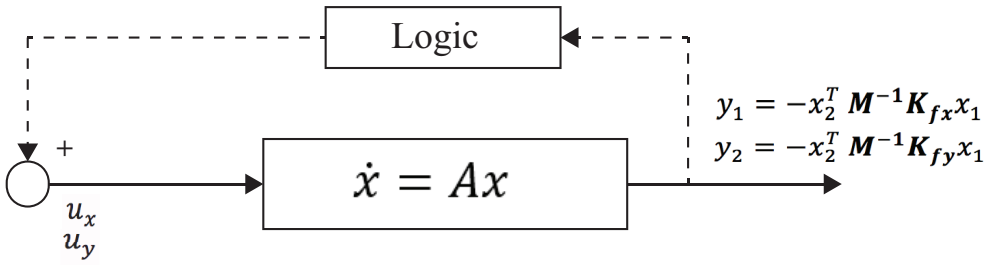

Figure 4.2. Basic system to control the vibration of the rectangular plate

4.2 Control Scheme For A Simply-Supported Plate

The control scheme presented in section 4.1 is applied to the simply supported plate depicted in Fig. 4.3. The plate length, width, and thickness are equal to *L*, *W*, and *h* respectively.

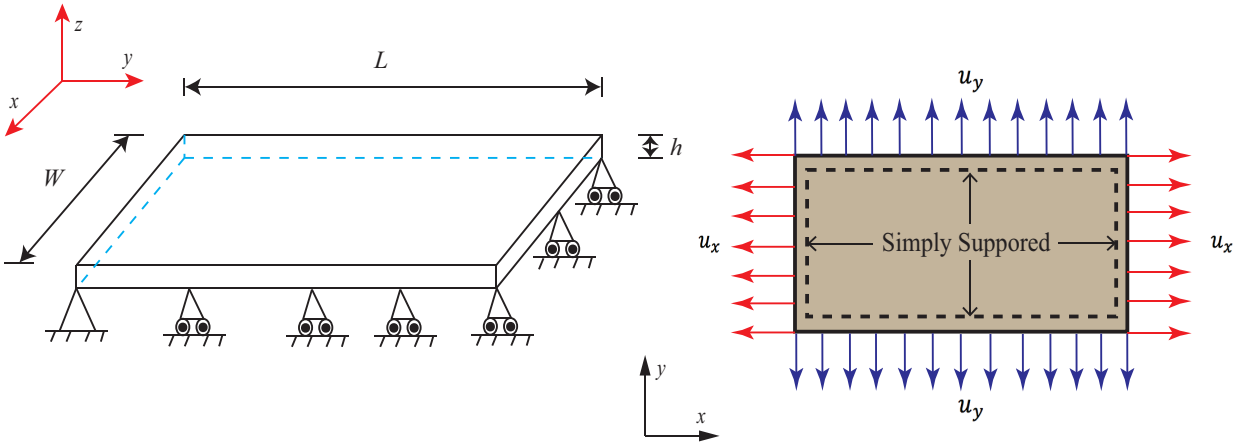

Figure 4.3. Simply supported thin rectangular plate with in-plane distributed forces

The plate is subjected to time-dependent, in-plane forces that are applied according to the control logic in (4.7) for the case without saturation, and according to the control logic in (4.12) for the case with saturation. The control scheme is applied to the mathematical model of the plate obtained using the approximation methods described in chapter 3, namely the Rayleigh-Ritz method and the FEM.

4.2.1 Control Scheme Using Rayleigh-Ritz Approximation

We assume the rectangular plate to have the following geometric and material properties:

Table 4.1. Specifications of the rectangular plate and the controller

Material	Aluminium
Young's modulus, E	70 Gpa
Mass density, ρ	2730 kg/m^3
Passion Ratio, ν	0.35
Damping Ratio, α	0
Damping Ratio, β	0.0002
Length, L	2 m
Width, W	1 m
Thickness, h	0.5 mm
$\overline{N}_x$	10 N
$\overline{N}_y$	5 N

Using the Rayleigh-Ritz method, the first five frequencies of the plate where obtained; these are listed in Table 4.2. The frequencies listed here will not be used in implementation of the controller; it will be compared with the frequencies obtained using FEM for model verification.

Table 4.2. Frequencies in Hz using Rayleigh-Ritz method

Mode	Freq. in Hz for $N_x = 0$ and $N_y = 0$	Freq. in Hz for $N_x = 10N$ and $N_y = 0$	Freq. in Hz for $N_x = 0$ and $N_y = 5N$	Freq. in Hz for $N_x = 10N$ and $N_y = 5N$
1	1.53088	1.6748	1.8063	1.92765
2	2.44912	2.8000	2.6314	2.9568
3	3.98001	4.4706	4.0965	4.56859
4	6.12353	6.2525	6.5493	6.55641
5	6.12353	6.2756	6.6199	6.76247

To investigate the efficacy of the control strategy, we first examine the variation of the energy and the first five modal displacements in the absence of control. The simulation results are shown in Figs. 4.4 and 4.5 for the following initial conditions:

$$\{x_0,\ \dot{x}_0\}^T = \{1 \quad 0.2 \quad 0.5 \quad 0.02 \quad 0.25 \quad 0 \quad 0 \quad 0 \quad 0 \quad 0\}^T \tag{4.19}$$

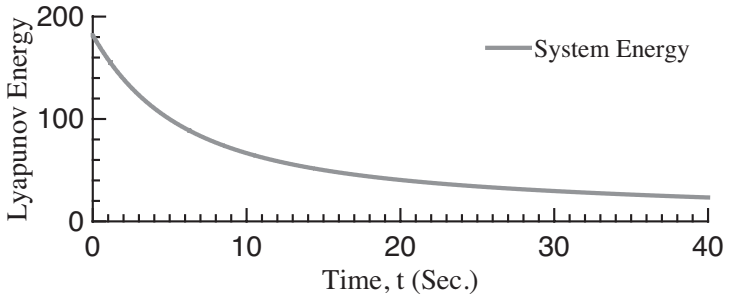

Figure 4.4. Energy deception for simply-supported plate without the controlled in-plane forces using Rayleigh-Ritz approximation

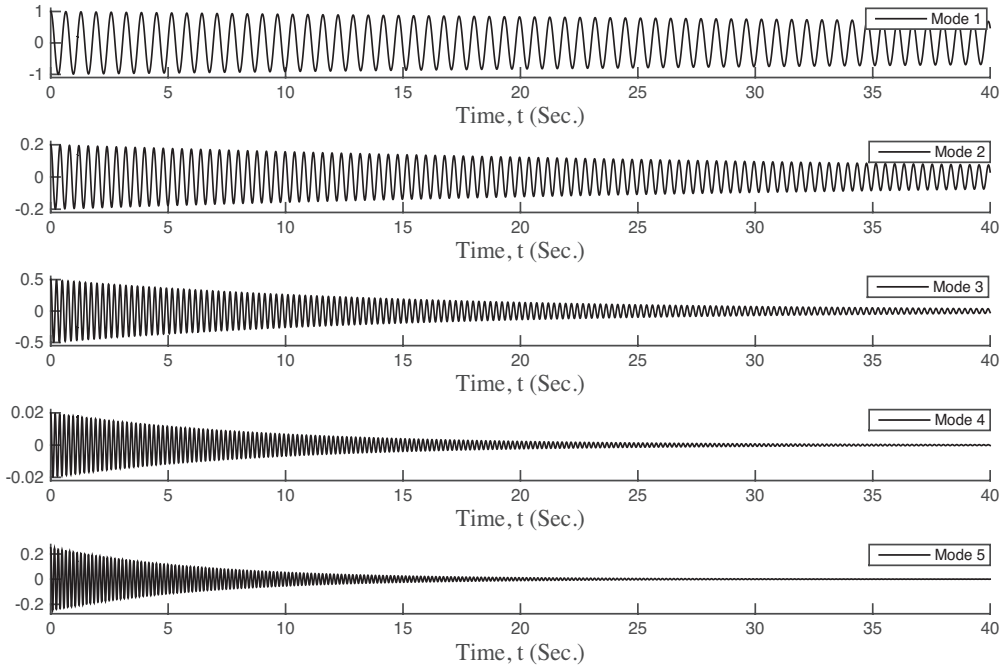

Figure 4.5. Modal displacements for simply supported plate without the controlled in-plane forces using Rayleigh-Ritz approximation

From Figs. 4.4 and 4.5 we observe that the energy of the system and the modal displacements do not converge to zero in 40 seconds. This is due to the fact that the plate has low damping. We now examine the variation of energy and the first five modal displacements for the controlled system based on the control logic in (4.7). The results are shown in Figs. 4.6 and 4.7.

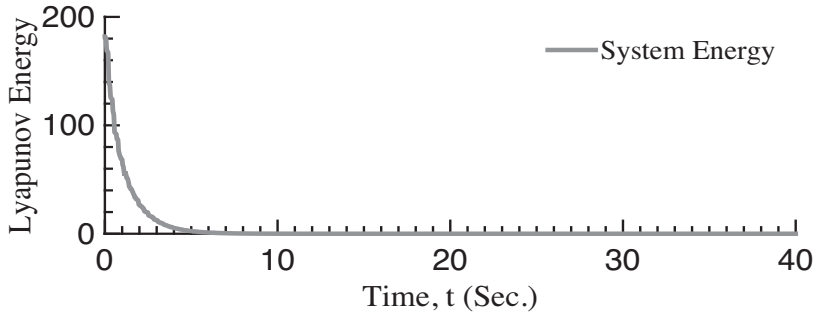

Figure 4.6. Energy deception for simply supported plate with controlled in-plane forces using Rayleigh-Ritz approximation

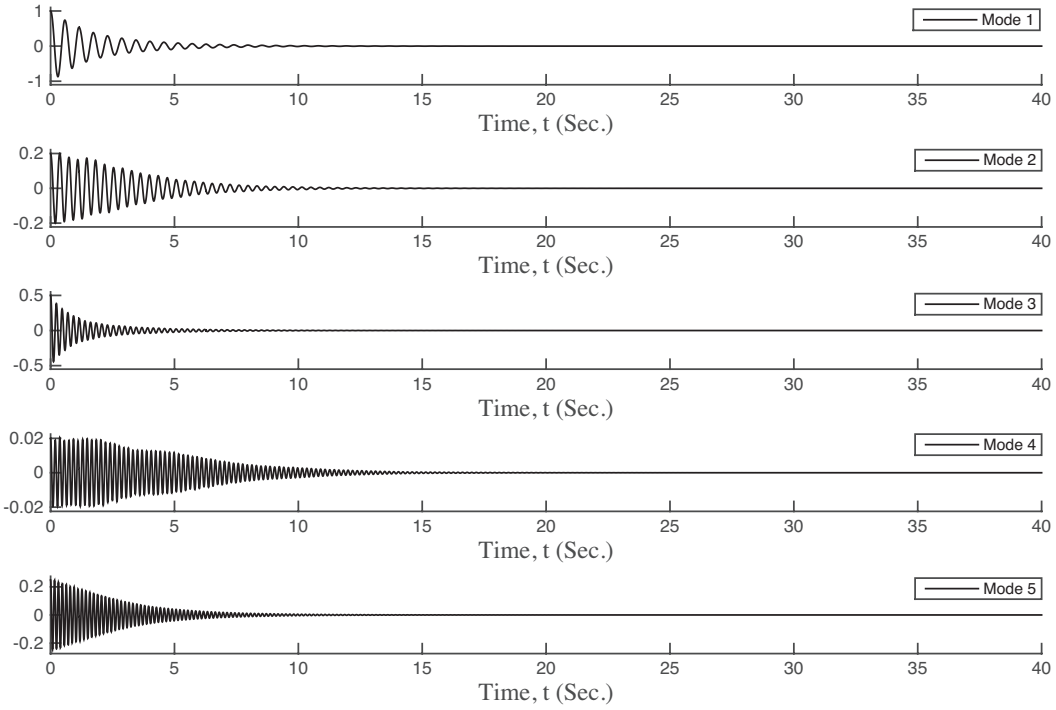

Figure 4.7. Modal displacements for simply supported plate with controlled in-plane forces using Rayleigh-Ritz approximation

Figures 4.6 and 4.7 show that the energy and the modal dispalcements are converged to zero in approximately 6 secondes. These results demonstrate the efficacy of the control. The controlled forces that are used to suppress the vibration are shown in Figs. 4.8 and 4.9.

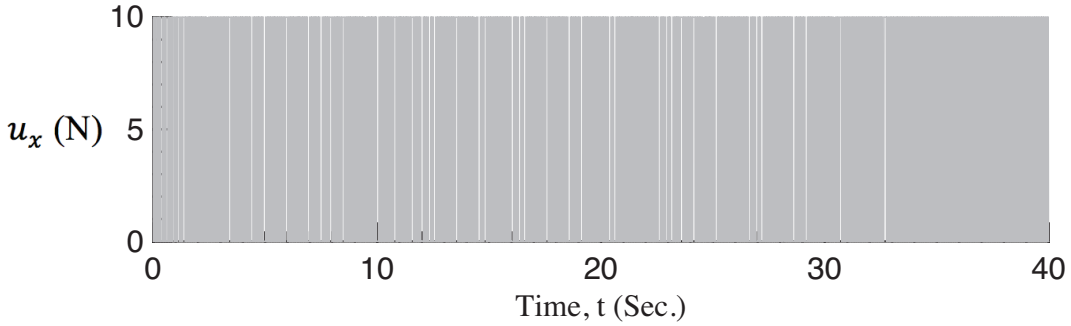

Figure 4.8. u_x inputs for simply supported plate using Rayleigh-Ritz approximation

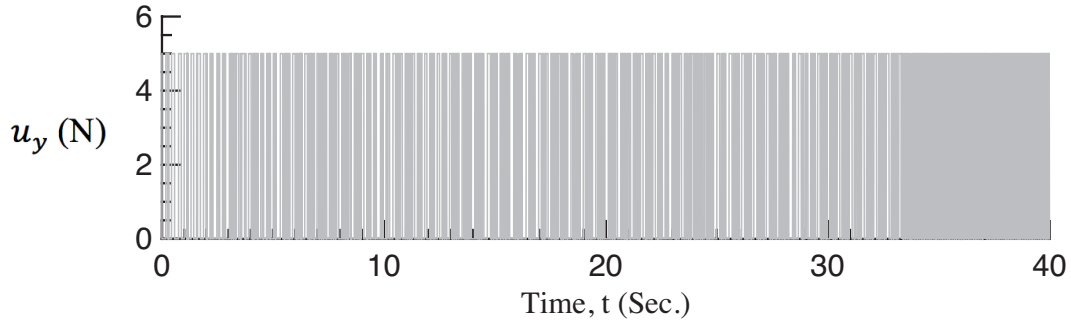

Figure 4.9. u_y inputs for simply supported plate using Rayleigh-Ritz approximation

It can be observed form Figs. 4.8 and 4.9 that the control inputs switch with high frequency. Furthermore, the control inputs keep switching even after the plate vibration has subsided. To address these problems, we implement the control logic in (4.12) – the results are shown in Figs. 4.10 – 4.14. The time constant for the filter and the saturation constant for the modified control are listed in Table 4.3.

Table 4.3. Modified control constants

Time constant, τ	0.15
ε, for saturation	0.5

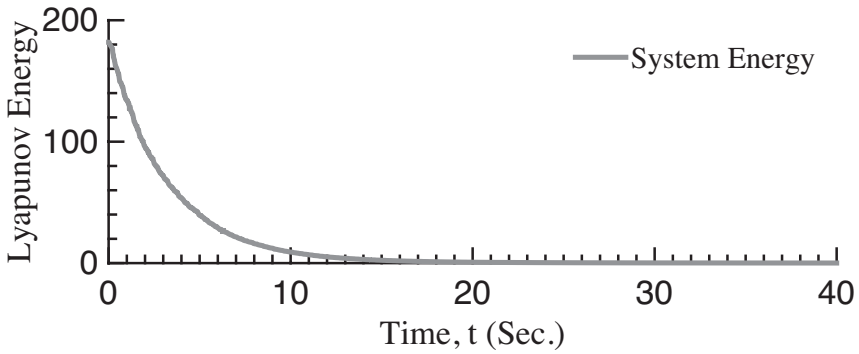

Figure 4.10. Energy deception for simply supported plate with modified controlled in-plane forces using Rayleigh-Ritz approximation

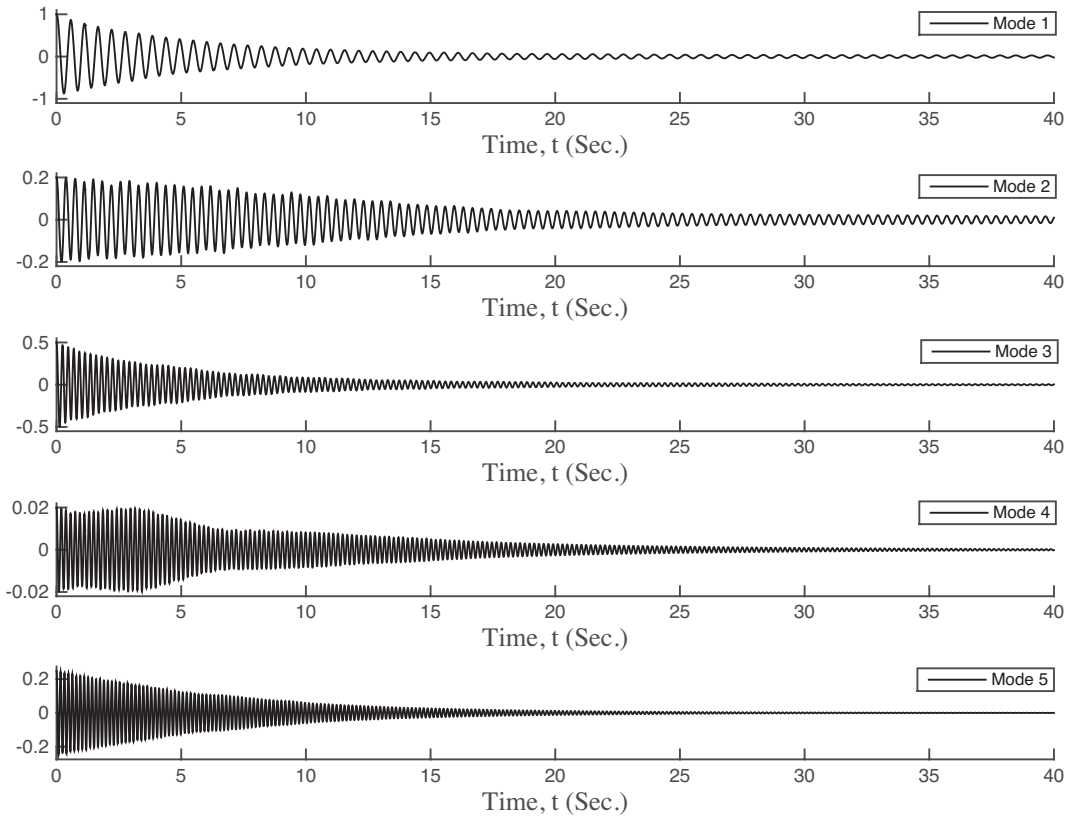

Figure 4.11. Modal displacements for simply supported plate with modified control using Rayleigh-Ritz approximation

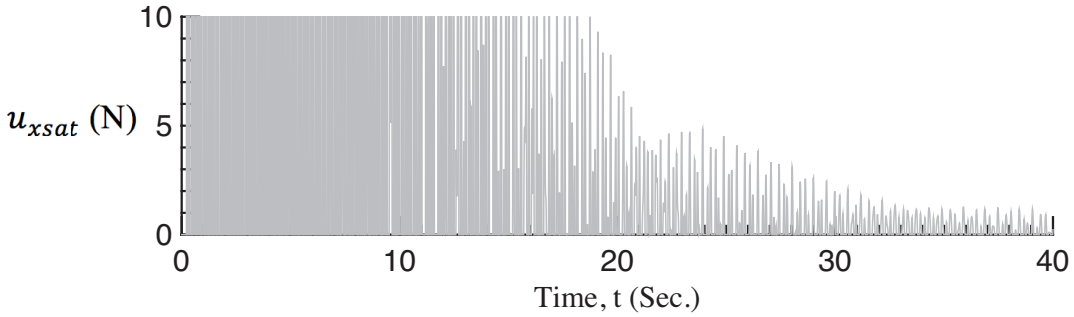

Figure 4.12. Modified control inputs u_{xsat} for simply supported plate using Rayleigh-Ritz approximation

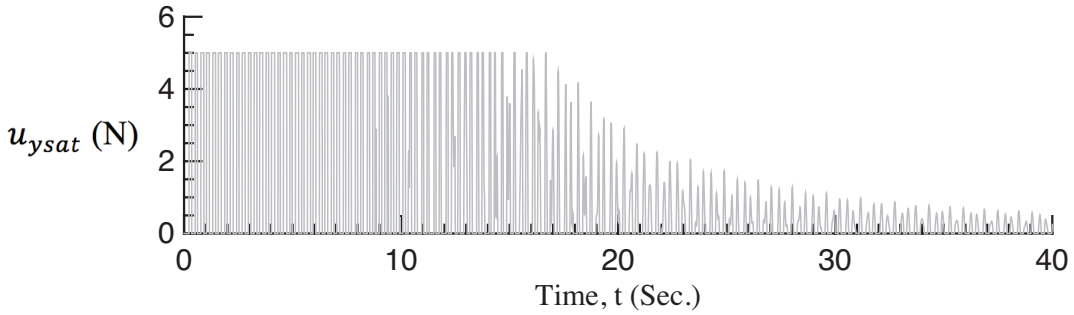

Figure 4.13. Modified control inputs u_{ysat} for simply supported plate using Rayleigh-Ritz approximation

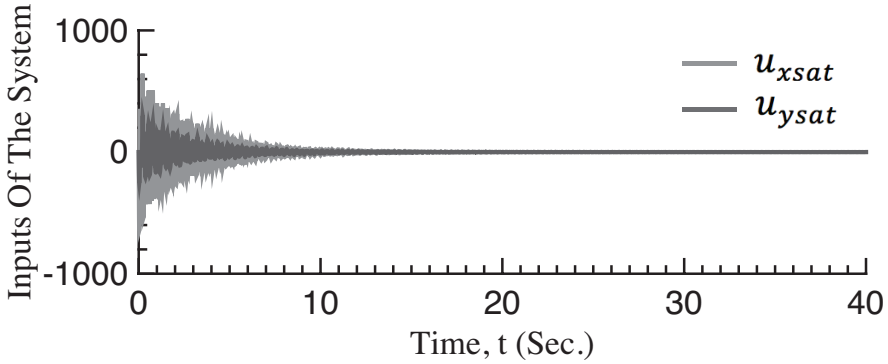

Figure 4.14. Modified control filter input for simply supported plate using Rayleigh-Ritz approximation

From the results shown in Figs. 4.6 – 4.13, we observe that the control scheme with filter and saturation (4.12) takes longer time to suppress the vibration of the plate compared with the control scheme without the filter and saturation (4.7). However, the input forces have lower switching frequency and converge to zero as the vibration subsides.

4.2.2 Control Scheme Using Finite Element Analysis

For the plate shown in Fig. 4.3 and the properties listed in Table 4.1, FEM analysis is used to model the plate dynamic (see chapter 3). The plate is discretized to 20 elements along the *x*-direction and 10 elements along the *y*-direction - see Fig. 3.4. The first five frequencies are listed in Table 4.4 for different combination of N_x and N_y.

Table 4.4. Frequencies in Hz using Finite Element Analysis

Mode	Freq. in Hz for $N_x = 0$ and $N_y = 0$	Freq. in Hz for $N_x = 10N$ and $N_y = 0$	Freq. in Hz for $N_x = 0$ and $N_y = 5N$	Freq. in Hz for $N_x = 10N$ and $N_y = 5N$
1	1.5531	1.6941	1.8242	1.9456
2	2.5045	2.8467	2.6810	3.0032
3	4.0590	4.5383	4.1702	4.6380
4	6.2190	6.3647	6.5070	6.6461
5	6.2193	6.7824	6.5745	6.8495

Comparing Table 4.4 with Table 4.2, we observe that the modal frequeceies obtained using the Rayleigh-Rtiz method are closed those obtained using FEM with reasonable difference (1%). To simulate the control scheme using FEM dynamic model, we should first perform a model reduction. This is because the mass and stiffness matrices obtained using FEM have a dimension much higher than those obatined using Rayleigh-Ritz method. Model reduction will allow us to control the vibration in a few modes of the system in a computationally efficient manner. Modal analysis is used to reduce the order of the system and transfer it to the state space representation. The governing equation for the freely vibrating system has the following form with absence of damping:

$$\boldsymbol{M}\ddot{\mu} + \boldsymbol{K}\mu = 0 \tag{4.20}$$

where $\mu \in R^n$ is the vector of the physical coordinate. Solving eigenvalue problem for (4.20), we get

$$(\boldsymbol{K} - \lambda\, \boldsymbol{M})[\emptyset] = 0 \tag{4.21}$$

We define the physical coordinates μ in terms of the model coordinate x using the relation

$$\boldsymbol{\mu} = [\emptyset]\, \boldsymbol{x} \tag{4.22}$$

where $[\emptyset]$ is the matrix of eigenvectors. Substitution of (4.22) in to (4.20) gives

$$\boldsymbol{M}[\emptyset]\, \ddot{x} + \boldsymbol{K}[\emptyset]\, x = 0 \tag{4.23}$$

Multiply (4.23) by $[\emptyset]^T$, we get

$$[\emptyset]^T \boldsymbol{M}[\emptyset]\ddot{x} + [\emptyset]^T \boldsymbol{K}[\emptyset]x = 0 \tag{4.24}$$

where

$$[\emptyset]^T \boldsymbol{M}[\emptyset] = I \tag{4.25}$$

$$[\emptyset]^T \boldsymbol{K}[\emptyset] = \begin{bmatrix} \lambda_1 & 0 & \dots & 0 \\ 0 & \ddots & 0 & \vdots \\ \vdots & 0 & \ddots & 0 \\ 0 & \cdots & 0 & \lambda_n \end{bmatrix} \tag{4.26}$$

Equation (4.23) can be written as

$$\ddot{x} + [\Lambda]x = 0 \tag{4.27}$$

where $[\Lambda] = diag(\lambda_i)$, and $i = 1, 2, \dots., n$. Using (4.27), we decouple our system to multiple equations that have the following form:

$$\ddot{x}_j + \left[\Lambda_j\right] x_j = 0 \qquad j = 1, 2, .., n \tag{4.28}$$

The proportional damping is used to obtain the damping matrix as

$$\boldsymbol{D} = \alpha\, \boldsymbol{I} + \beta\, [\Lambda] \tag{4.29}$$

Adding damping effect to (4.28), we get

$$\ddot{x}_j + \left(\alpha + \beta\left[\Lambda_j\right]\right)\dot{x}_j + \left[\Lambda_j\right]x_j = 0 \qquad j = 1, 2, .., n \tag{4.30}$$

After using the modal reduction, our system is decoupled into *n* equations. The first five equations from (4.30) are used to form the dynamic model that are used in the control scheme. The results for the control logic in (4.7) using the initial conditions in (4.19) are shown in the

Figs. 4.15 – 4.18.

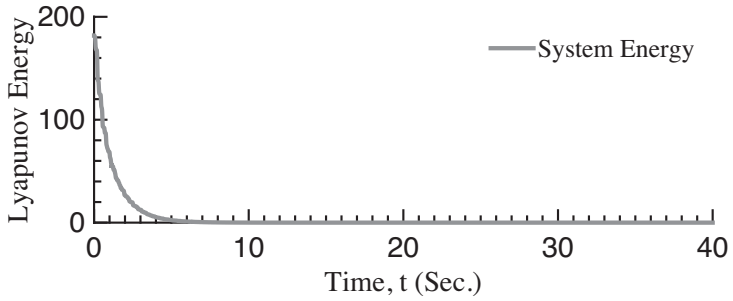

Figure 4.15. Energy deception for simply supported plate with controlled in-plane forces using FEM approximation

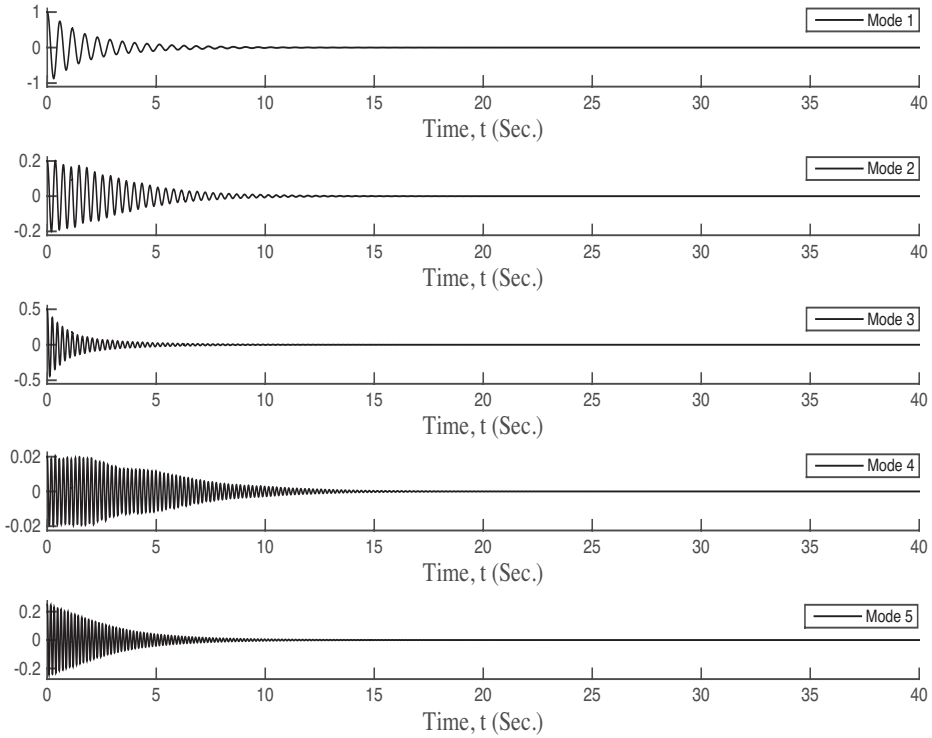

Figure 4.16. Modal displacements for simply supported plate with controlled in-plane forces using FEM approximation

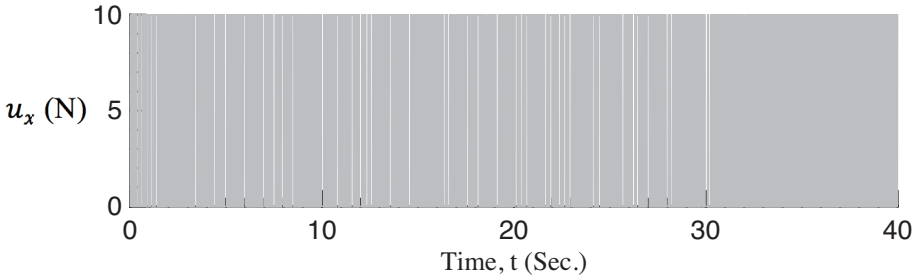

Figure 4.17. u_x input for simply supported plate using FEM approximation

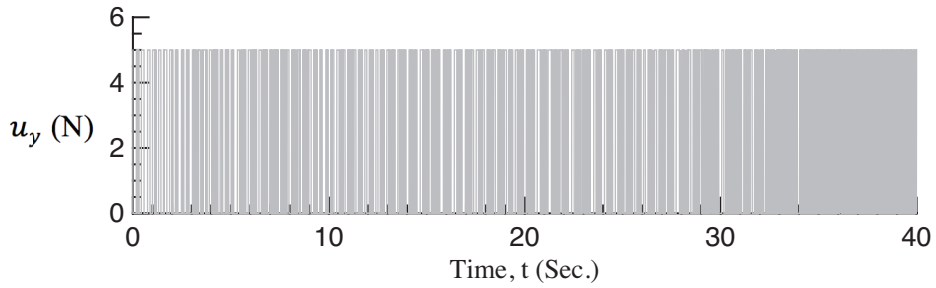

Figure 4.18. u_y input for simply supported plate using FEM approximation

For the modified control scheme using filter and saturation (4.12), the results are shown in Figs. 4.19 – 4.23; the time and saturation constants are listed in Table 4.3. Once again, it can be observe that the control logic in (4.12) are taking more time to suppress the vibration.

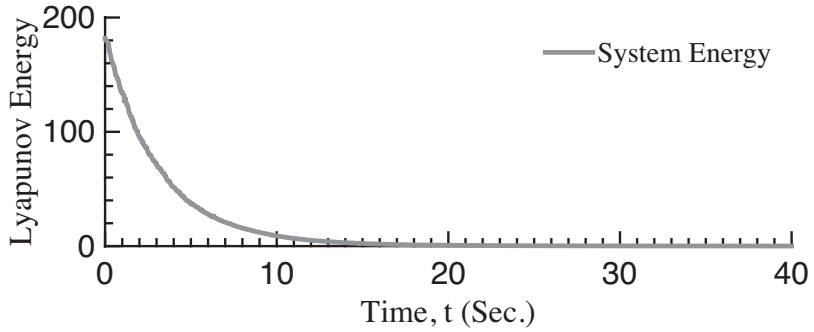

Figure 4.19. Energy deception for simply supported plate with modified controlled in-plane forces using filter and saturation for FEM approximation

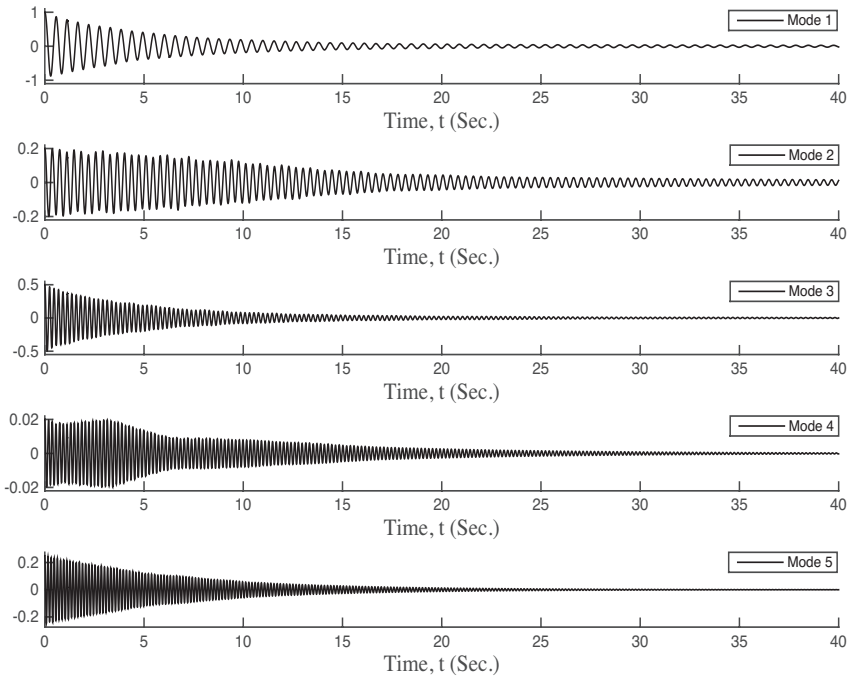

Figure 4.20. Modal displacements for simply supported plate with modified controlled in-pane forces using FEM approximation

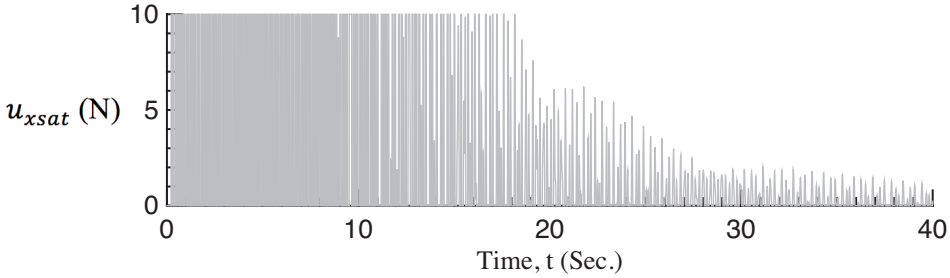

Figure 4.21. Modified control inputs u_{xsat} for simply supported plate for FEM approximation

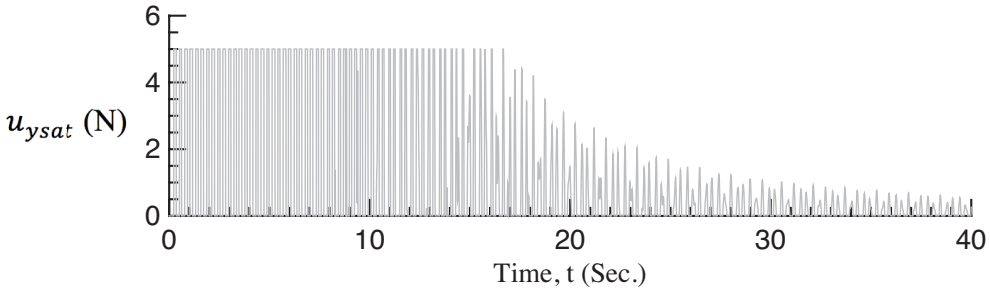

Figure 4.22. Modified control inputs u_{ysat} for simply supported plate for FEM approximation

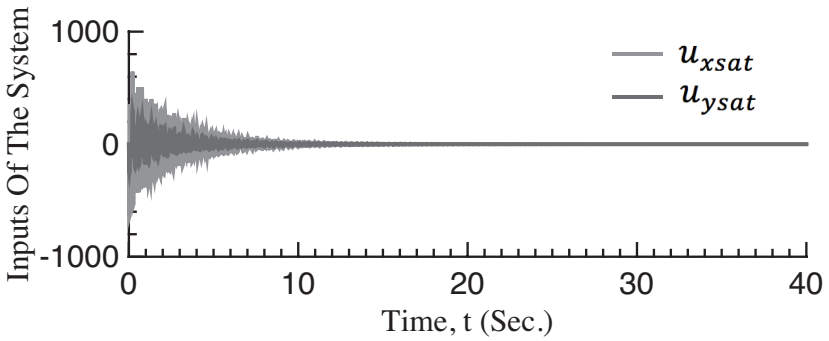

Figure 4.23. Filter inputs for simply supported plate with modified controlled in-plane forces using for FEM approximation

4.2.3 Comparisons

In this section, we investigated the efficacy of the control strategy that is presented in section 4.1 for simply supported rectangular plate using two approximation methods (Rayleigh-Ritz method and FEM). The results are shown in Figs. 4.6 – 4.14 using Rayleigh-Ritz method and in Figs. 4.15 – 4.23 using FEM. Comparing these two sets of results, we observe that they are identical using both control logics (with and without modification using filter and saturation). Therefore, either method can be used to accurately simulate the control scheme in section 4.1. For both method, the energy converge to zero within approximately 5 seconds using the control logic in (4.7); the time required for convergence jumps up to 15 seconds with the control logic using filter and saturation (4.12). This is a price we have to pay to reduce the bandwidth requirement for the actuator: the in-plane forces used in the modified control logic have lower switching frequency and they converge to zero as the vibration of the system decays out.

4.3 Control Scheme For A Plate With Elastic Boundary Conditions

In this section, the effect of changing the boundary conditions is investigated. A plate with uniformly distributed springs around the boundaries is studied – see Fig. 4.24.

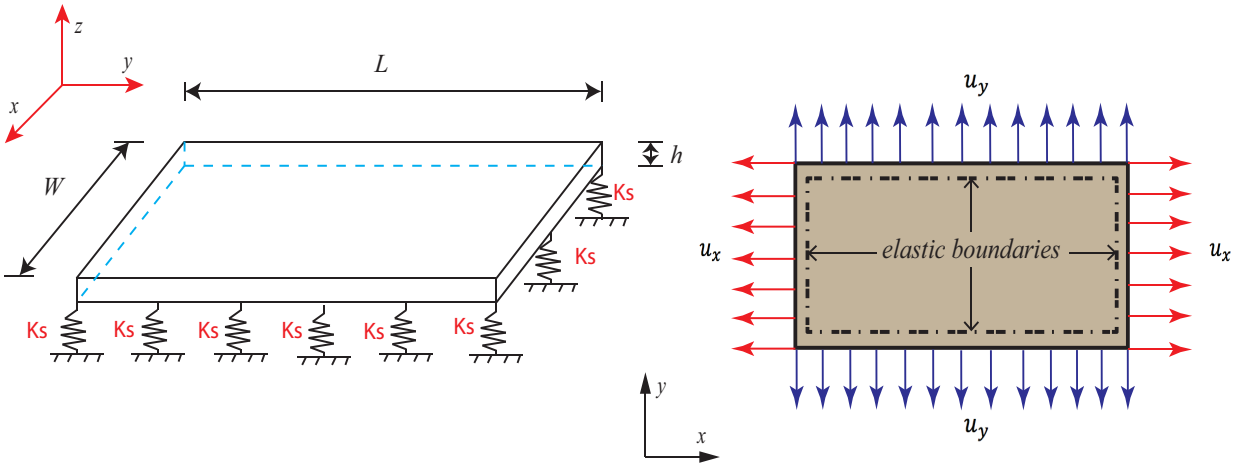

Figure 4.24. Thin rectangular plate with in-plane distributed forces and elastic boundary conditions

The plate length, width, and thickness are labeled as L, W, and h respectively, and K_s represents the stiffness constant for uniformly distributed boundary springs. Using elastic boundary condition converts the problem boundary into a general case that can reproduce other boundary conditions. For instance, the previous case (simply supported boundary conditions) can be obtained by assigning a very large stiffness constant. In addition, using different values for the stiffness constant alter the stiffness matrix of the system that can change the dynamic behavior. The plate is subjected to time-dependent, in-plane uniformly distributed forces that are applied according to the control scheme presented in section 4.1. The control scheme is applied after the dynamic model of the system is obtained using an approximation method, i.e., the mass; damping; and stiffness matrices are obtained. The FEM is used together with model reduction to model these matrices (where the stiffness constants K_s are added to their associated degrees of

freedom in the global stiffness matrix) in this section due to the limitation of the Rayleigh-Ritz method (see chapter 3).

4.3.1 Verify The Solution Using Elastic Boundary Conditions

To verify the elastic boundary condition results, a special case is considered by assigning a large stiffness constant K_s. Therefore, the problem will be similar to the simply supported boundary condition. For a plate that has a properties listed in Table 4.1, the frequency analysis using different forcing combination are shown in the table below.

Table 4.5. Frequencies in Hz using FEM method for elastic boundary condition with $K_s = 10^6\ N/m$

Mode	Freq. in Hz for $N_x = 0$ and $N_y = 0$	Freq. in Hz for $N_x = 10N$ and $N_y = 0$	Freq. in Hz for $N_x = 0$ and $N_y = 5N$	Freq. in Hz for $N_x = 10N$ and $N_y = 5N$
1	1.5531	1.6941	1.8242	1.9456
2	2.5045	2.8467	2.6810	3.0032
3	4.0590	4.5383	4.1702	4.6380
4	6.1290	6.3647	6.5921	6.6461
5	6.1293	6.4782	6.6270	6.8495

Comparing the results listed in Table 4.5 and Table 4.4, we observe that they are close to each other, which prove our previous claim (the elastic boundary condition is a general case that can reproduce other boundary conditions).

4.3.2 Control Scheme Using Finite Element Analysis

A plate with an elastic boundary condition as shown in Fig. 4.24 is studied, the stiffness constant K_s is set to be $100\ N/m$. The frquency analysis for the plate with the properties listed in Table 4.1 are shown in Table 4.6.

Table 4.6. Frequencies in Hz using Finite Element Analysis for elastic boundary condithins and $K_s = 100\ N/m$

Mode	Freq. in Hz for $N_x = 0$ and $N_y = 0$	Freq. in Hz for $N_x = 10N$ and $N_y = 0$	Freq. in Hz for $N_x = 0$ and $N_y = 5N$	Freq. in Hz for $N_x = 10N$ and $N_y = 5N$
1	1.5379	1.6772	1.8041	1.9242
2	2.4633	2.8014	2.6338	2.9525
3	3.9737	4.4446	4.0773	4.5376
4	6.0603	6.1680	6.1247	6.4305
5	6.0289	6.6086	6.2971	6.6678

Comparing Table 4.5 with 4.6, we observe that the frequencies are decreased as we reduced the stiffness constant K_s. The control scheme (section 4.1) is applied after we obtained the model dynamics using FEM to investigate the efficacy of the control logic. The results for the control scheme using the initial conditions in (4.19) are shown in Figs. 4.27 – 4.35.

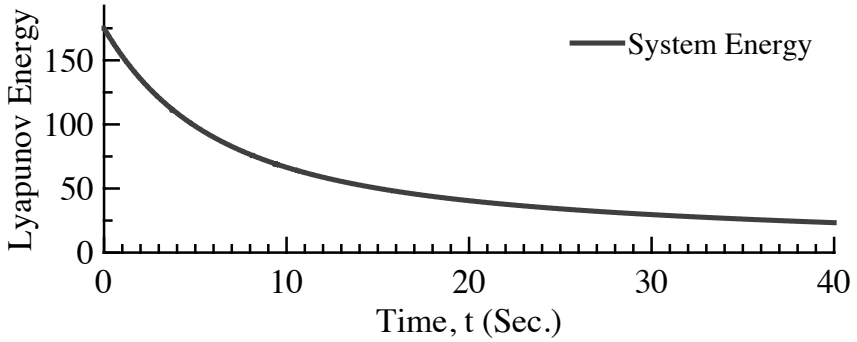

Figure 4.25. Energy deception for elastic boundary condition without in-plane forces and $K_s = 100\ N/m$ using FEM approximation

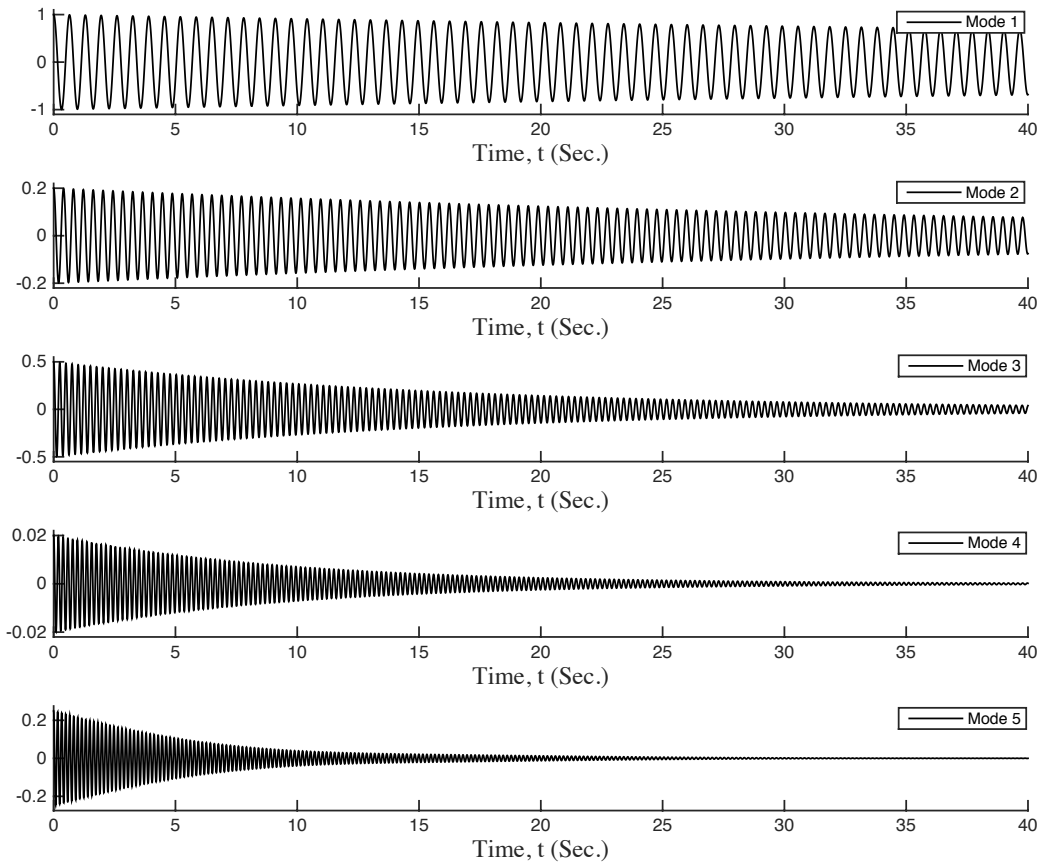

Figure 4.26. Modal displacements for elastic boundary condition without in-plane forces and $K_s = 100\ N/m$ using FEM approximation

Comparing Figs. 4.25 and 4.26 with 4.3 and 4.4, we observe that the system total energy is reduced by using the elastic boundary conditions.

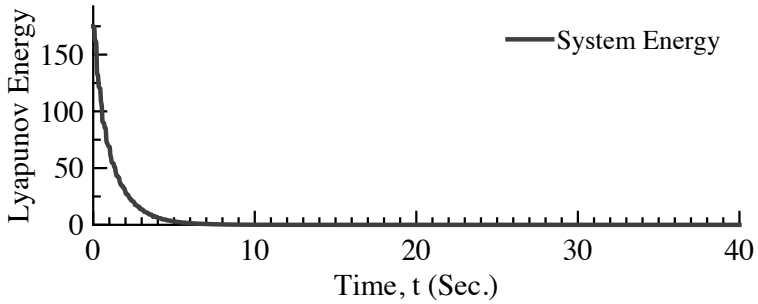

Figure 4.27. Energy deception for elastic boundary condition with controlled in-plane forces and $K_s = 100\ N/m$ using FEM approximation

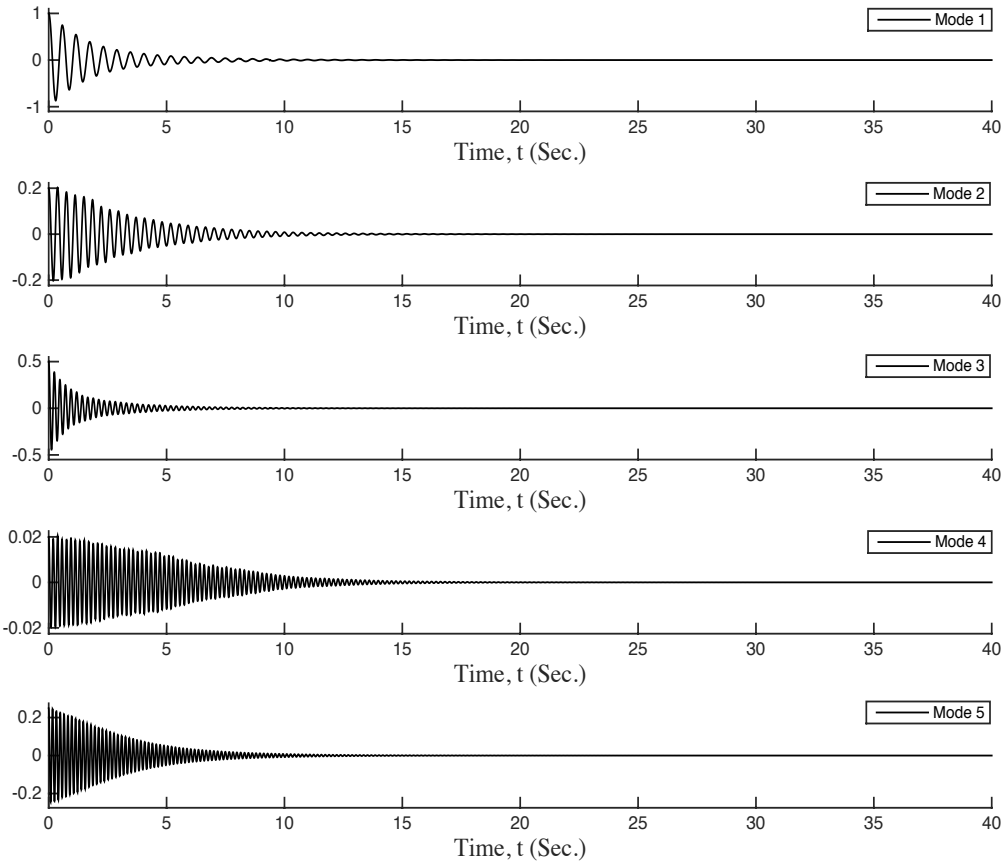

Figure 4.28. Modal displacements for elastic boundary condition with controlled in-plane forces and $K_s = 100\ N/m$ using FEM approximation

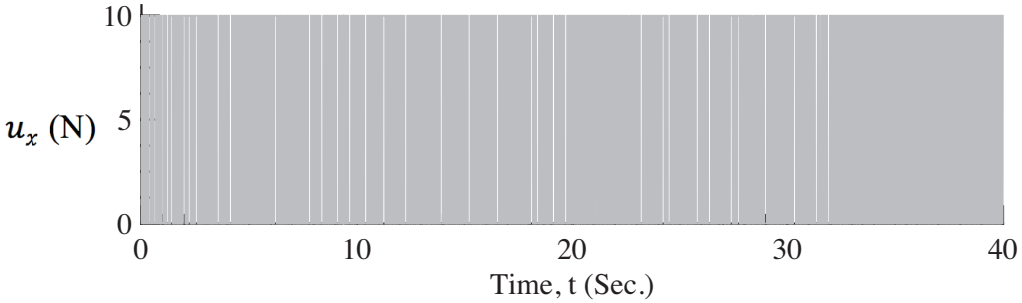

Figure 4.29. u_x inputs for a plate with elastic boundary condition and $K_s = 100\ N/m$ using FEM approximation

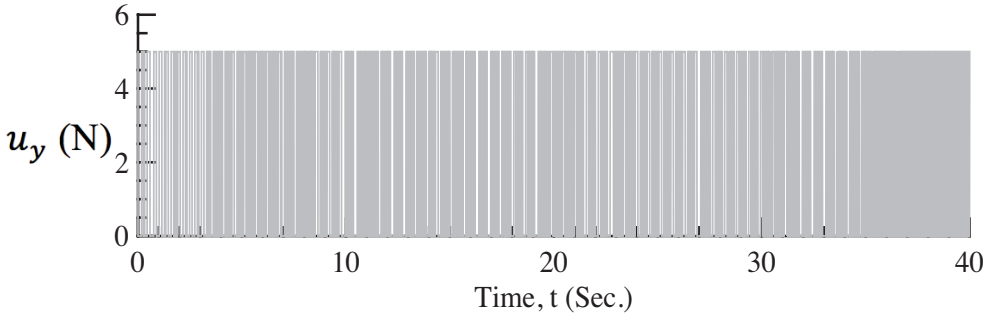

Figure 4.30. u_y inputs for a plate with elastic boundary condition and $K_s = 100\ N/m$ using FEM approximation

Applying the modified control logic (4.12) using the filter and saturation with the properties listed in Table 4.3, the results are shown in the Figs. 4.31 – 4.35.

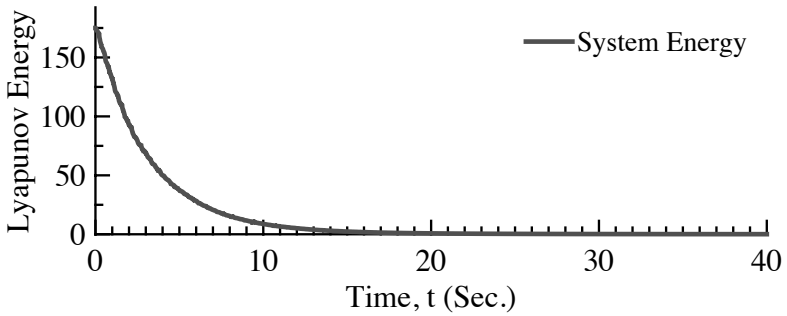

Figure 4.31. Energy deception for plate with elastic boundary condition and $K_s = 100\ N/m$ using modified controlled in-plane forces

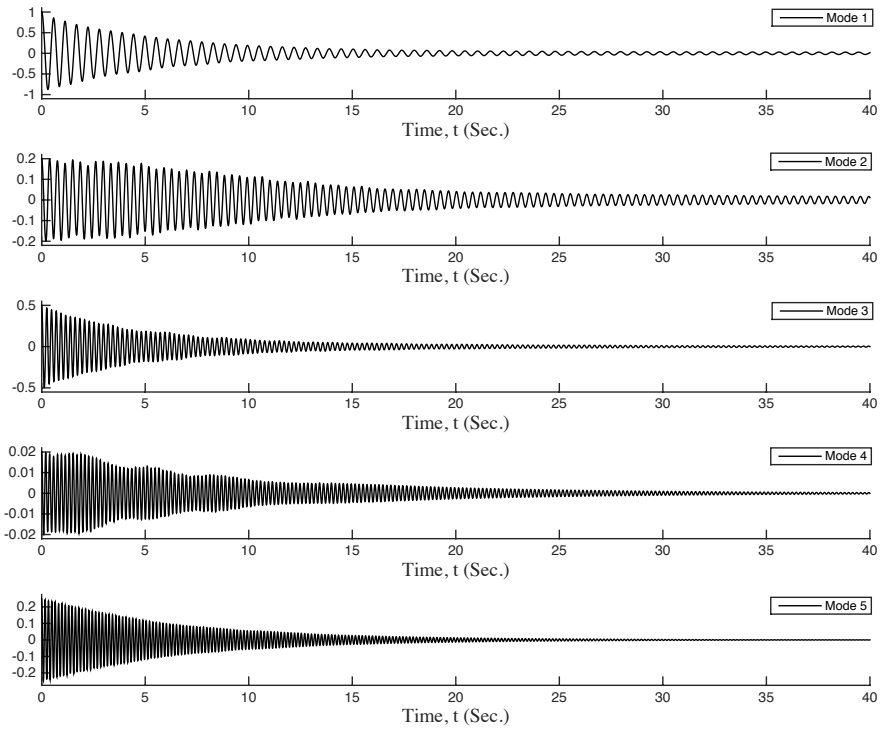

Figure 4.32. Modal displacements for plate with elastic boundary condition and $K_s = 100\ N/m$ using filtered and saturated in-plane controlled forces

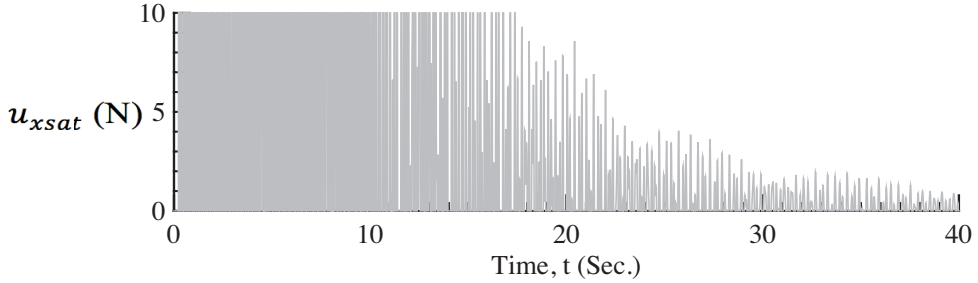

Figure 4.33. u_{xsat} inputs for a plate with elastic boundary condition and $K_s = 100\ N/m$

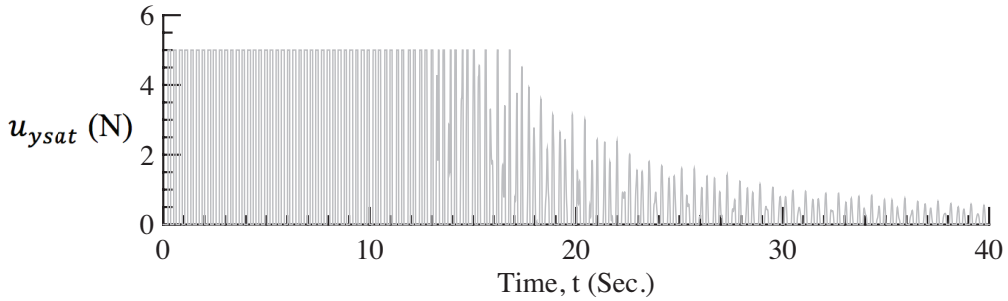

Figure 4.34. u_{ysat} inputs for a plate with elastic boundary condition and $K_s = 100\ N/m$

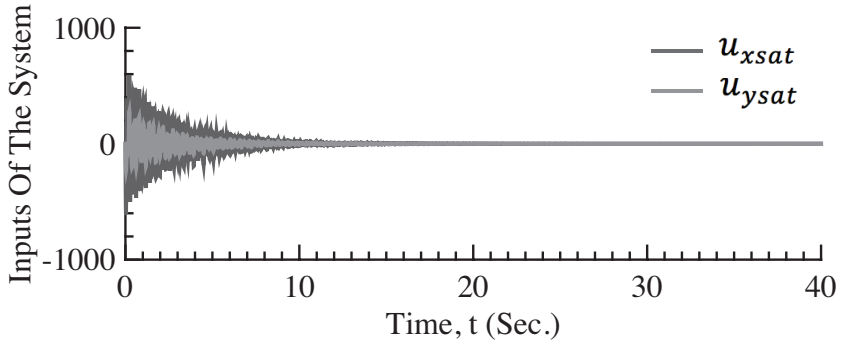

Figure 4.35. Filter input for a plate with elastic boundary condition and $K_s = 100\ N/m$ using modified control logic

To investigate the boundary condition effects on the control logic, we reduced the stiffness constant to $K_s = 10\ N/m$. The frequency analysis results for different combination of in-plane forces are listed in Table 4.7.

Table 4.7. Frequencies in Hz using Finite Element Analysis for elastic boundary condithins and $K_s = 10\ N/m$

Mode	Freq. in Hz for $N_x = 0$ and $N_y = 0$	Freq. in Hz for $N_x = 10N$ and $N_y = 0$	Freq. in Hz for $N_x = 0$ and $N_y = 5N$	Freq. in Hz for $N_x = 10N$ and $N_y = 5N$
1	1.4397	1.5664	1.6647	1.7764
2	2.2204	2.5273	2.3485	2.6427
3	3.4896	3.8983	3.5532	3.9574
4	4.9045	5.0257	5.0672	5.1862
5	5.1663	5.6107	5.1983	5.6414

Comparing Tables 4.6 and 4.7, we observe that the frequencies are reduced as we reduce the stiffness constant for the boundary springs. The control scheme results are shown in the Figs. 4.36 – 4.46 using $K = 10\ N/m$ with the initial condition in (4.21).

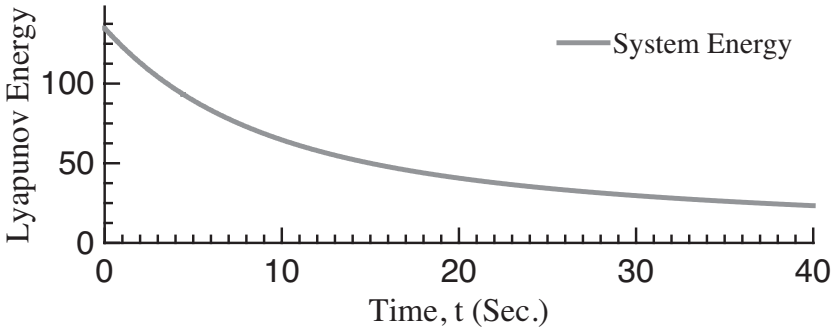

Figure 4.36. Energy deception for elastic boundary condition without in-plane forces and $K_s = 10 \ \ N/m$ using FEM approximation

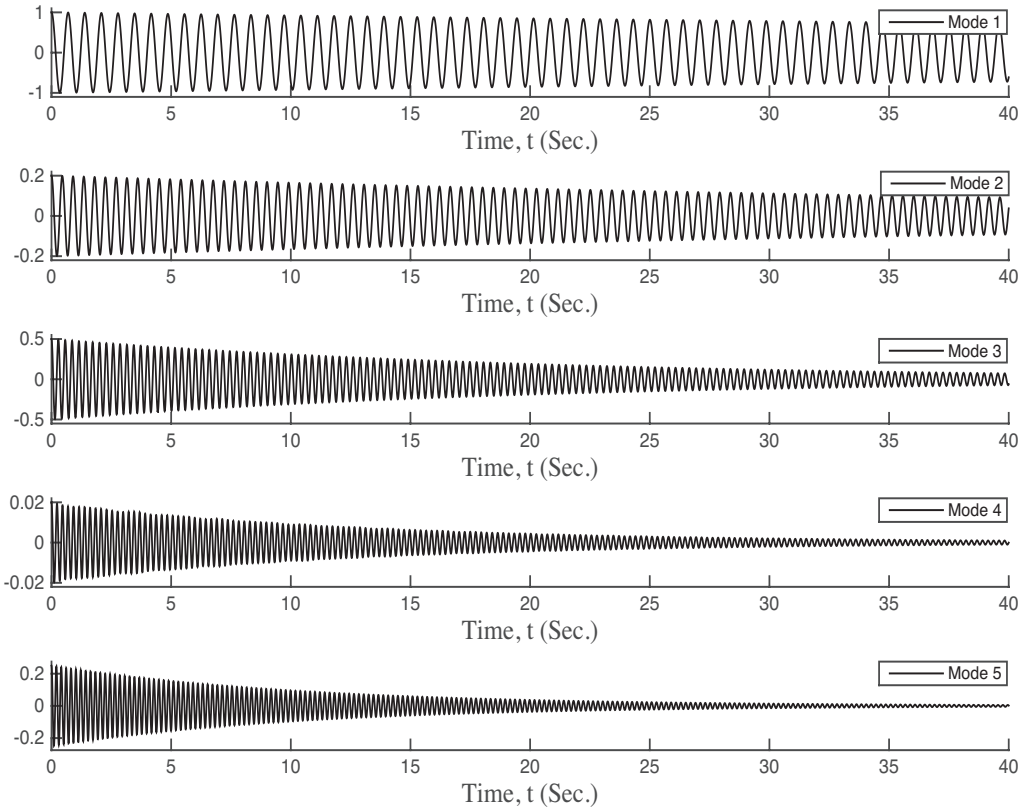

Figure 4.37. Modal displacements for elastic boundary condition without in-plane forces and $K_s = 10 \ \ N/m$ using FEM approximation

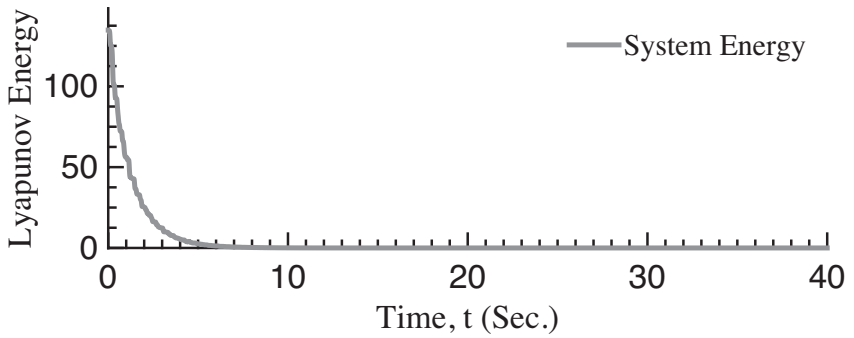

Figure 4.38. Energy deception for elastic boundary condition with $K_s = 10\ N/m$ using controlled in-plane forces

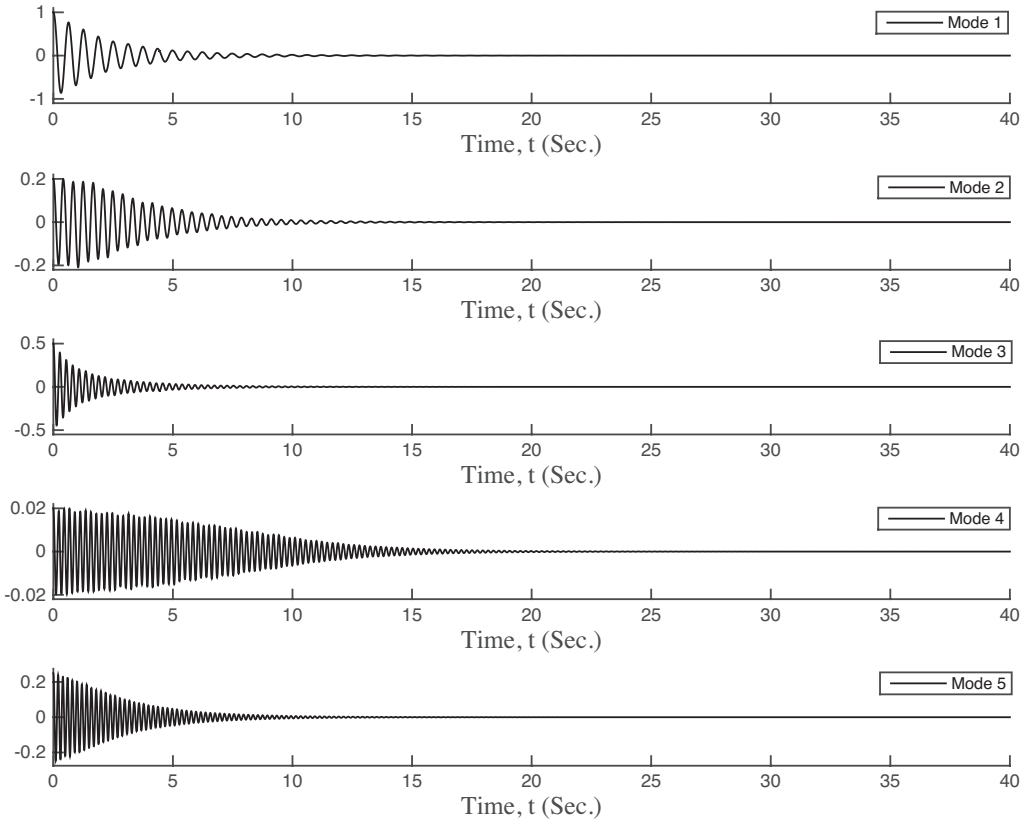

Figure 4.39. Modal displacements for elastic boundary condition with $K_s = 10\ N/m$ using controlled in-plane forces

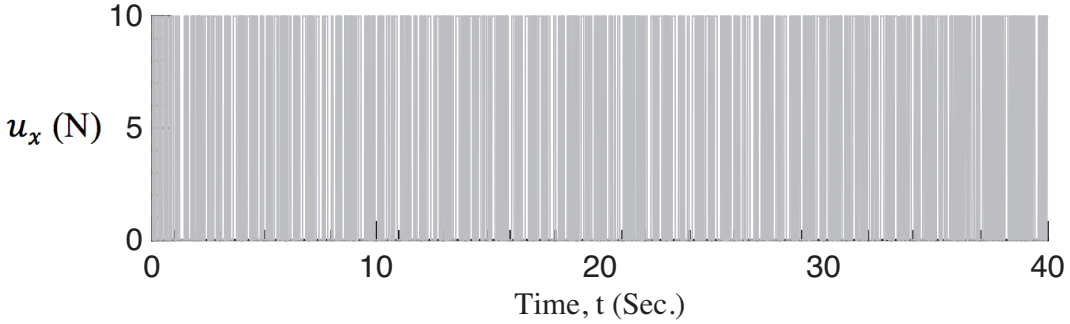

Figure 4.40. Controlled u_x forces for plate with elastic boundary condition and $K_s = 10\ N/m$

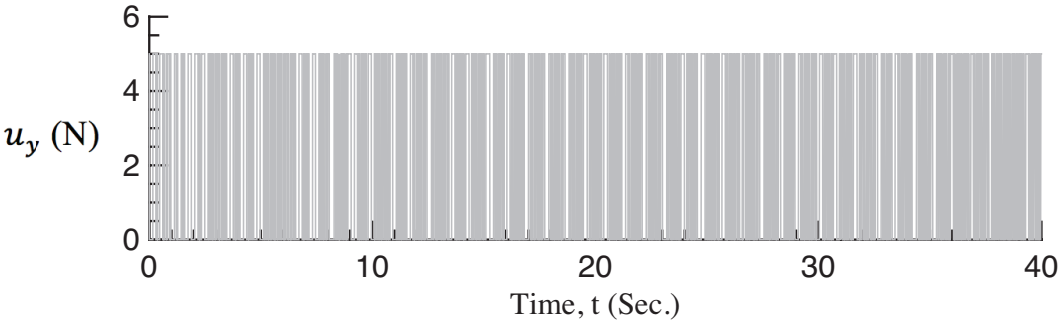

Figure 4.41. Controlled u_y forces for a plate with elastic boundary condition and $K_s = 10\ N/m$

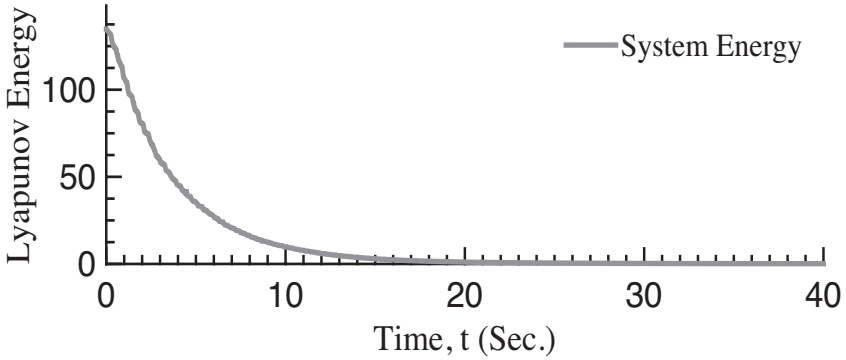

Figure 4.42. Energy deception for plate with elastic boundary condition and $K_s = 10\ N/m$ using modified control logic

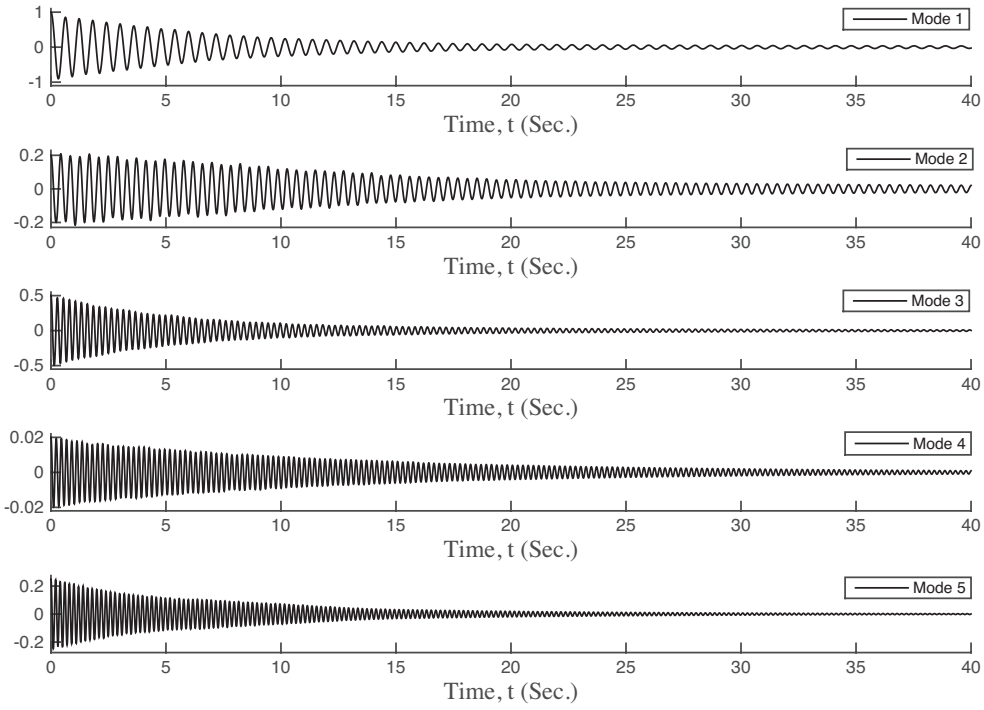

Figure 4.43. Modal displacements for elastic boundary condition and $K_s = 10\ N/m$ using modified control logic

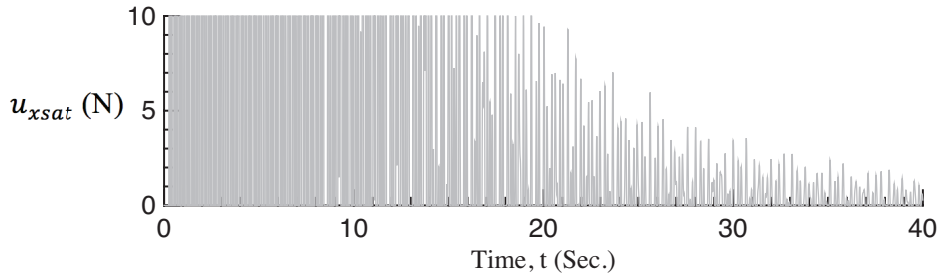

Figure 4.44. u_{xsat} inputs for a plate with elastic boundary condition and $K_s = 10\ N/m$ using modified control logic

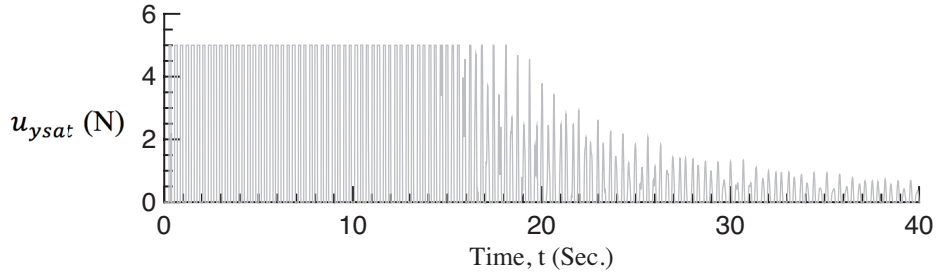

Figure 4.45. N_y inputs for a plate with elastic boundary condition and $K_s = 10\ N/m$ using modified control logic

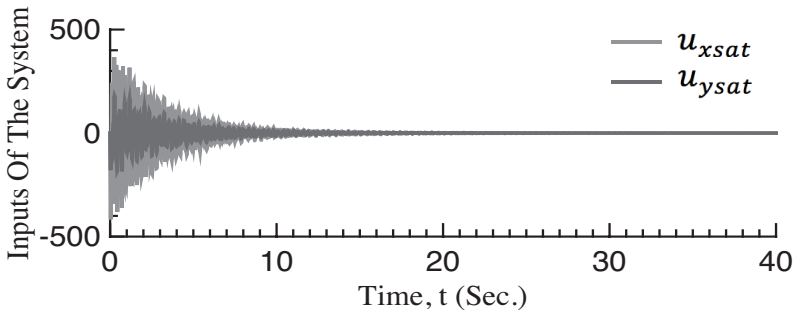

Figure 4.46. Filter inputs for a plate with elastic boundary condition and $K_s = 10\ N/m$ using modified control logic

Comparing the results we got for the plate with the elastic boundary condition (Figs. 4.27 – 4.35 for $K_s = 100\ N/m$ and Figs. 4.38 – 4.46 for $K_s = 10\ N/m$), we observe that the vibration takes longer time to converge to zero as we decrease the stiffness constant. The control logic in (4.7) takes approximately 6 seconds to eliminate the vibration for $K_s = 100\ N/m$ and 7 seconds for $K_s = 10\ N/m$. However, the modified control logic (4.12) using filter and saturation takes around 18 seconds to do that for $K_s = 100\ N/m$ and 20 seconds for $K_s = 10\ N/m$. In conclusion, using the elastic boundary conditions alters the stiffness matrix and reduces the efficacy of the control logic (section 4.1) that is based on increasing the stiffness of the system using controlled in-plane forces.

Remark:

Form the previous results we can claim that our control logic with and without the low-pass filter and the saturation (logics in (4.7) and (4.12)) does the designed purpose by controlling the vibration of the thin elastic plate using uniformly distributed in-plane forces. Adding the filter and saturation to the control logic effects the results by increasing the vibrating time from 5 to 15 seconds in the simply supported plate. However, they reduce the switching frequency of the in-plane forces and converge these forces to zero as the vibration subsidies. These results can be improved by assigning different values for the time constant τ and ϵ for the saturation. For instance, assigning smaller τ, higher bandwidth will speed the vibration suppression, but it will cause more frequent switching in the in-plane forces. This tradeoff process should be considered in real application when we choose the actuator for our control logic.

Chapter 5

Vibration Control Of A Thin Rectangular Plate Using A Web-Of-Cables

In chapter four, a control strategy was introduced to control the vibration in a plate using uniformly distributed in-plane forces. Two different types of boundary conditions were considered and the control efficacy was proven through simulation. In this chapter, a web-of-cables around the plate is proposed as a mechanism to suppress the vibration of the plate. The web-of-cables structure provides the boundary of the plate with in-plane forces that act at a few discrete locations, which results in a non-uniform stress distribution. A model of the pre-stressed plate is first developed in this chapter. The dynamic model of the plate is then obtained from vibration analysis using the pre-stress data. Finally, the control logic introduced in section 4.1 (which is an extension of the work presented by Nudehi [48]) is applied to suppress the vibration.

5.1 A Web-Of-Cables Structure Supporting A Plate

In this section, a web-of-cables structure is proposed for supporting a plate and the forces in the cables are investigated. The web structure, which is shown in Fig. 5.1, is comprised of the following:

- Corner cables, which their lengths are labeled as L_{01} and L_{02}.
- Side cables that have a catenary shape and their lengths are labeled as L_1, L_2, L_3, K_1 and K_2.
- Boundary cables that connects the web structure to the plate edges; their lengths are labeled as l_1, l_2, l_3, h_1, and h_2.

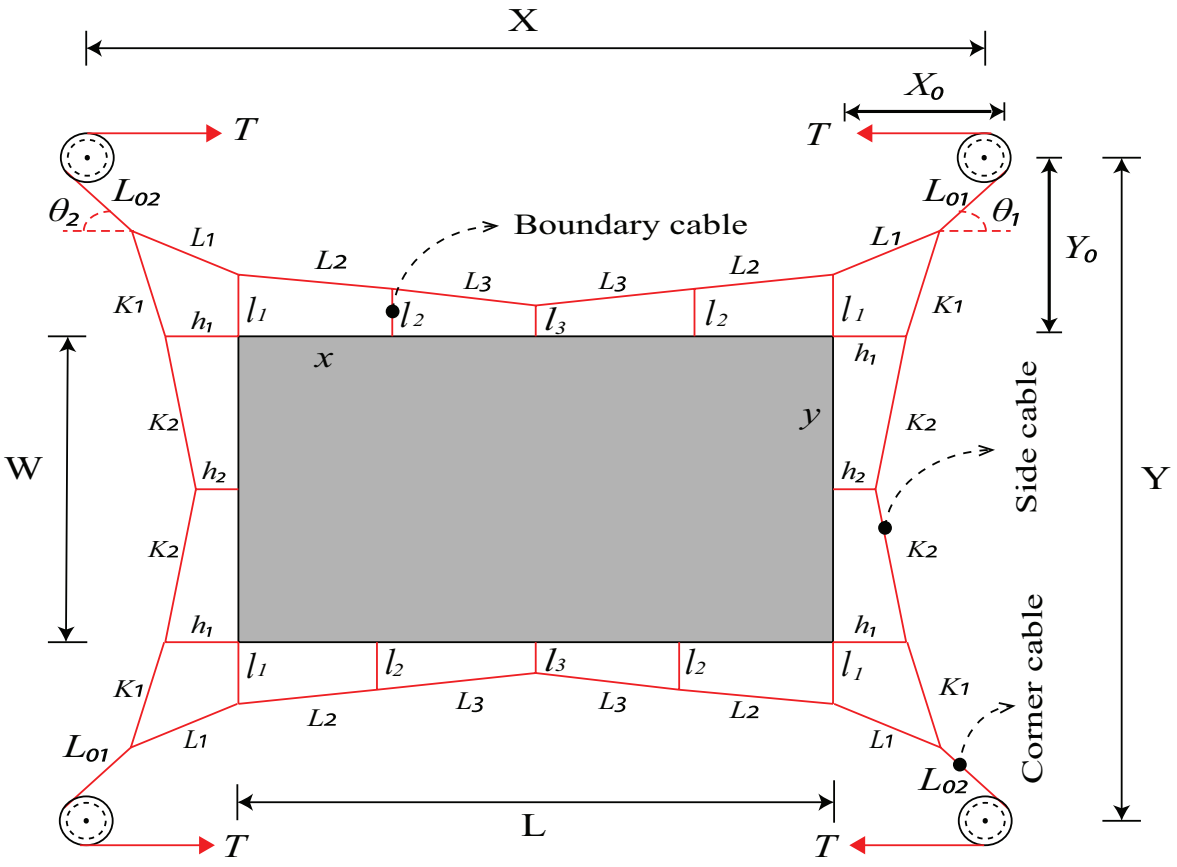

Figure 5.1. Rectangular plate with a web-of-cables structure

We first study the static characteristics of the web structure. The tensions in the boundary cables are considered to be equal to T_0 and perpendicular to the plate edges. Also, the tensions in the corner cables T are equal and they have the same angle θ with respect the x-axis, which can be obtained from

$$\theta = tan^{-1}\left(\frac{W}{L}\right) \tag{5.1}$$

where W and L are the width and the length of the plate. Equation (5.1) follows from the assumption that the corner cables are congruent with the diagonal of the plat. To simplify the problem, it is considered that the web-of-cables configuration is symmetric in both x and y directions. Assuming symmetry, it is sufficient to investigate the top-right quarter of the plate that has three cables on the top edge and two cables on its right edge as shown in Fig. 5.2.

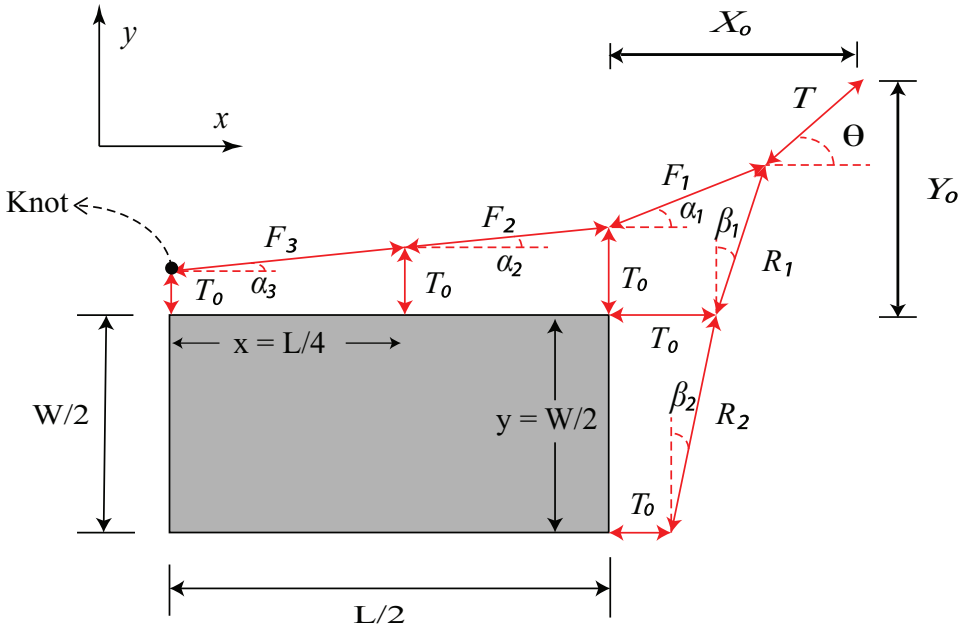

Figure 5.2. Quarter of a plate with web-of-cables structure

In Figure 5.2, X_0 and Y_0 are the distances from the corner of the plate to the pulley in the *x* and *y* directions respectively. The tensions in the side cables are assumed to be all positive and denoted by F_1, F_2, F_3, R_1, and R_2. Also, the cables are assumed to be inextensible. The plate is considered to be rigid; hence, the web-of-cables structure can have deformation. By considering the static equilibrium at each knot (point where two or more cables meet), we get 11 equations from the 6 knots – see Fig. 5.2. However, in this web structure there are 13 unknowns that are labeled as $T, F_1, F_2, F_3, R_1, R_2, l_1, l_2, l_3, h_1, h_2, X_0$ and Y_0. To simplify the problem, we assume two arbitrary variables to match the number of the equations with the number of unknowns. We assume l_3 and X_0 to be known. We observe that by changing either l_3 or X_0 the configuration of the web structure is changed as well, which means that the problem has infinite number of solutions for different values of l_3 or X_0. To solve for the unknowns, we write the equation for static equilibrium at the six knots first:

$$T\cos\theta = F_1\cos\left(\tan^{-1}\left(\frac{Y_0 - l_1}{X_0}\right)\right) + R_1\sin\left(\tan^{-1}\left(\frac{X_0 - h_1}{Y_0}\right)\right) \tag{5.2}$$

$$T\sin\theta = F_1\sin\left(\tan^{-1}\left(\frac{Y_0 - l_1}{X_0}\right)\right) + R_1\cos\left(\tan^{-1}\left(\frac{X_0 - h_1}{Y_0}\right)\right) \tag{5.3}$$

$$F_1\cos\left(\tan^{-1}\left(\frac{Y_0 - l_1}{X_0}\right)\right) = F_2\cos\left(\tan^{-1}\left(\frac{l_1 - l_2}{x}\right)\right) \tag{5.4}$$

$$F_1\sin\left(\tan^{-1}\left(\frac{Y_0 - l_1}{X_0}\right)\right) = F_2\sin\left(\tan^{-1}\left(\frac{l_1 - l_2}{x}\right)\right) + T_0 \tag{5.5}$$

$$F_2\cos\left(\tan^{-1}\left(\frac{l_1 - l_2}{x}\right)\right) = F_3\cos\left(\tan^{-1}\left(\frac{l_2 - l_3}{x}\right)\right) \tag{5.6}$$

$$F_2\sin\left(\tan^{-1}\left(\frac{l_1 - l_2}{x}\right)\right) = F_3\sin\left(\tan^{-1}\left(\frac{l_2 - l_3}{x}\right)\right) + T_0 \tag{5.7}$$

$$2\times F_3\sin\left(\tan^{-1}\left(\frac{l_2 - l_3}{x}\right)\right) = T_0 \tag{5.8}$$

$$R_1 \cos\left(\tan^{-1}\left(\frac{X_0 - h_1}{Y_0}\right)\right) = R_2 \cos\left(\tan^{-1}\left(\frac{h_1 - h_2}{y}\right)\right) \tag{5.9}$$

$$R_1 \sin\left(\tan^{-1}\left(\frac{X_0 - h_1}{Y_0}\right)\right) = R_2 \sin\left(\tan^{-1}\left(\frac{h_1 - h_2}{y}\right)\right) + T_0 \tag{5.10}$$

$$2{\times}R_2 \sin\left(\tan^{-1}\left(\frac{h_1 - h_2}{y}\right)\right) = T_0 \tag{5.11}$$

In addition, we have from the geometry

$$\theta = \tan^{-1}\left(\frac{Y_0}{X_0}\right) \tag{5.12}$$

where θ is known - see Equation (5.1). In (5.2) – (5.12), we have eleven unknowns since l_3 and X_0 are considered to be known. These equations are solved for the parameters listed in Table 5.1; the results are shown in Table 5.2, and 5.3.

Table 5.1. Preset parameters for the design problem

T_0(N)	1
θ (deg.)	26.5651
l_3(m)	0.2
X_0(m)	1
L (m)	2
W (m)	1

Table 5.2. Cables tension results for the design problem

T (N)	14.7208
F_1(N)	11.9315
F_2(N)	11.7627
F_3(N)	11.6774
R_1(N)	4.3501
R_2(N)	4.1138

Table 5.3. Cables length results for the design problem

l_1(m)	0.2857
l_2(m)	0.2214
h_1(m)	0.8163
h_2(m)	0.7551
Y_0(m)	0.5

From the results in Tables 5.2, and 5.3, the remaining unknowns of the web-of-cables structure are solved using the following kinematic relationships and presented in Table 5.4:

$$\alpha_1 = \tan^{-1}\left(\frac{Y_0 - l_1}{X_0}\right) \tag{5.13}$$

$$\alpha_2 = \tan^{-1}\left(\frac{l_1 - l_2}{x}\right) \tag{5.14}$$

$$\alpha_3 = \tan^{-1}\left(\frac{l_2 - l_3}{x}\right) \tag{5.15}$$

$$\beta_1 = \tan^{-1}\left(\frac{X_0 - h_1}{Y_0}\right) \tag{5.16}$$

$$\beta_2 = \tan^{-1}\left(\frac{h_1 - h_2}{y}\right) \tag{5.17}$$

$$L_2 = \frac{x}{\cos\alpha_2} = \frac{L}{4\cos\alpha_2} \tag{5.18}$$

$$L_3 = \frac{x}{\cos\alpha_3} = \frac{L}{4\cos\alpha_3} \tag{5.19}$$

$$K_2 = \frac{y}{\cos\beta_2} = \frac{W}{2\cos\beta_2} \tag{5.20}$$

$$L_1\cos\alpha_1 = h_1 + K_1\sin\beta_1 \tag{5.21}$$

$$L_1\sin\alpha_1 + l_1 = K_1\cos\beta_1 \tag{5.22}$$

Table 5.4. Cables angles and length results for the design problem

α_1(deg.)	12.0948
α_2(deg.)	7.3264
α_3(deg.)	2.454
β_1(deg.)	20.1707
β_2(deg.)	6.9811
L_1(m)	1.0227
L_2(m)	0.5041
L_3(m)	0.5005
K_1(m)	0.5327
K_2(m)	0.5037

5.2 Investigating The Changes in The Corner Cables Tensions

In the previous section, the web-of-cables structure was investigated with constant corner tension. In this section, we investigate the effect of changing the corner cables tensions from their nominal values. Specifically, we increase the tension of two opposite corners by ΔT and decrease the tension of the other two corners by ΔT. As a result of these changes, the web-of-cables structure is deformed and the plate undergoes rotation – see Fig. 5.3. Due to the way that ΔT is applied, symmetry about the center of the plate is maintained. In addition, all the side and boundary cables length are considered to remain unchanged from their values in the undeformed configuration. In the new configuration, the side cables will no longer be perpendicular to the edge of the plate. The fixed coordinates of the pulleys are used to determine the angles of the corner cables after the deformation. By analyzing the new web configuration, we obtain 81 equations that include 81 unknowns. These equations are obtained from both kinematics and kinetic equilibrium equations for the structure. To eliminate the moment that is caused by changing the tensions at the corners, we allowed the plate to translate and freely rotate about its origin. In this setup the web cable lengths and the corner tensions T are known from the design configuration - see Tables 5.2 – 5.4. We considered adding $\Delta T = 3N$ to two corner tensions and subtracting it from the others two corner tensions as shown in Fig. 5.4.

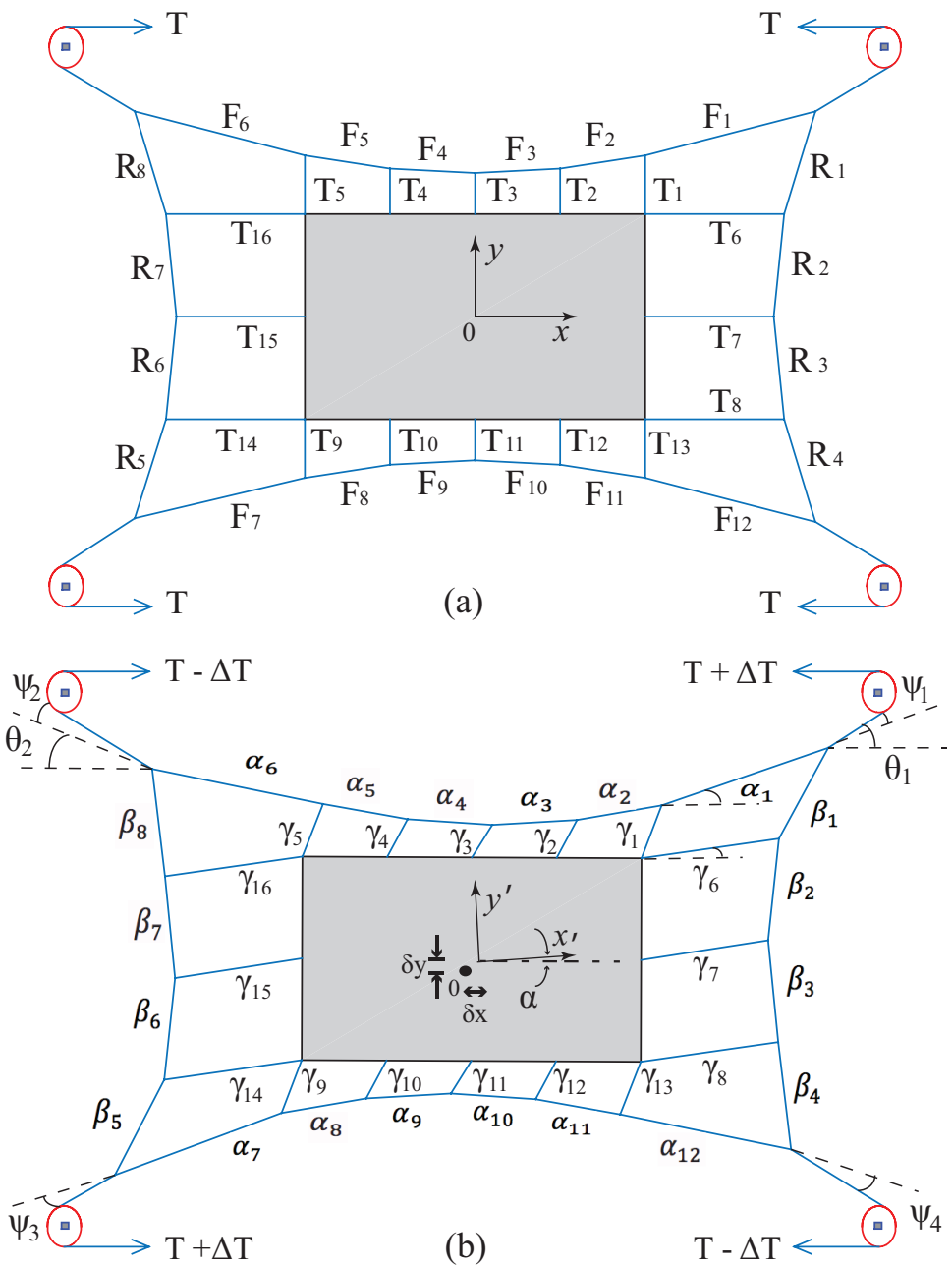

Figure 5.3. Plate with the with-of-cables before the deformation, (b), after deformation – the forces in the web-of-cables structure are shown in (a), and the angles of deformations are shown in (b)

To investigate the rotational and translational displacements in the plate, a full plate model is used. The 81 unknown variables of the model are comprised of the following:

- The unknown forces, which are labeled as F_i, where i = 1, 2,.., 12; R_j, where j = 1, 2,.., 8; and T_n, where n = 1, 2,.., 16.
- The unknown angles of deformation, which are labeled as α_i, where i = 1, 2,.., 12; β_j, where j = 1, 2,.., 8; γ_n, where n = 1, 2,.., 16; ψ_s, where s = 1, 2,.., 4; and α.
- The unknown corner cables length, which are labeled as L_{0r}, where r = 1, 2,..,4.

The corner cables static equilibrium equations are:

$$(T + \Delta T)\cos(\theta_1 - \alpha) = F_1 \cos\alpha_1 + R_1 \sin\beta_1 \tag{5.23}$$

$$(T + \Delta T)\sin(\theta_1 - \alpha) = F_1 \sin\alpha_1 + R_1 \cos\beta_1 \tag{5.24}$$

$$(T - \Delta T)\cos(\theta_2 + \alpha) = F_6 \cos\alpha_6 + R_8 \sin\beta_8 \tag{5.25}$$

$$(T - \Delta T)\sin(\theta_2 + \alpha) = F_6 \sin\alpha_6 + R_8 \cos\beta_8 \tag{5.26}$$

$$(T + \Delta T)\cos(\theta_3 - \alpha) = F_7 \cos\alpha_7 + R_5 \sin\beta_5 \tag{5.27}$$

$$(T + \Delta T)\sin(\theta_3 - \alpha) = F_7 \sin\alpha_7 + R_5 \cos\beta_5 \tag{5.28}$$

$$(T - \Delta T)\cos(\theta_4 + \alpha) = F_{12} \cos\alpha_{12} + R_4 \sin\beta_4 \tag{5.29}$$

$$(T - \Delta T)\sin(\theta_4 + \alpha) = F_{12} \sin\alpha_{12} + R_4 \cos\beta_4 \tag{5.30}$$

The static equilibrium of the top edge knots gives:

$$F_1 \cos\alpha_1 = F_2 \cos\alpha_2 + T_1 \sin\gamma_1 \tag{5.31}$$

$$F_1 \sin\alpha_1 = F_2 \sin\alpha_2 + T_1 \cos\gamma_1 \tag{5.32}$$

$$F_2 \cos \alpha_2 = F_3 \cos \alpha_3 + T_2 \sin \gamma_2 \quad (5.33)$$

$$F_2 \sin \alpha_2 = F_3 \sin \alpha_3 + T_2 \cos \gamma_2 \quad (5.34)$$

$$F_3 \cos \alpha_3 = F_4 \cos \alpha_4 + T_3 \sin \gamma_3 \quad (5.35)$$

$$F_3 \sin \alpha_3 + F_4 \sin \alpha_4 = T_3 \cos \gamma_3 \quad (5.36)$$

$$F_4 \cos \alpha_4 = F_5 \cos \alpha_5 + T_4 \sin \gamma_4 \quad (5.37)$$

$$F_5 \sin \alpha_5 = F_4 \sin \alpha_4 + T_4 \cos \gamma_4 \quad (5.38)$$

$$F_5 \cos \alpha_5 = F_6 \cos \alpha_6 + T_5 \sin \gamma_5 \quad (5.39)$$

$$F_6 \sin \alpha_6 = F_5 \sin \alpha_5 + T_5 \cos \gamma_5 \quad (5.40)$$

For the bottom edge knots, the static equilibrium equations can be expressed as

$$F_7 \cos \alpha_7 = F_8 \cos \alpha_8 + T_9 \sin \gamma_9 \quad (5.41)$$

$$F_7 \sin \alpha_7 = F_8 \sin \alpha_8 + T_9 \cos \gamma_9 \quad (5.42)$$

$$F_8 \cos \alpha_8 = F_9 \cos \alpha_9 + T_{10} \sin \gamma_{10} \quad (5.43)$$

$$F_8 \sin \alpha_8 = F_9 \sin \alpha_9 + T_{10} \cos \gamma_{10} \quad (5.44)$$

$$F_9 \cos \alpha_9 = F_{10} \cos \alpha_{10} + T_{11} \sin \gamma_{11} \quad (5.45)$$

$$F_9 \sin \alpha_9 + F_{10} \sin \alpha_{10} = T_{11} \cos \gamma_{11} \quad (5.46)$$

$$F_{10} \cos \alpha_{10} = F_{11} \cos \alpha_{11} + T_{12} \sin \gamma_{12} \quad (5.47)$$

$$F_{11} \sin \alpha_{11} = F_{10} \sin \alpha_{10} + T_{12} \cos \gamma_{12} \quad (5.48)$$

$$F_{11} \cos \alpha_{11} = F_{12} \cos \alpha_{12} + T_{13} \sin \gamma_{13} \quad (5.49)$$

$$F_{12} \sin \alpha_{12} = F_{11} \sin \alpha_{11} + T_{13} \cos \gamma_{13} \quad (5.50)$$

The static equilibrium for left edge knots yield

$$R_1 \cos \beta_1 = R_2 \cos \beta_2 + T_6 \sin \gamma_6 \quad (5.51)$$

$$R_1 \sin \beta_1 = R_2 \sin \beta_2 + T_6 \cos \gamma_6 \quad (5.52)$$

$$R_2 \cos \beta_2 = R_3 \cos \beta_3 + T_7 \sin \gamma_7 \quad (5.53)$$

$$R_2 \sin \beta_2 + R_3 \sin \beta_3 = T_7 \cos \gamma_7 \quad (5.54)$$

$$R_3 \cos \beta_3 = R_4 \cos \beta_4 + T_8 \sin \gamma_8 \quad (5.55)$$

$$R_4 \sin \beta_4 = R_3 \sin \beta_3 + T_8 \cos \gamma_8 \quad (5.56)$$

For the right edge knots, the static equilibrium equations are

$$R_5 \cos \beta_5 = R_6 \cos \beta_6 + T_{14} \sin \gamma_{14} \quad (5.57)$$

$$R_5 \sin \beta_5 = R_6 \sin \beta_6 + T_{14} \cos \gamma_{14} \quad (5.58)$$

$$R_6 \cos \beta_6 = R_7 \cos \beta_7 + T_{15} \sin \gamma_{15} \quad (5.59)$$

$$R_6 \sin \beta_6 + R_7 \sin \beta_7 = T_{15} \cos \gamma_{15} \quad (5.60)$$

$$R_7 \cos \beta_7 = R_8 \cos \beta_8 + T_{16} \sin \gamma_{16} \quad (5.61)$$

$$R_8 \sin \beta_8 = R_7 \sin \beta_7 + T_{16} \cos \gamma_{16} \quad (5.62)$$

The geometry of the structure for the top edge gives

$$l_2 \sin \gamma_2 + L_2 \cos \alpha_2 = l_1 \sin \gamma_1 + x \quad (5.63)$$

$$l_2 \cos \gamma_2 + L_2 \sin \alpha_2 = l_1 \cos \gamma_1 \quad (5.64)$$

$$l_3 \sin\gamma_3 + L_3 \cos\alpha_3 = l_2 \sin\gamma_2 + x \tag{5.65}$$

$$l_3 \cos\gamma_3 + L_3 \sin\alpha_3 = l_2 \cos\gamma_2 \tag{5.66}$$

$$l_2 \sin\gamma_4 + L_3 \cos\alpha_4 = l_3 \sin\gamma_3 + x \tag{5.67}$$

$$l_3 \cos\gamma_3 + L_3 \sin\alpha_4 = l_2 \cos\gamma_4 \tag{5.68}$$

$$l_1 \sin\gamma_5 + L_2 \cos\alpha_5 = l_2 \sin\gamma_4 + x \tag{5.69}$$

$$l_2 \cos\gamma_4 + L_2 \sin\alpha_5 = l_1 \cos\gamma_5 \tag{5.70}$$

For the bottom edge, the geometry of the structure gives

$$l_2 \sin\gamma_{10} + L_2 \cos\alpha_8 = l_1 \sin\gamma_9 + x \tag{5.71}$$

$$l_2 \cos\gamma_{10} + L_2 \sin\alpha_8 = l_1 \cos\gamma_9 \tag{5.72}$$

$$l_3 \sin\gamma_{11} + L_3 \cos\alpha_9 = l_2 \sin\gamma_{10} + x \tag{5.73}$$

$$l_3 \cos\gamma_{11} + L_3 \sin\alpha_9 = l_2 \cos\gamma_{10} \tag{5.74}$$

$$l_2 \sin\gamma_{12} + L_3 \cos\alpha_{10} = l_3 \sin\gamma_{11} + x \tag{5.75}$$

$$l_3 \cos\gamma_{11} + L_3 \sin\alpha_{10} = l_2 \cos\gamma_{12} \tag{5.76}$$

$$l_1 \sin\gamma_{13} + L_2 \cos\alpha_{11} = l_2 \sin\gamma_{12} + x \tag{5.77}$$

$$l_2 \cos\gamma_{12} + L_2 \sin\alpha_{11} = l_1 \cos\gamma_{13} \tag{5.78}$$

For the right edge of the plate, the geometry of the web structure can be expressed as

$$h_2 \sin\gamma_7 + K_2 \cos\beta_2 = y + h_1 \sin\gamma_6 \tag{5.79}$$

$$h_2 \cos\gamma_7 + K_2 \sin\beta_2 = h_1 \cos\gamma_6 \tag{5.80}$$

$$h_1 \sin\gamma_8 + K_2 \cos\beta_3 = y + h_2 \sin\gamma_7 \tag{5.81}$$

$$h_2 \cos\gamma_7 + K_2 \sin\beta_3 = h_1 \cos\gamma_8 \tag{5.82}$$

For the left edge of the plate, the equations are

$$h_2 \sin\gamma_{15} + K_2 \cos\beta_6 = y + h_1 \sin\gamma_{14} \tag{5.83}$$

$$h_2 \cos\gamma_{15} + K_2 \sin\beta_6 = h_1 \cos\gamma_{14} \tag{5.84}$$

$$h_1 \sin\gamma_{16} + K_2 \cos\beta_7 = y + h_2 \sin\gamma_{15} \tag{5.85}$$

$$h_2 \cos\gamma_{15} + K_2 \sin\beta_7 = h_1 \cos\gamma_{16} \tag{5.86}$$

Finally, for the corner cells, the kinematic relationships are

$$l_1 \sin\gamma_1 + L_1 \cos\alpha_1 = h_1 \cos\gamma_6 + K_1 \sin\beta_1 \tag{5.87}$$

$$l_1 \cos\gamma_1 + L_1 \sin\alpha_1 = h_1 \sin\gamma_6 + K_1 \cos\beta_1 \tag{5.88}$$

$$l_1 \cos\gamma_5 + L_1 \sin\alpha_6 = K_1 \cos\beta_8 - h_1 \sin\gamma_{16} \tag{5.89}$$

$$L_1 \cos\alpha_6 - l_1 \sin\gamma_5 = h_1 \cos\gamma_{16} + K_1 \sin\beta_8 \tag{5.90}$$

$$l_1 \sin\gamma_9 + L_1 \cos\alpha_7 = h_1 \cos\gamma_{14} + K_1 \sin\beta_5 \tag{5.91}$$

$$l_1 \cos\gamma_9 + L_1 \sin\alpha_7 = h_1 \sin\gamma_{14} + K_1 \cos\beta_5 \tag{5.92}$$

$$l_1 \cos\gamma_{13} + L_1 \sin\alpha_{12} = K_1 \cos\beta_4 - h_1 \sin\gamma_8 \tag{5.93}$$

$$L_1 \cos\alpha_{12} - l_1 \sin\gamma_{13} = h_1 \cos\gamma_8 + K_1 \sin\beta_4 \tag{5.94}$$

Equations (5.23) to (5.94) provide a total of 72 equations. The remaining 9 equations require us to define the coordinate transformation (see Fig. 5.4) associated with the rotation of the plate.

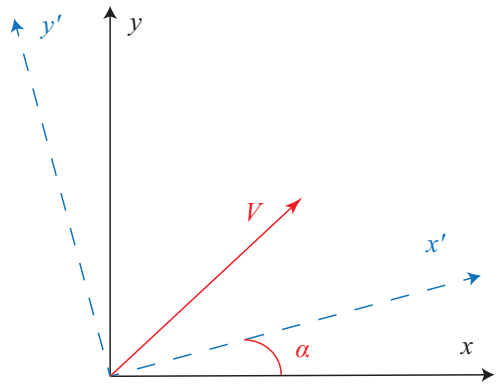

Figure 5.4. Coordinate Transformation

The rotated coordinates $\acute{x}$ and $\acute{y}$ are related to the original coordinates as follows:

$$\begin{aligned} \acute{x}_i &= x_i \cos\alpha + y_i \sin\alpha \\ \acute{y}_i &= x_i \sin\alpha - y_i \cos\alpha \quad , \text{where } i = 1,2,3,4 \end{aligned} \tag{5.95}$$

Then

$$\begin{aligned} r_i &= \sqrt{\acute{x}_i{}^2 + \acute{y}_i{}^2} \\ \psi_i &= \tan^{-1}\left(\frac{\acute{y}_i}{\acute{x}_i}\right) \quad , \text{where } i = 1,2,3,4 \end{aligned} \tag{5.96}$$

In (5.95) and (5.96), x_i and y_i are the distances evaluated from the center of the plate to the corner cables. For instance, x_1 and y_1 for the upper-right corner can be obtained from

$$\begin{aligned} x_1 = \frac{L}{2}\cos\alpha &+ (h_2 \cos\gamma_7 + K_2 \sin\beta_2 + K_1 \sin\beta_1)\cos\alpha \\ &+ (h_2 \sin\gamma_7 + K_2 \cos\beta_2 + K_1 \cos\beta_1)\sin\alpha \end{aligned} \tag{5.97}$$

$$\begin{aligned} y_1 = (h_2 \cos\gamma_7 + K_2 \sin\beta_2 + K_1 \sin\beta_1)\ \sin\alpha \\ + (h_2 \sin\gamma_7 + K_2 \cos\beta_2 + K_1 \cos\beta_1)\cos\alpha \end{aligned} \tag{5.98}$$

Similarly, the other three x_i and y_i distances can be obtained. Using the coordinate transformations formula in (5.95), the distance between the four fixed corner pulleys can be written as

$$
\begin{aligned}
X = L\cos\alpha &+ [h_2\cos\gamma_7 + K_2\sin\beta_2 + K_1\sin\beta_1]\cos\alpha \\
&+ [h_2\sin\gamma_7 + K_2\cos\beta_2 + K_1\cos\beta_1]\sin\alpha \\
&+ L_{01}\cos(\theta_1 - \psi_1) \\
&+ [h_2\cos\gamma_{15} + K_2\sin\beta_7 + K_1\sin\beta_8]\cos\alpha \\
&+ [-h_2\sin\gamma_{15} + K_2\cos\beta_7 + K_1\cos\beta_8]\sin\alpha \\
&+ L_{02}\cos(\theta_2 + \psi_2)
\end{aligned}
\tag{5.99}
$$

$$
\begin{aligned}
X = L\cos\alpha &+ [h_2\cos\gamma_{15} + K_2\sin\beta_6 + K_1\sin\beta_5]\cos\alpha \\
&+ [h_2\sin\gamma_{15} + K_2\cos\beta_6 + K_1\cos\beta_5]\sin\alpha \\
&+ L_{03}\cos(\theta_3 - \psi_3) \\
&+ [h_2\cos\gamma_7 + K_2\sin\beta_3 + K_1\sin\beta_4]\cos\alpha \\
&+ [-h_2\sin\gamma_7 + K_2\cos\beta_3 + K_1\cos\beta_4]\sin\alpha \\
&+ L_{04}\cos(\theta_4 + \psi_4)
\end{aligned}
\tag{5.100}
$$

$$
\begin{aligned}
Y = -[h_2\cos\gamma_7 &+ K_2\sin\beta_2 + K_1\sin\beta_1]\sin\alpha \\
&+ [h_2\sin\gamma_7 + K_2\cos\beta_2 + K_1\cos\beta_1]\cos\alpha \\
&+ L_{01}\sin(\theta_1 - \psi_1) \\
&- [h_2\cos\gamma_7 + K_2\sin\beta_3 + K_1\sin\beta_4]\sin\alpha \\
&+ [-h_2\sin\gamma_7 + K_2\cos\beta_3 + K_1\cos\beta_4]\cos\alpha \\
&+ L_{04}\sin(\theta_4 + \psi_4)
\end{aligned}
\tag{5.101}
$$

$$
\begin{aligned}
Y = -[h_2\cos\gamma_{15} &+ K_2\sin\beta_7 + K_1\sin\beta_8]\sin\alpha \\
&+ [-h_2\sin\gamma_{15} + K_2\cos\beta_7 + K_1\cos\beta_8]\cos\alpha \\
&+ L_{02}\sin(\theta_2 + \psi_2) \\
&- [h_2\cos\gamma_{15} + K_2\sin\beta_6 + K_1\sin\beta_5]\sin\alpha \\
&+ [h_2\sin\gamma_{15} + K_2\cos\beta_6 + K_1\cos\beta_5]\cos\alpha \\
&+ L_{03}\sin(\theta_3 - \psi_3)
\end{aligned}
\tag{5.102}
$$

$$
\begin{aligned}
&-[l_3 \sin\gamma_3 + L_3 \cos\alpha_3 + L_2 \cos\alpha_2 + L_1 \cos\alpha_1] \sin\alpha \\
&\quad + [l_3 \cos\gamma_3 + L_3 \sin\alpha_3 + L_2 \sin\alpha_2 + L_1 \sin\alpha_1] \cos\alpha \\
&\quad + L_{01} \sin(\theta_1 - \psi_1) \\
&\quad - [-l_3 \sin\gamma_3 + L_3 \cos\alpha_4 + L_2 \cos\alpha_5 + L_1 \cos\alpha_6] \sin\alpha \\
&\quad + [l_3 \cos\gamma_3 + L_3 \sin\alpha_4 + L_2 \sin\alpha_5 + L_1 \sin\alpha_6] \cos\alpha \\
&\quad + L_{02} \sin(\theta_2 + \psi_2) = 0
\end{aligned} \tag{5.103}
$$

$$
\begin{aligned}
&[l_3 \sin\gamma_3 + L_3 \cos\alpha_3 + L_2 \cos\alpha_2 + L_1 \cos\alpha_1] \cos\alpha \\
&\quad + [l_3 \cos\gamma_3 + L_3 \sin\alpha_3 + L_2 \sin\alpha_2 + L_1 \sin\alpha_1] \sin\alpha \\
&\quad + L_{01} \cos(\theta_1 - \psi_1) \\
&\quad - [-l_3 \sin\gamma_{11} + L_3 \cos\alpha_{10} + L_2 \cos\alpha_{11} \\
&\quad + L_1 \cos\alpha_{12}] \cos\alpha \\
&\quad - [l_3 \cos\gamma_{11} + L_3 \sin\alpha_{10} + L_2 \sin\alpha_{11} + L_1 \sin\alpha_{12}] \sin\alpha \\
&\quad - L_{04} \cos(\theta_4 + \psi_4) = 0
\end{aligned} \tag{5.104}
$$

Balance of moment about the center of mass of the plate gives

$$
\begin{aligned}
&(T + \Delta T)\ r_1\ \sin(\theta_1 - \psi_1) - (T + \Delta T)\, r_2 \sin(\theta_2 + \psi_2) \\
&\quad + (T + \Delta T)\, r_3 \sin(\theta_3 - \psi_3) \\
&\quad - (T + \Delta T)\ r_4 \sin(\theta_4 + \psi_4) = 0
\end{aligned} \tag{5.105}
$$

$$
\begin{aligned}
&(T + \Delta T) \cos(\theta_1 - \psi_1) + (T + \Delta T) \cos(\theta_4 + \psi_4) \\
&\quad - (T - \Delta T) \cos(\theta_3 - \psi_3) \\
&\quad - (T + \Delta T) \cos(\theta_2 + \psi_2) = 0
\end{aligned} \tag{5.106}
$$

$$
\begin{aligned}
&(T + \Delta T) \sin(\theta_1 - \psi_1) + (T + \Delta T) \sin(\theta_2 + \psi_2) \\
&\quad - (T - \Delta T) \sin(\theta_3 - \psi_3) \\
&\quad - (T + \Delta T) \sin(\theta_4 + \psi_4) = 0
\end{aligned} \tag{5.107}
$$

The corner cables forces equilibrium in *x* and *y* directions give two more equations – see (5.106) and (5.107). Solving Equations (5.23 – 5.95) and (5.99 – 5.107) for the 81 unknowns, the results are listed in the Tables 5.6 – 5.7.

Table 5.5. Designed parameters for the web-of-cables of the deformation problem

L_1(m)	1.0227	l_3(m)	0.2
L_2(m)	0.5041	K_1(m)	0.5327
L_3(m)	0.5005	K_2(m)	0.5037
l_1(m)	0.2857	h_1(m)	0.8163
l_2(m)	0.2214	h_2(m)	0.7551

Table 5.6. The web-of-cables tension and the corner cables length results after the deformation

$F_1 = F_7$(N)	13.374	$T_1 = T_9$(N)	2.1842
$F_2 = F_8$(N)	12.0654	$T_2 = T_{10}$(N)	1.3958
$F_3 = F_9$(N)	11.2005	$T_3 = T_{11}$(N)	1.3981
$F_4 = F_{10}$(N)	10.3646	$T_4 = T_{12}$(N)	1.0541
$F_5 = F_{11}$(N)	9.8846	$T_5 = T_{13}$(N)	0.2097
$F_6 = F_{12}$(N)	9.8264	$T_6 = T_{14}$(N)	2.3795
$R_1 = R_5$(N)	5.2929	$T_7 = T_{15}$(N)	1.0179
$R_2 = R_6$(N)	4.1846	$T_8 = T_{16}$(N)	0.0973
$R_3 = R_7$(N)	4.0488	$L_{01} = L_{03}$(m)	0.3882
$R_4 = R_8$(N)	4.05	$L_{02} = L_{04}$(m)	0.6313

Table 5.7. The web-of-cables angle results after the deformation

Angle	Value (deg.)	Angle	Value (deg.)
$\alpha_1 = \alpha_7$	16.2928	$\gamma_1 = \gamma_9$	24.3577
$\alpha_2 = \alpha_8$	8.3985	$\gamma_2 = \gamma_{10}$	32.5475
$\alpha_3 = \alpha_9$	2.9975	$\gamma_3 = \gamma_{11}$	36.6389
$\alpha_4 = \alpha_{10}$	2.9654	$\gamma_4 = \gamma_{12}$	32.6817
$\alpha_5 = \alpha_{11}$	8.2794	$\gamma_5 = \gamma_{13}$	24.9902
$\alpha_6 = \alpha_{12}$	9.4504	$\gamma_6 = \gamma_{14}$	7.031
$\beta_1 = \beta_5$	32.8934	$\gamma_7 = \gamma_{15}$	7.6092
$\beta_2 = \beta_6$	7.0395	$\gamma_8 = \gamma_{16}$	7.0398
$\beta_3 = \beta_7$	7.0378	$\theta_1 = \theta_3$	27.7876
$\beta_4 = \beta_8$	8.4143	$\theta_2 = \theta_4$	28.4137
		α	0.2373

The translation of the center of the plate is evaluated (see Table 5.8) from the following equations:

$$\delta_x = \frac{X}{2} - \frac{L}{2}\cos\alpha + (h_2\cos\gamma_7 + K_2\sin\beta_2 + K_1\sin\beta_1)\cos\alpha + (h_2\sin\gamma_7 + K_2\cos\beta_2 + K_1\cos\beta_1)\sin\alpha \quad (5.108)$$

$$\delta_y = \frac{Y}{2} - (h_2\cos\gamma_7 + K_2\sin\beta_2 + K_1\sin\beta_1)\sin\alpha + (h_2\sin\gamma_7 + K_2\cos\beta_2 + K_1\cos\beta_1)\cos\alpha \quad (5.109)$$

Table 5.8. Evaluating the coordinate of the centre of the thin plate after the deformation

δ_x(m)	δ_y(m)
$0.6214\times e^{-08}$	$0.5392\times e^{-08}$

The results shown in Table 5.8 indicate that the plate does not move; this is due to symmetric forcing. When the tension and angle of the deformation for each cable around the plate (the boundary cables) are evaluated, the in-plane stress distributions can be obtained. The boundary cable forces on the plate are decomposed into two components, in the x' and y' directions - see Fig. 5.5.

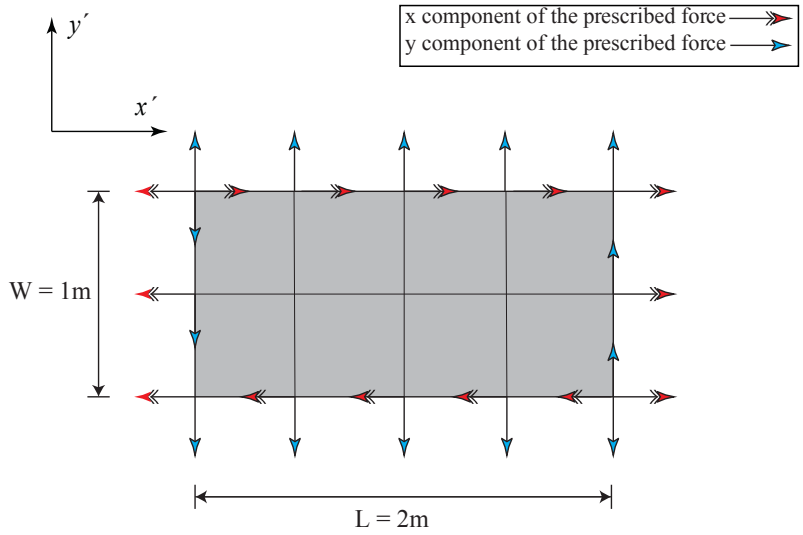

Figure 5.5. Thin rectangular plate with the components of the side forces – plate is comprised of eight squares of dimension 0.5m for each side.

5.3 In-Plane Stress Distribution

In section 3.2, we used FEM to derive the dynamic model for out-of-plane vibration for plate subjected to forces at discrete locations. The problem was divided into two parts: evaluating in-plane stress distributions and out-of-plane vibration analysis. Following the first part of the analysis, the in-plane stress distributions are obtained using our FEM code (in MATLAB) and verified with commercial FEM software (ANSYS). Each element has three stress values: two normal stresses in the x and y directions and one shear stress in xy plane. After we evaluated these three values for each element, we plotted the results for the entire plate. The results for both FEM methods for ΔT = 0 N are shown in the Figs. 5.6 – 5.8 and the difference between them are shown in Figs. 5.9 – 5.11.

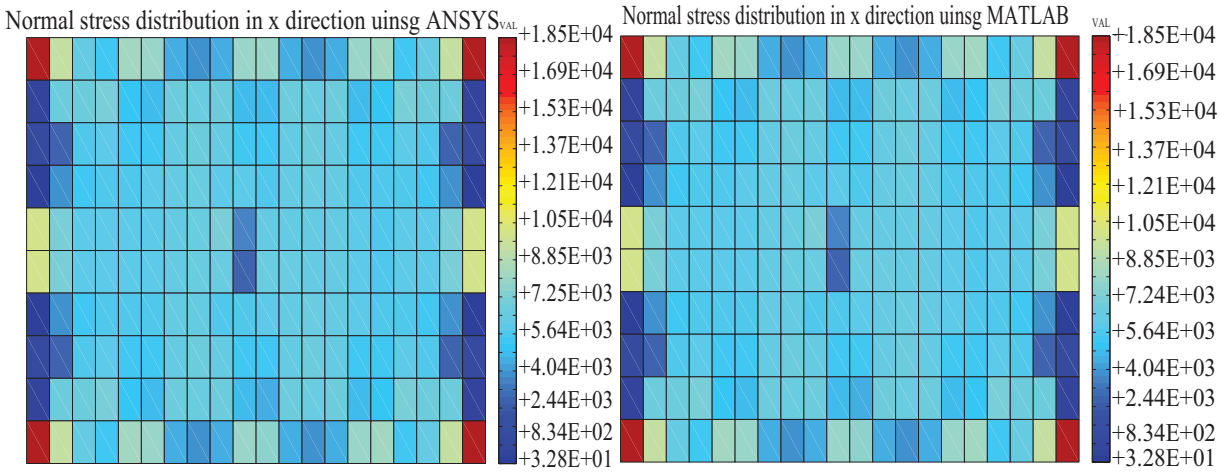

Figure 5.6. In-plane normal stress distribution in x direction when ΔT = 0 N

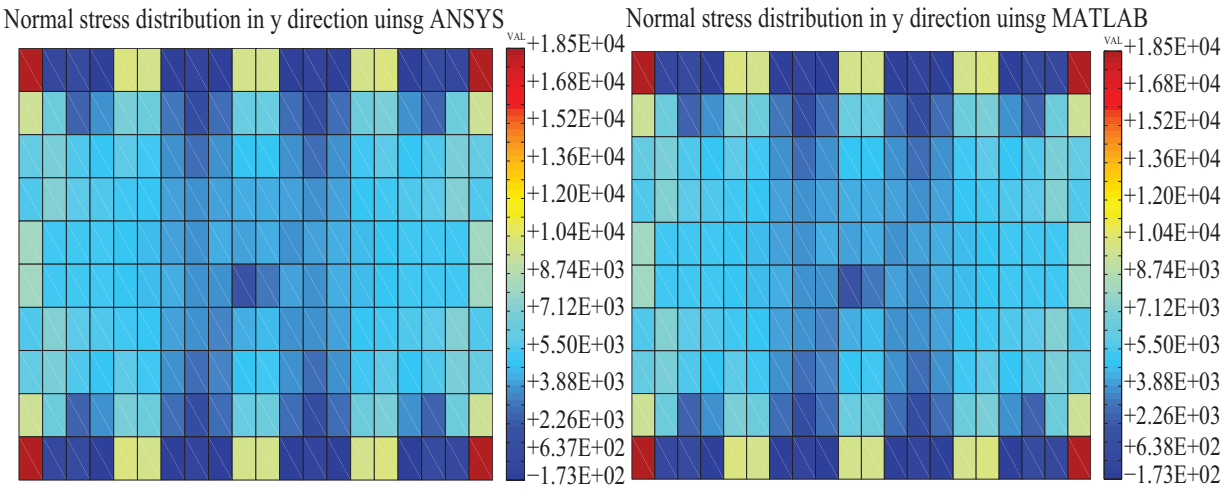

Figure 5.7. In-plane normal stress distribution in y direction when ΔT = 0 N

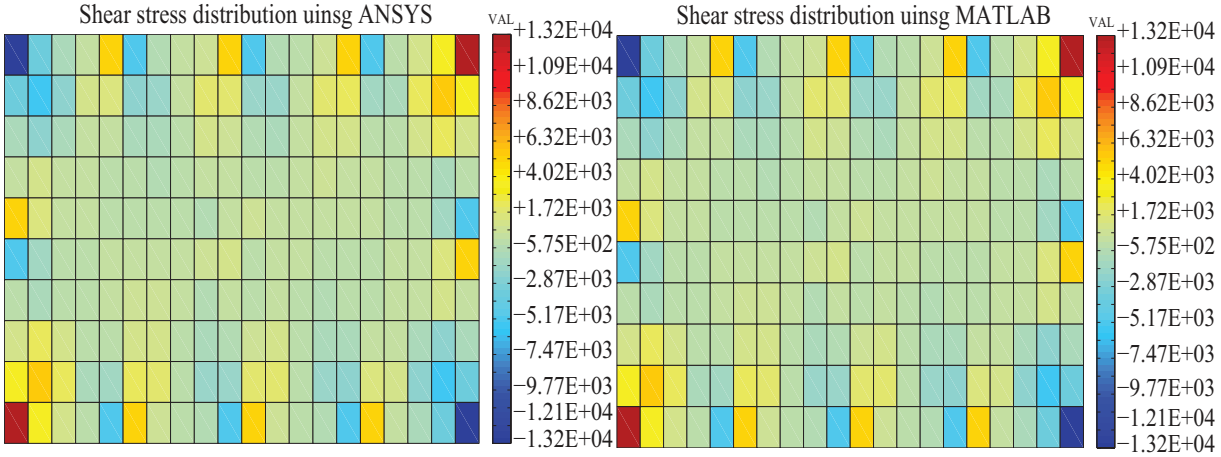

Figure 5.8. In-plane shear stress distributions when ΔT = 0 N

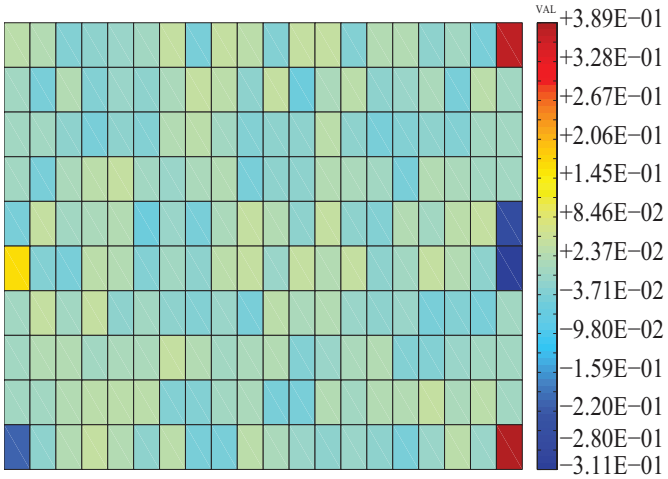

Figure 5.9. Difference between ANSYS and MATLAB code for the x direction stress distribution when ΔT = 0 N

Figure 5.9 shows that the maximum difference between both results for the stress distribution in the x direction is negligible, around 0.389. This difference is small compared to the maximum stress value of 1.85×10^4 N/m and can therefore be neglected.

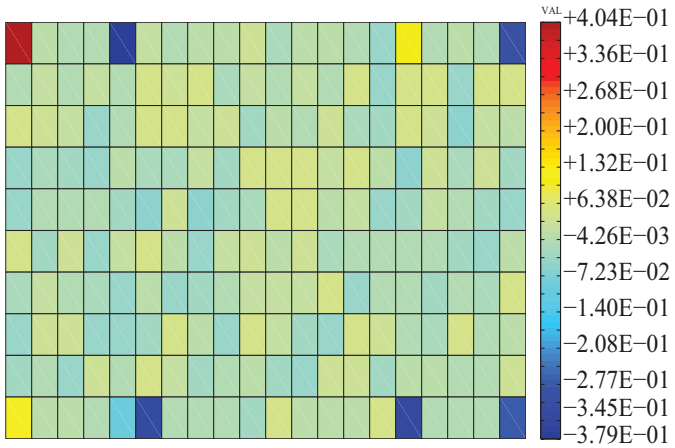

Figure 5.10. Difference between ANSYS and MATLAB code for the y direction stress distribution when ΔT = 0 N

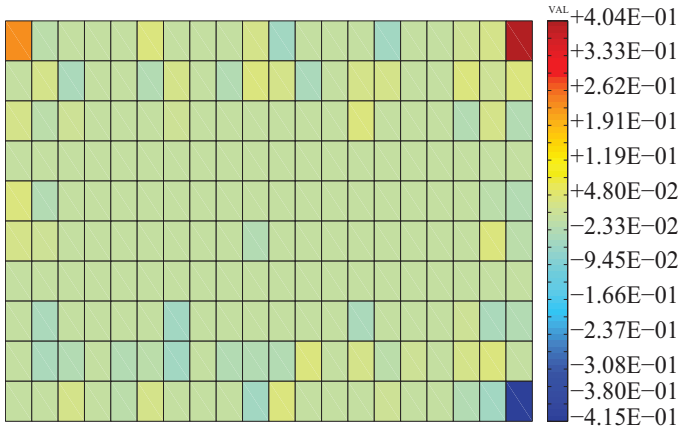

Figure 5.11. Difference between ANSYS and MATLAB code for the shear stress distribution when ΔT = 0 N

Figure 5.10 and 5.11 show that the maximum difference between both FEM results for both normal stresses in y direction and shear stresses in xy plane is equal to 0.4, which are also negligible.

For $\Delta T = 3$ N, the stress distributions are shown in Figs 5.12 – 5.14 for both FEM methods. The differences between the two methods are shown in Figs 5.15 – 5.17.

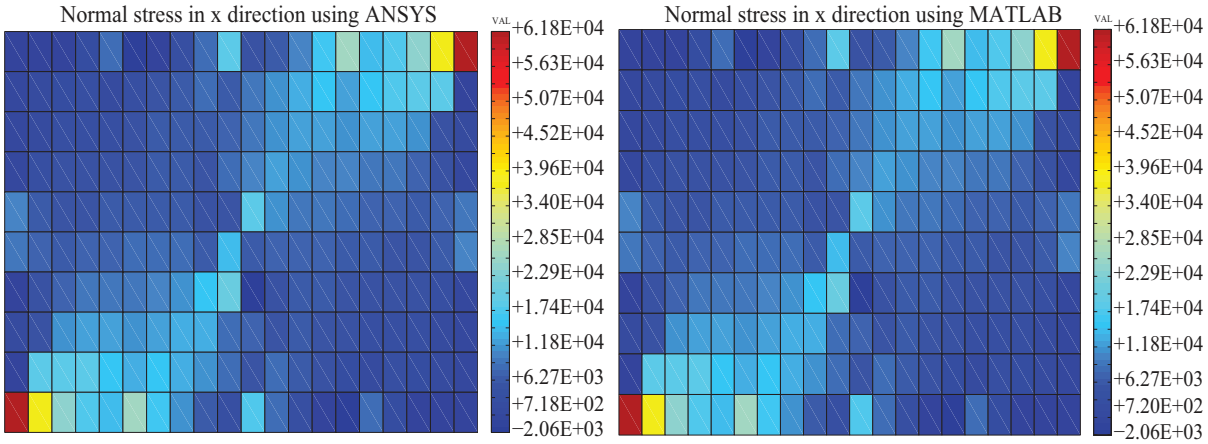

Figure 5.12. In-plane normal stress distribution in x direction when ΔT = 3 N

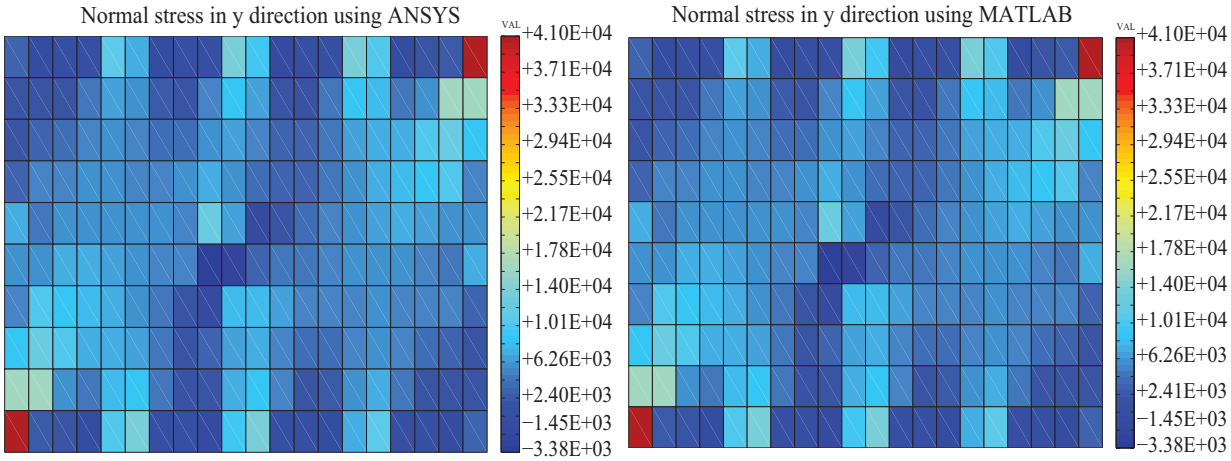

Figure 5.13. In-plane normal stress distribution in y direction when ΔT =3 N

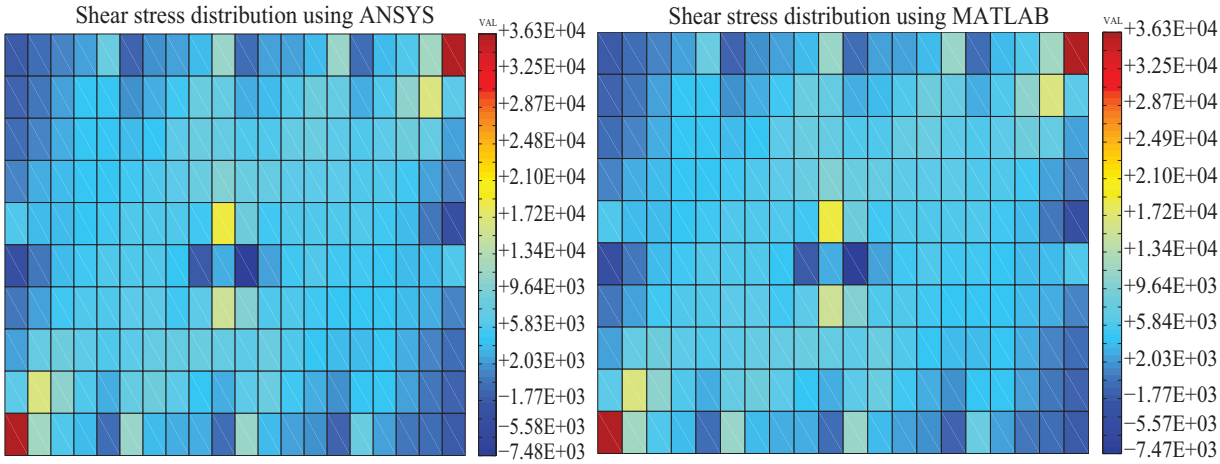

Figure 5.14. In-plane shear stress distributions when ΔT = 3 N

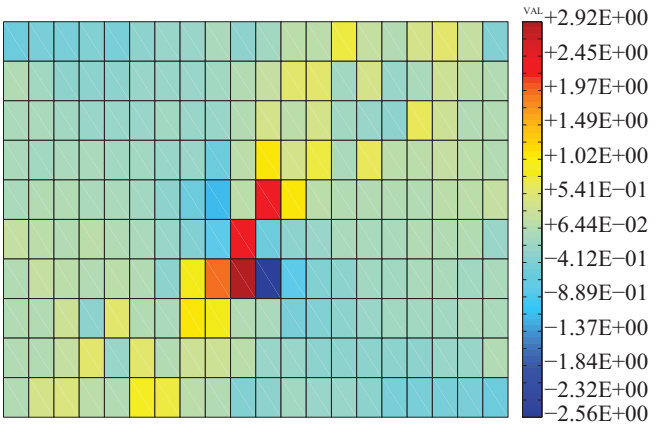

Figure 5.15. Difference between ANSYS and MATLAB code for the x direction stress distribution when ΔT = 3 N

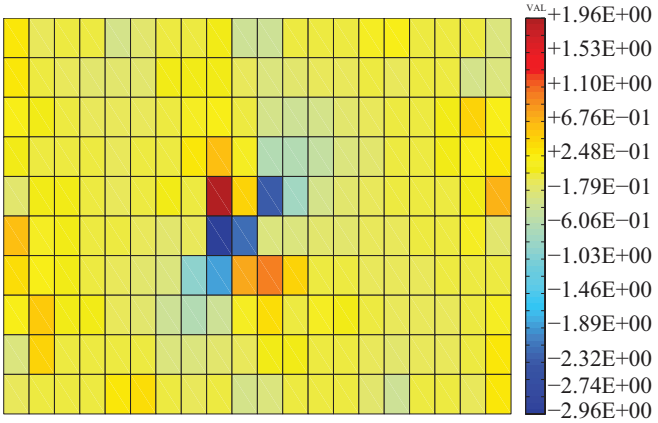

Figure 5.16. Difference between ANSYS and MATLAB code for the y direction stress distribution when ΔT = 3 N

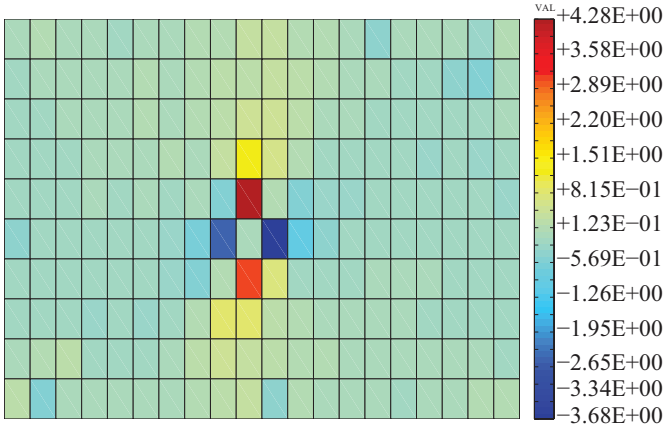

Figure 5.17. Difference between ANSYS and MATLAB code for the shear stress distribution when ΔT = 3 N

The maximum difference between ANSYS and MATLAB results when ΔT = 3 N are 0.2 for the stress in the *x* direction, 0.196 for the stress in the *y* direction, and 0.428 for the shear stress in the *xy* plane. These differences are quite small compared to the maximum stress value of the plate, which is 6.18×10^4 N/m, and can therefore be neglected.

5.4 Out-Of-Plane Vibration Analysis For Varying Boundary Conditions

An out-of-plane vibration analysis of the plate will be conducted using the pre-stress data obtained in section 5.3. In our previous vibration analysis (chapter 4), we assumed that the stresses are uniformly distributed around the plate due to uniformly distributed in-plane forces around the plate boundaries. In this chapter, the stress distribution is not assumed to be uniformly distributed. The analysis is done using MATLAB FEM code and verified using commercial FEM software (ANSYS). The results for a plate with simply supported boundaries are first listed in Table 5.9 and the mode shapes are shown in Figs. 5.18 and 5.19 using ANSYS and MATLAB respectively, for ΔT = 0 N. For ΔT = 3 N, the results are listed in Table 5.10 and the mode shapes shown in Figs. 5.20 and 5.21.

Table 5.9. Comparing ANSYS and MATLAB frequency analysis when ΔT = 0 N

Mode	MATLAB Frequency Hz	ANSYS Frequency Hz	Difference %
1	1.681	1.683	0.118835
2	2.639	2.62	0.719969
3	4.188	4.192	0.09541
4	5.309	5.526	3.92689
5	6.288	6.436	2.572
6	6.295	6.454	2.19

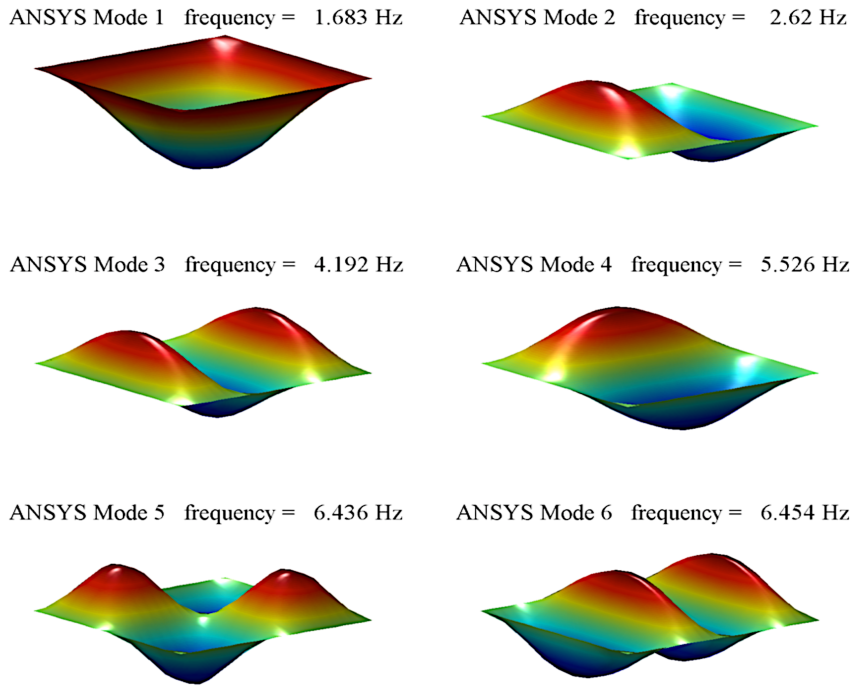

Figure 5.18. ANSYS frequency analysis when ΔT = 0 N

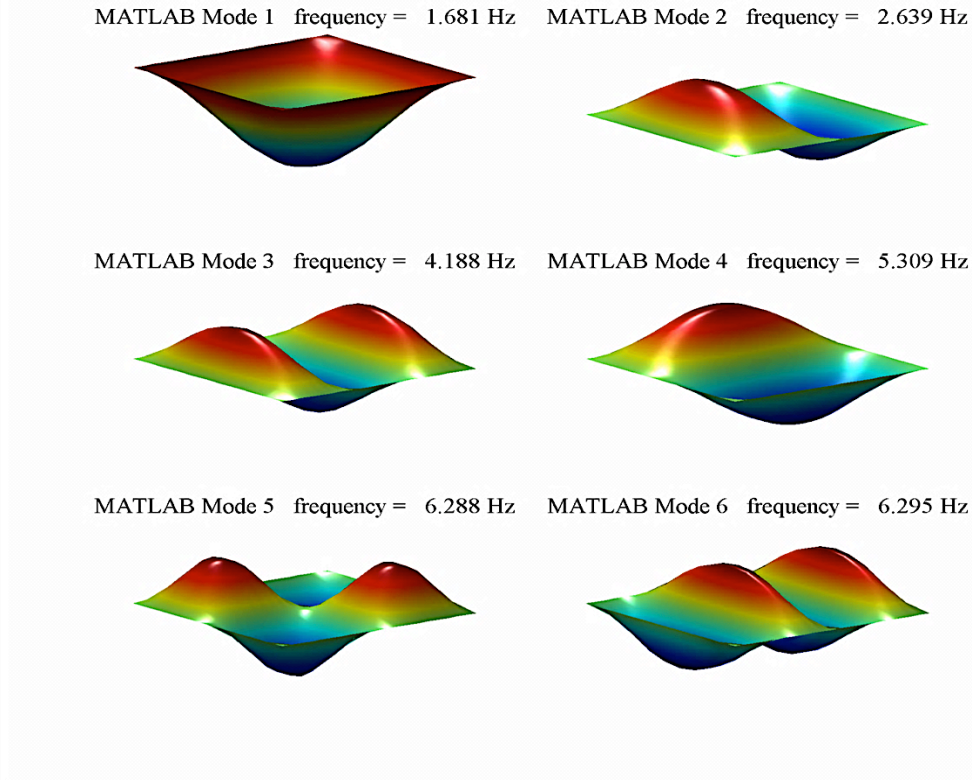

Figure 5.19. MATLAB frequency analysis when ΔT = 0 N

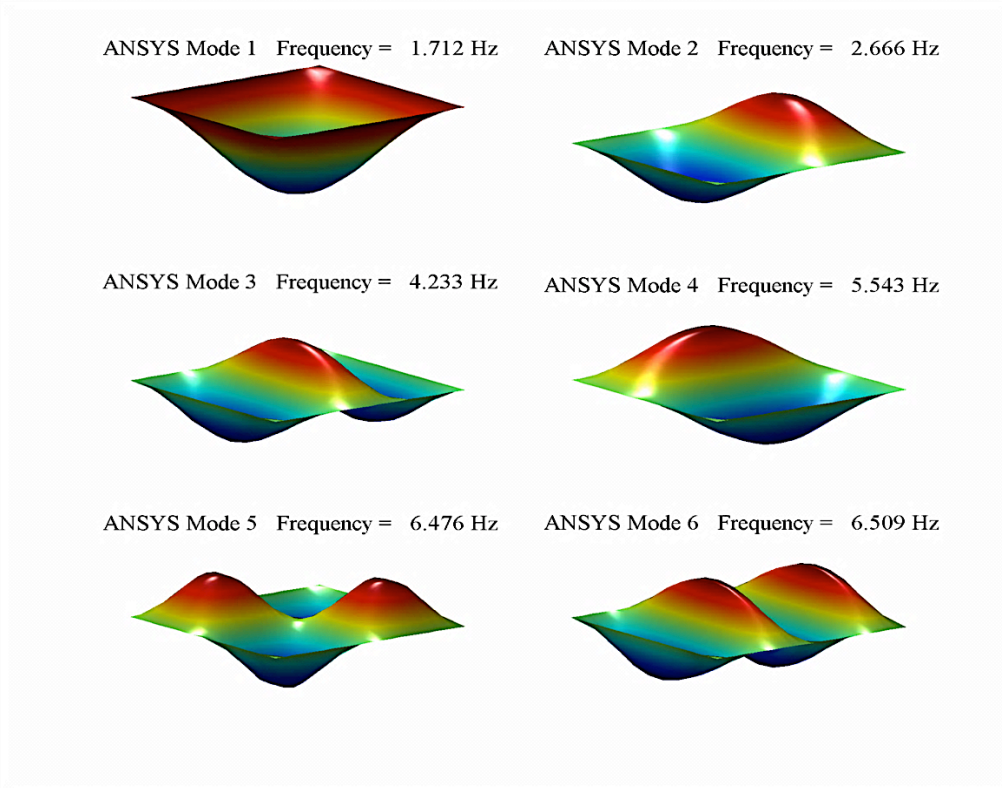

Figure 5.20. ANSYS frequency analysis when ΔT = 3 N

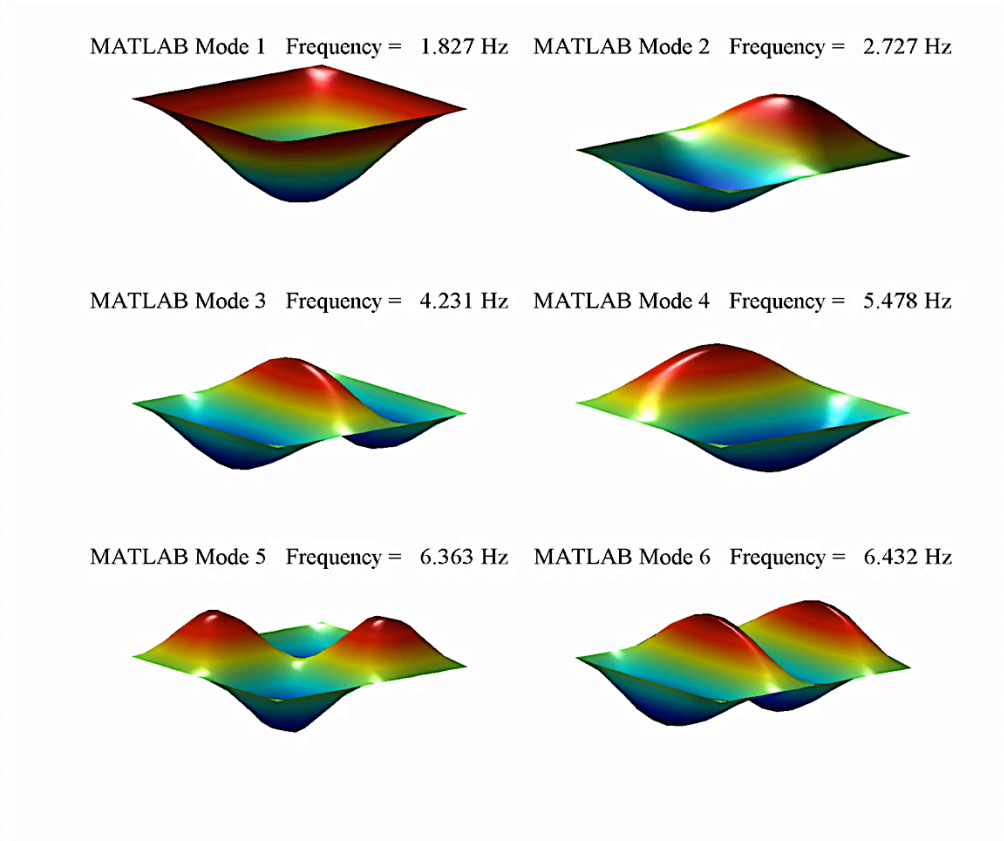

Figure 5.21. MATLAB frequency analysis when ΔT = 3 N

Table 5.10. Comparing ANSYS and MATLAB frequency analysis when ΔT = 3 N

Mode	MATLAB Frequency Hz	ANSYS Frequency Hz	Difference %
1	1.827	1.712	6.2944
2	2.727	2.666	16.6
3	4.231	4.233	0.04724
4	5.478	5.543	0.876
5	6.363	6.476	2.24
6	6.432	6.509	0.679

The changes in the plate modes and frequencies are examined using MATLAB results for $\Delta T = 0$ and $\Delta T = 3\ N$. These changes are presented in Table 5.11.

$$\phi_i^T \boldsymbol{M} \varphi_i = \boldsymbol{I} \tag{5.110}$$

where ϕ_i is ith mode with ΔT = 0 N and φ_i is ith mode with ΔT = 3 N, $\boldsymbol{M}$ is the mass matrix, and $\boldsymbol{I}$ is the identity matrix.

Table 5.11. Comparing MATLAB frequency analysis when ΔT = 0 and 3 N

Mode (i)	Frequency Hz for ΔT = 0 N	Frequency Hz for ΔT = 3 N	Difference %	$\phi_i^T \boldsymbol{M} \varphi_i$
1	1.681	1.827	7.99124	0.9993
2	2.639	2.727	3.22698	0.999
3	4.188	4.231	1.0872	0.9982
4	5.309	5.478	3.085	0.9987
5	6.288	6.363	1.1786	0.9958

As expected, the entries in the last column are not identically unity since $\phi_i \neq \varphi_i$. Also, all the natural frequencies increase as ΔT is increased.

The stiffness matrix of the web-of-cables structure is evaluated and added as elastic boundary conditions for a floating plate to replace the simply supported boundary condition. To evaluate the stiffness matrix of the web-of-cables structure, we model the plate and the surrounding web as shown in Fig. 5.22.

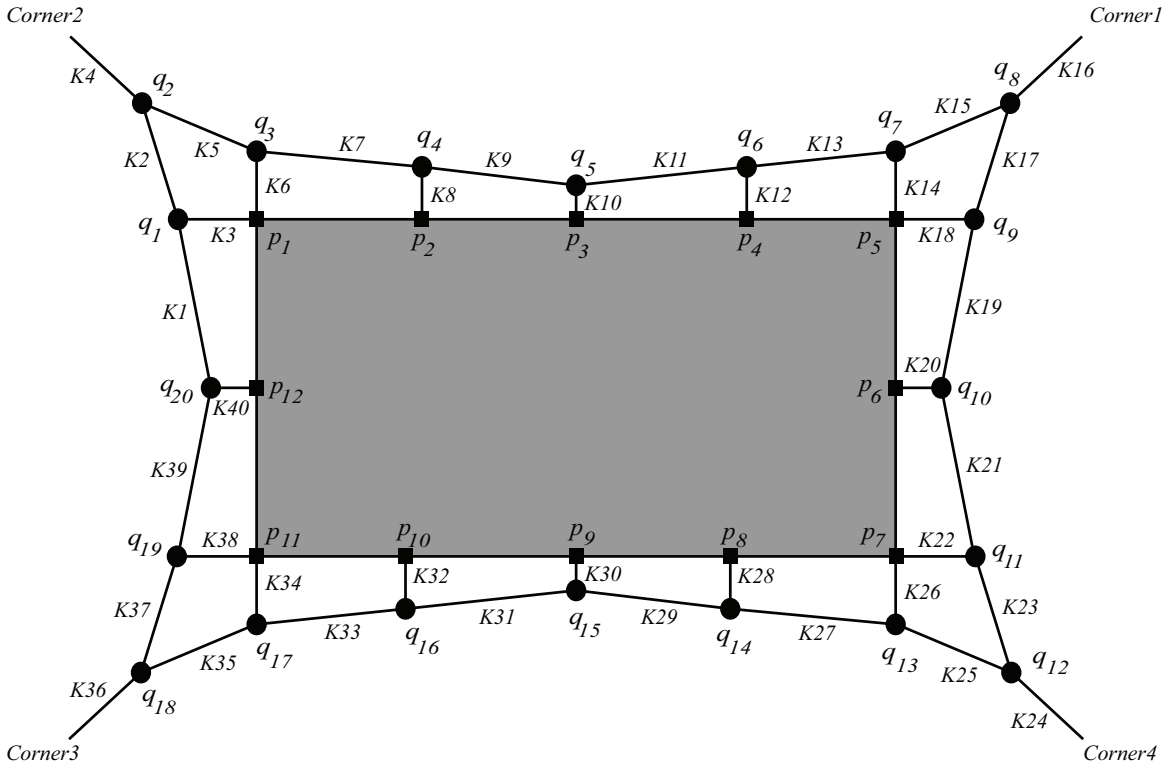

Figure 5.22. Web-of-cables stiffness evaluation

The points where the web-of-cables attaches to the plate are marked as p_i, where i = 1, 2,…,12. The knot points that the web cables join each other are marked as q_j, where j = 1, 2,…,20. The displacement of each of these point (p_i or q_j) in z direction is assumed to be Z_n, where n = 1, 2,.., 32. Some of these new DOF in z direction are added to the global DOF of the plate structure. Therefore, the web-of-cables and the plate are considered to be a one structure. The stiffness of each cable is labeled as K_s (s = 1, 2,.., 40) and can be evaluated by dividing the tension on the cable by its length. Using second order partial derivatives (the Hessian matrix method), the web-of-cables stiffness matrix, $E^{s\times s}$, can be obtained as follows

$$E^{s\times s} = \begin{bmatrix} \frac{\partial^2 E_{total}}{\partial {z_1}^2} & \frac{\partial^2 E_{total}}{\partial z_1 \partial z_2} & \cdots & \frac{\partial^2 E_{total}}{\partial z_1 \partial z_n} \\ \frac{\partial^2 E_{total}}{\partial z_2 \partial z_1} & \frac{\partial^2 E_{total}}{\partial {z_2}^2} & \cdots & \frac{\partial^2 E_{total}}{\partial z_2 \partial z_n} \\ \vdots & \vdots & \ddots & \vdots \\ \frac{\partial^2 E_{total}}{\partial z_n \partial z_1} & \frac{\partial^2 E_{total}}{\partial z_n \partial z_2} & \cdots & \frac{\partial^2 E_{total}}{\partial {z_n}^2} \end{bmatrix} \tag{5.111}$$

where E_{total} is the total potential energy of the web-of-cables structure and can be obtained from the summation of the potential energy of each cable.

$$E_{total} = \sum_{s=1}^{40} \frac{1}{2} K_s \, {\Delta z_s}^2 \tag{5.112}$$

where Δz_s is the difference between the displacements of the two ends of the cable in z direction. After the stiffness matrix of the web-of-cables, $E^{s\times s}$, is obtained, we connected the two structures through their associated DOF (more DOF will be added to the global DOF of the mass and stiffness matrices). The structure stiffness, $E^{s\times s}$, increases the stiffness of the boundaries of the global stiffness matrix **K** of the floating plate in the frequency analysis. In addition, the stiffness matrix **K** also includes the pre-stress effect that is caused by adding the web-cable forces, which is done using pre-stress information to obtain the frequency analysis as presented in section 5.3. The first five out-of-plane vibration frequencies and modes are listed in Table 5.12 and shown in Figs 5.23 – 5.26 respectively for different values of ΔT.

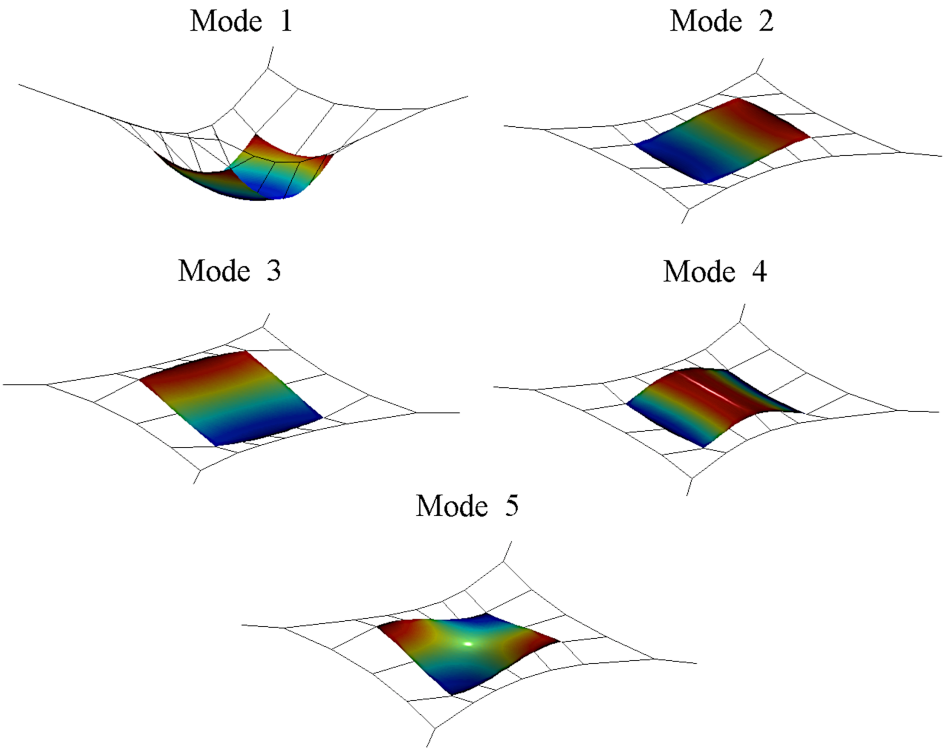

Figure 5.23. Out-of-plane vibration results when ΔT = 0 N

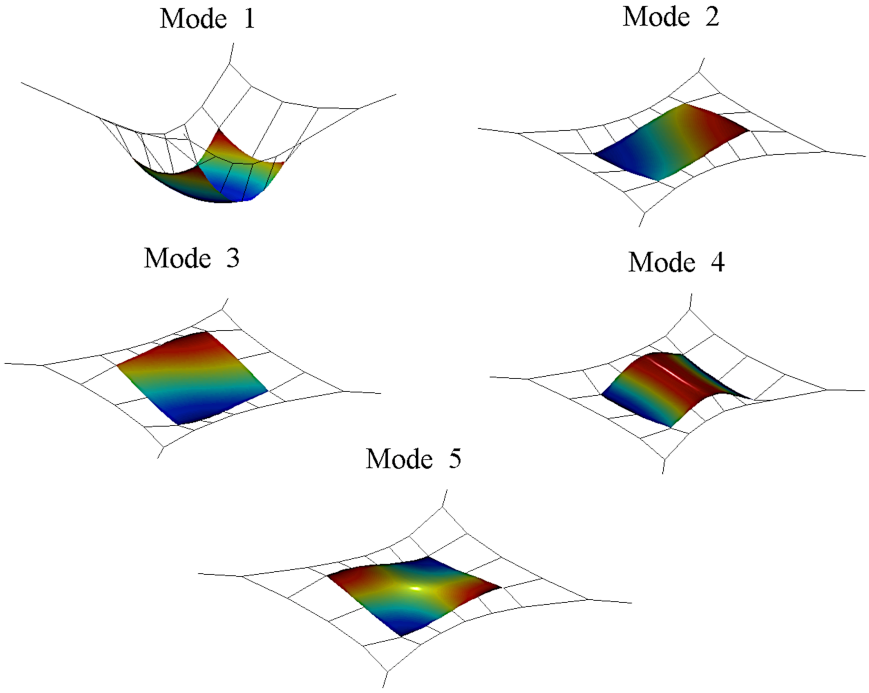

Figure 5.24. Out-of-plane vibration results when ΔT = 1 N

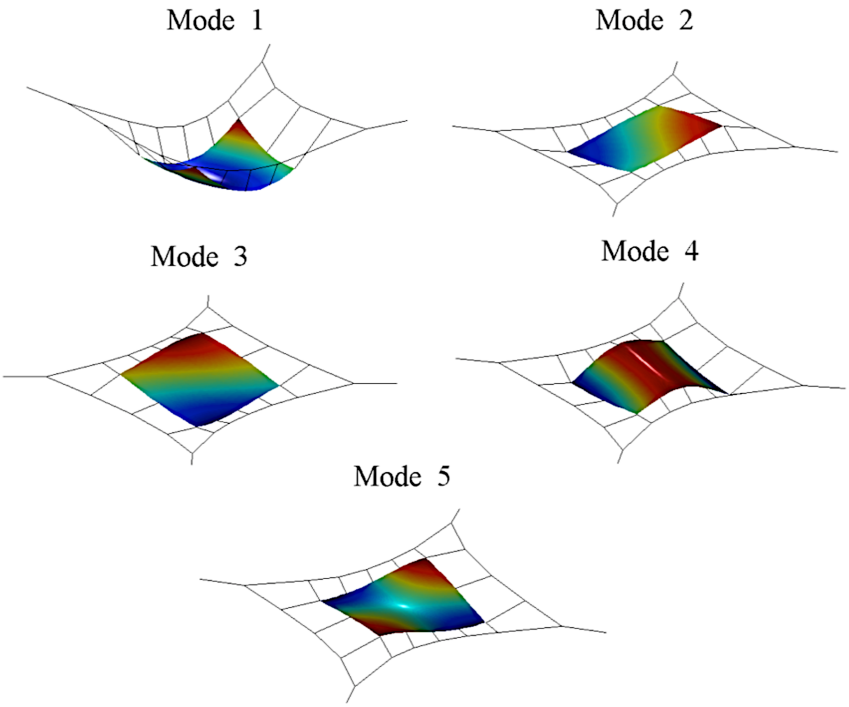

Figure 5.25. Out-of-plane vibration results when ΔT = 2 N

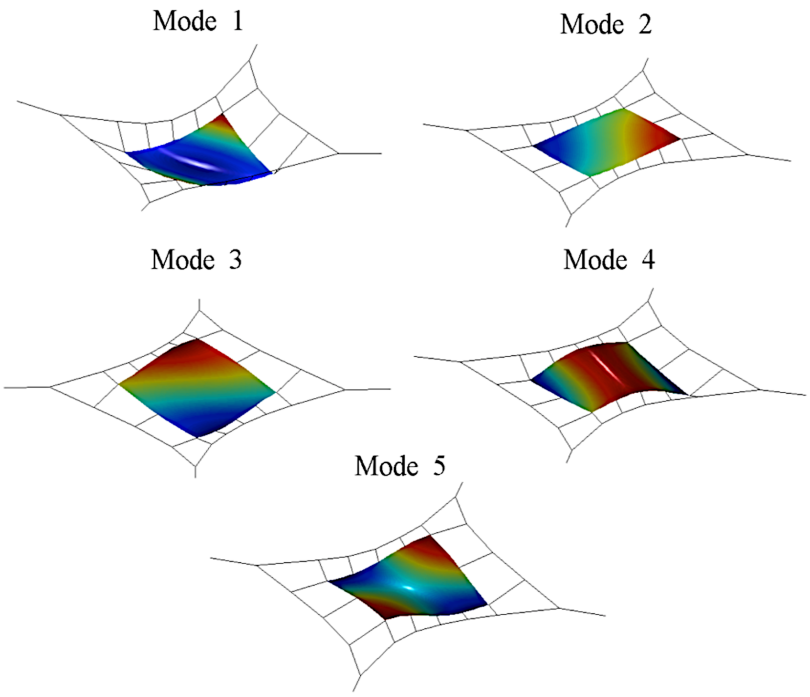

Figure 5.26. Out-of-plane vibration results when ΔT = 3 N

Table 5.12. MATLAB frequency analysis for different ΔT values

First Five Eigenvalues				
Modes	$\Delta T = 0$ N	$\Delta T = 1$ N	$\Delta T = 2$ N	$\Delta T = 3$ N
1	6.3649	6.3793	6.4128	6.4188
2	17.6285	16.5403	14.4832	12.15
3	21.2724	22.317	24.1678	26.0546
4	44.6023	43.6041	40.8418	36.9578
5	75.4323	76.4714	79.2026	82.835

From Table 5.12, we can observe that the modes 2 and 4 are decreased as the value of ΔT increased. However, the frequencies are increased as we increased the value of ΔT for the other modes.

5.5 Control Scheme Using The Web-OF-Cables Structure

In this section, the control scheme introduced in chapter 4 is used to control the vibration of a floating rectangular Aluminum plate using the web-of-cables structure. The in-plane forces that are created by the web-of-cables structure are controlled using the control logic (4.7) or (4.12) through variation in the tension of the corner cables above their nominal values. Following section 4.1, the modes (of a plate with similar dimension and properties as in chapter 4) are examined using the initial conditions below.

$$\begin{bmatrix} w_1 \\ w_2 \\ w_3 \\ w_4 \\ w_5 \\ \dot{w}_1 \\ \dot{w}_2 \\ \dot{w}_3 \\ \dot{w}_4 \\ \dot{w}_5 \end{bmatrix} = \begin{bmatrix} 0.01 \\ 0.2 \\ 0.4 \\ 0.1 \\ 0.3 \\ 0 \\ 0 \\ 0 \\ 0 \\ 0 \end{bmatrix} \tag{5.113}$$

FEM models for different value of corner tensions (see section 5.4 for example), where the system stiffness matrix $K = diag\,(\omega_i^2)$ and the proportional damping matrix $D = \beta K$ with $\beta = 0.0002$, are used to investigate the efficacy of the control strategy. The energy dissipation and the modal displacement for the system in absence of the control scheme are shown in Figs. 5.27 and 5.28 below; these figures will be compared with results obtained with different control schemes.

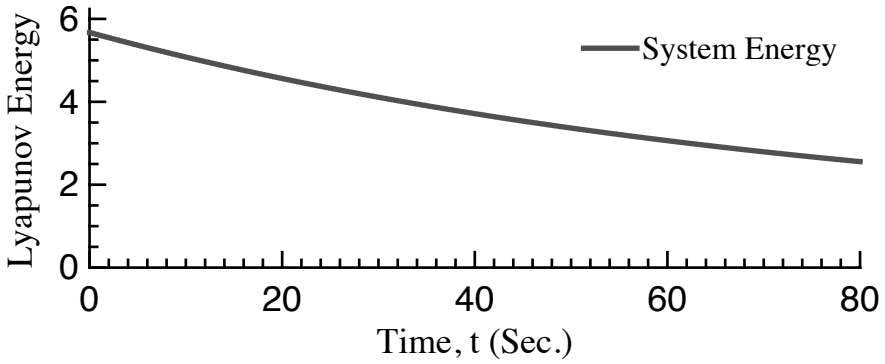

Figure 5.27. Energy dispassion for the system without control

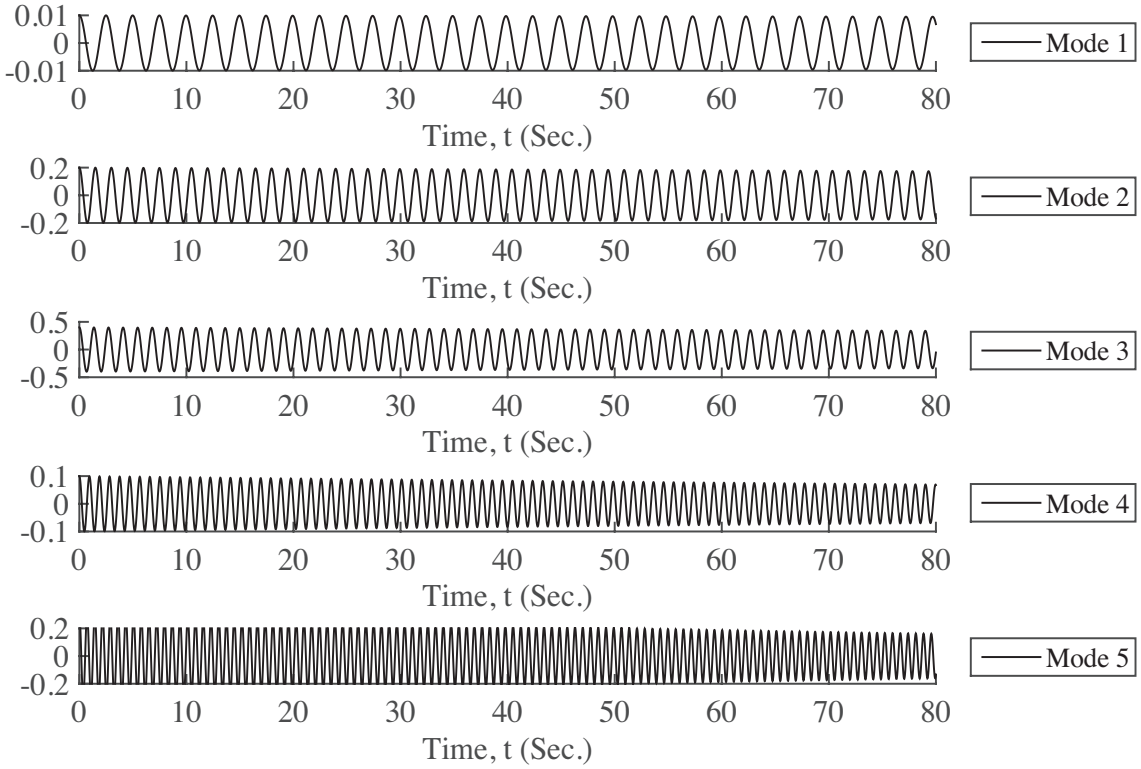

Figure 5.28. Modal displacement for the system without control

5.5.1 Adding ΔT To The Four Corner Cables

The control scheme in section 4.1 is investigated for the floating plate by switching ΔT in the corner cables tensions between 0 and 3 N. For The initial conditions in (5.113), the results of control scheme in (4.7) are shown in Figs. 5.29 – 5.31.

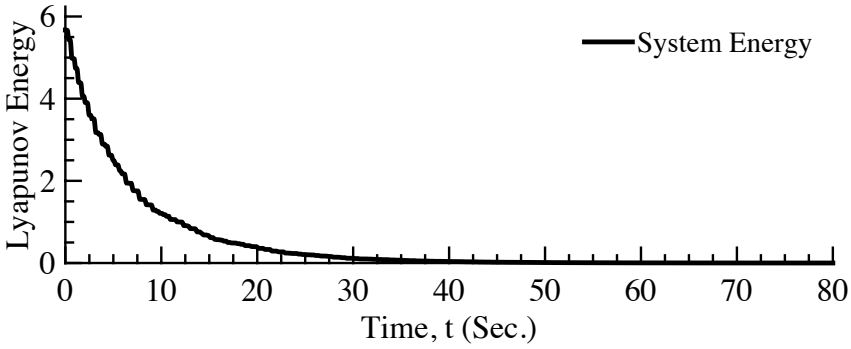

Figure 5.29. Energy dissipation using the control logic in (4.7) - adding ΔT = 3 N to the four corner cables

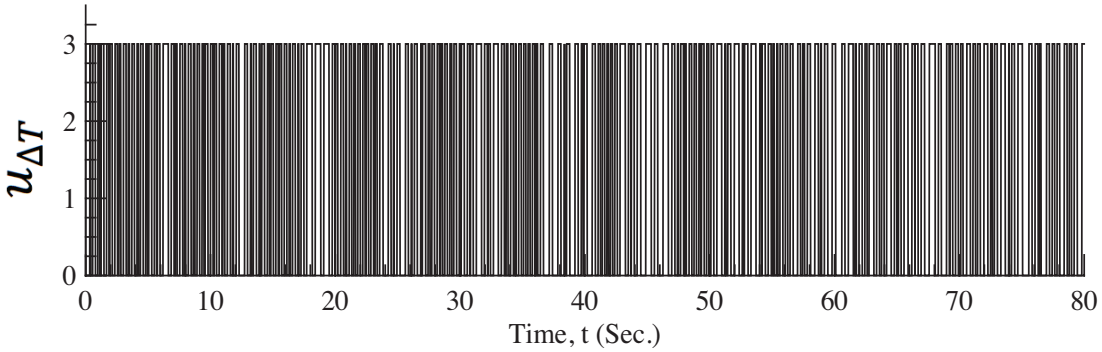

Figure 5.30. Input force using the control logic in (4.7) - adding ΔT = 3 N to all four corner cables

A comparison of Fig. 5.29 with Fig. 5.27 shows that the controller is effective in suppressing the vibration of the plate using the web-of-cables structure. The vibration energy is converged to zero in approximately 60 seconds. In the absence of the control scheme, only 30% of the system energy decay out in 60 seconds due to the damping in the system. The modal displacements results for the controlled system are shown in Fig. 5.31.

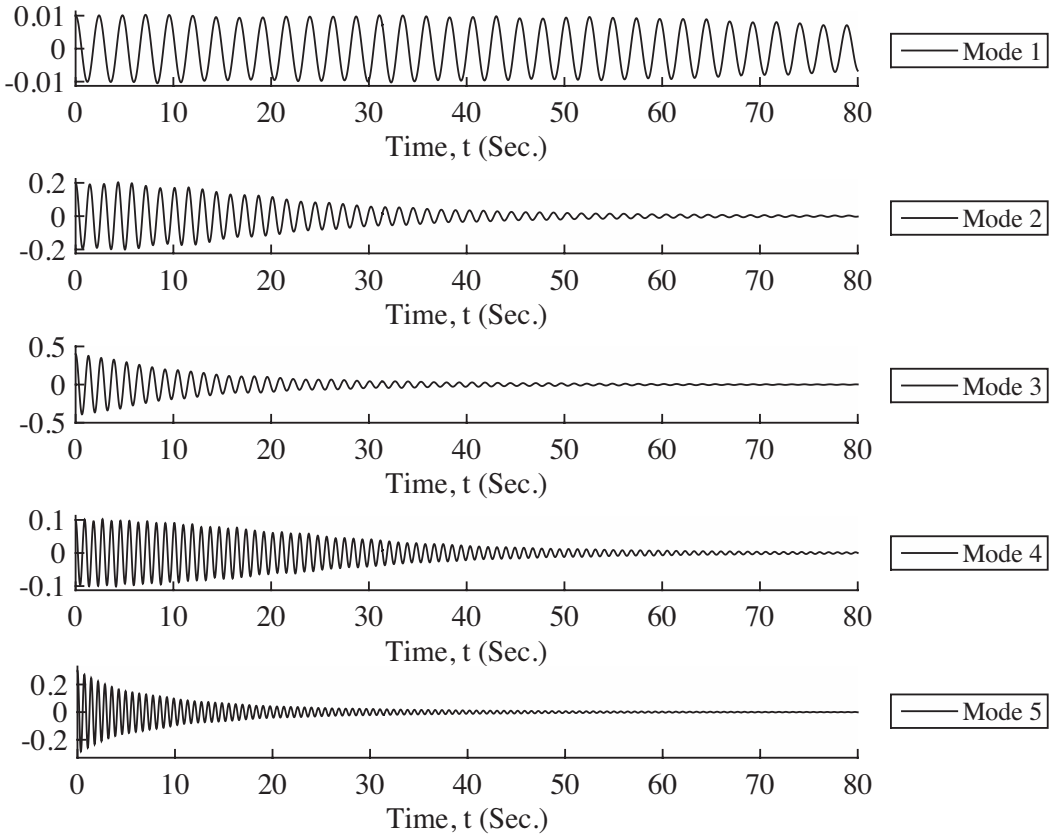

Figure 5.31. Modal displacements using the control logic in (4.7) - adding ΔT = 3 N to all four corner cables

Figure 5.31 shows that the modal displacements for the higher modes are converged to zero in approximately 60 seconds; however, in absence of the control the modal displacements for those modes did not converge to zero even after 80 seconds as shown in Fig 5.28. From Fig. 5.31, we also observe that the controller does not suppress the vibration in the first mode. The results of modified control logic in (4.12) are shown in Figs. 5.32 – 5.34; the time constant of the low pass filter and the saturation constant were chosen as $\tau = 0.15$ and $\varepsilon = 0$.

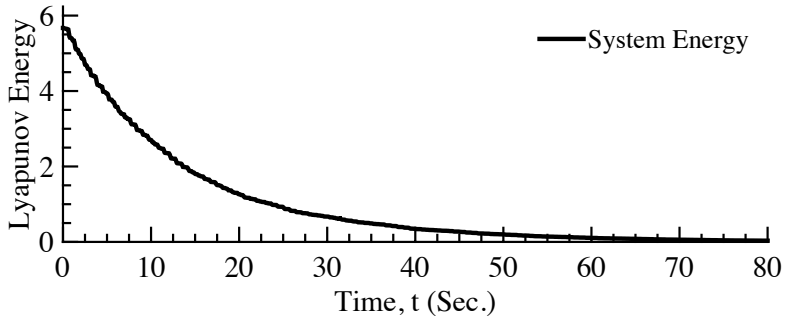

Figure 5.32. Energy dissipation using the modified control logic (4.12) with $\varepsilon = 0$ - adding ΔT = 3 N to all four corner cables

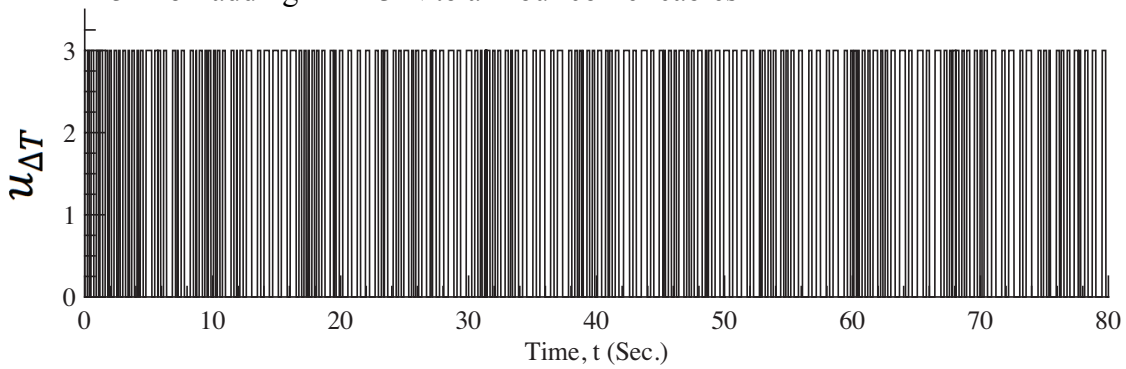

Figure 5.33. Forcing input using the modified control logic (4.12) with $\varepsilon = 0$ - adding ΔT = 3 N to all four corner cables

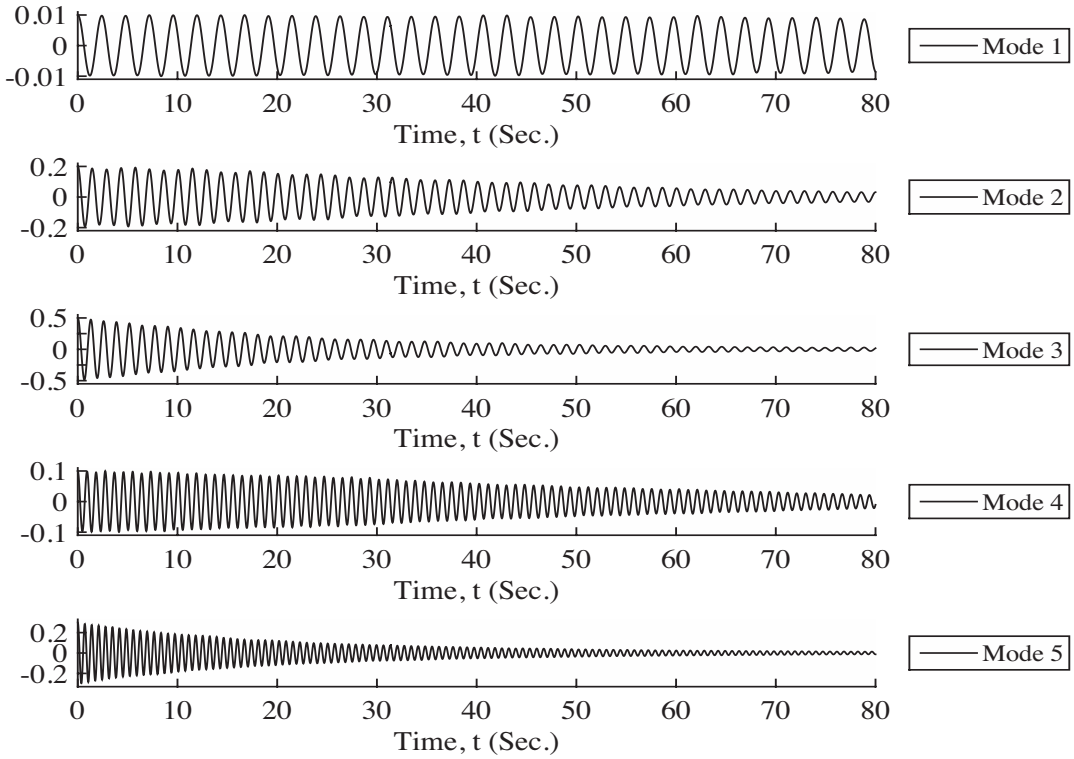

Figure 5.34. Modal displacement using the modified control logic (4.12) with $\varepsilon = 0$ - adding ΔT = 3 N to all four corner cables

From Figs. 5.32 and 5.34, we observe that the energy and modal displacements take more time to converge to zero comparing with the unmodified control (4.7). However, the switching frequencies of the input forces are decreased compare with the unmodified control logic (4.7) – see Fig. 5.33. Adding saturation to the modified control logic (4.12) using $\varepsilon = 0.09$ (to converge the input forces to zero as the system vibration subsided), the results are shown in Figs. 5.35 – 5.37.

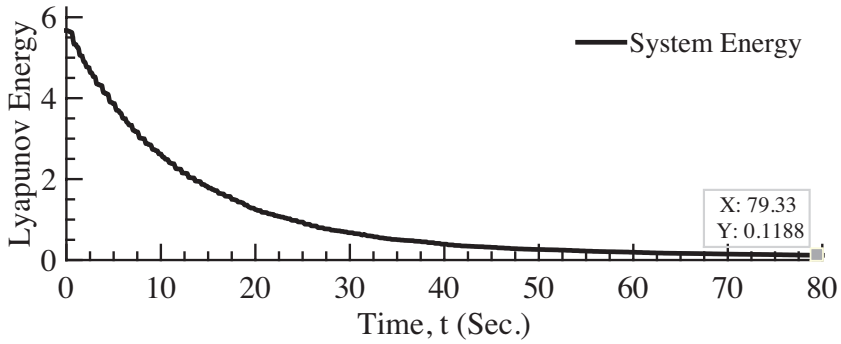

Figure 5.35. Energy dissipation using the modified control logic (4.12) - adding ΔT = 3 N to all four corner cables

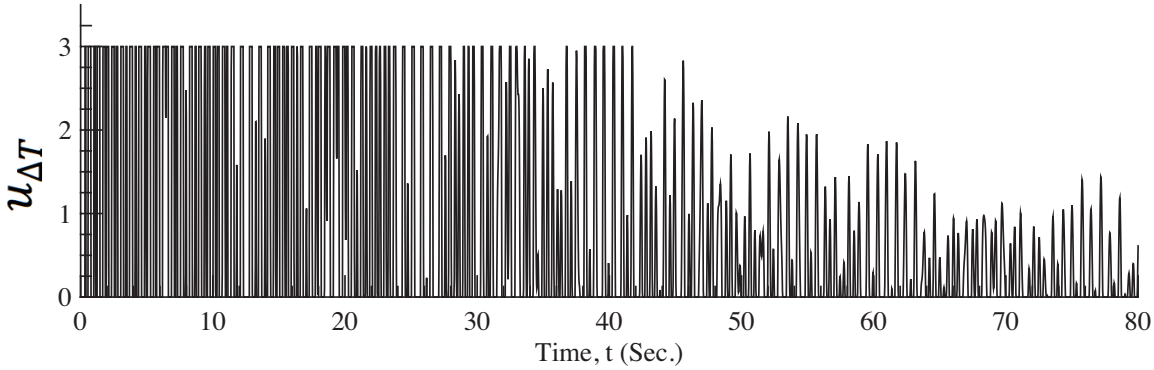

Figure 5.36. Forcing input using the modified control logic (4.12) - adding ΔT = 3 N to all four corner cables

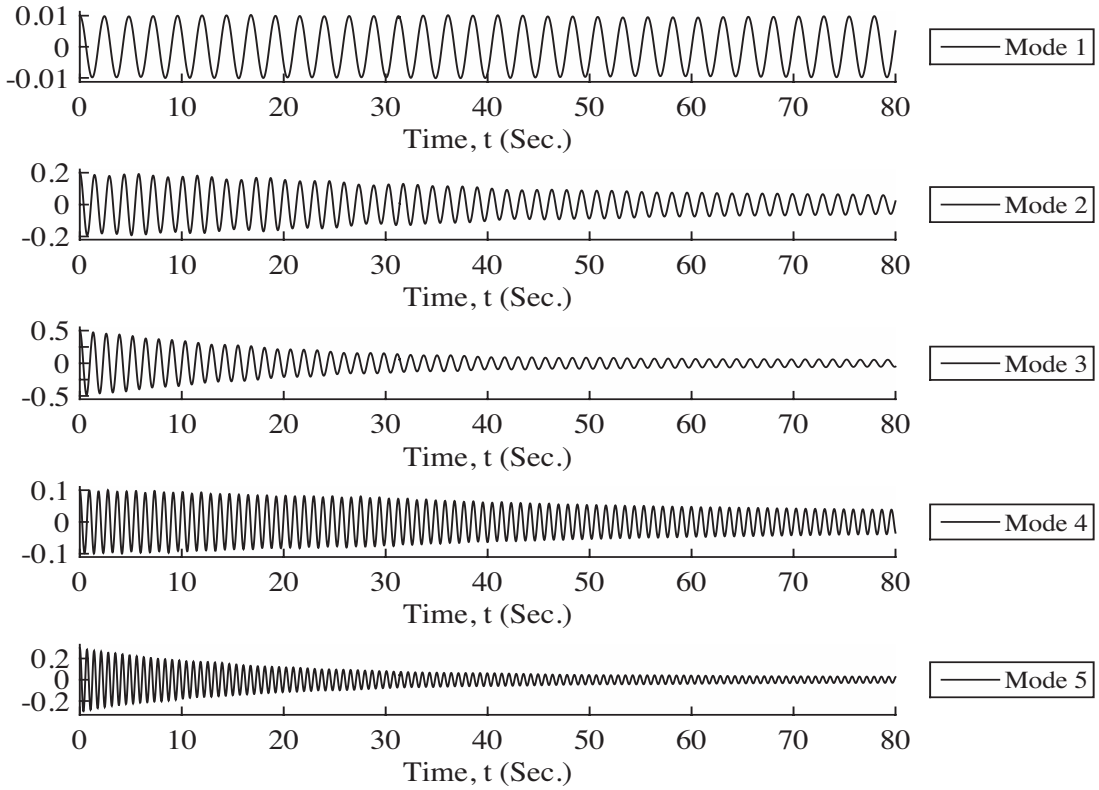

Figure 5.37. Modal displacements using the modified control logic (4.12) - adding ΔT = 3 N to all four corner cables

From Fig. 5.36, we can observe that the input forces are converged to zero as the system vibration converged to zero. However, the energy and modal displacements take more time to decay out compared with the unmodified control scheme in (4.7). This is the price that we should pay to get an input force that less frequently added and converge to zero as the vibration subsides. Comparing the modified control logic results with and without the saturation (as shown in Figs. 5.35 – 5.37 and Figs. 5.32 - 5.34 respectively), we observe that adding the saturation reduce the efficacy of the control logic by increasing the vibrating time. This effect can be observed in Fig. 5.35, where the system at time t = 79.33 seconds still has an energy equal to 0.1188.

5.5.2 Adding ΔT To Two Corner Cables And Subtracting ΔT From The Other Two Corner Cables

In the previous subsection, the control scheme is investigated by switching ΔT between zero and 3 N in all four corner-cables. That means the web-of-cables structure apply equal perpendicular tensions on the plate boundaries. Therefore, the plate is not subjected to shear forces along the boundaries. In this subsection, we modify the configuration of the web-of-cables structure by adding the ΔT = 3 N to two corner cables tension, T, and subtracting it form the other two corner cables (the new configuration presented in section 5.2). This modification will create shear forces in addition to in-plane forces around the boundaries as presented in section 5.4. The control scheme (section 4.1) results are shown below using the initial conditions in (5.113).

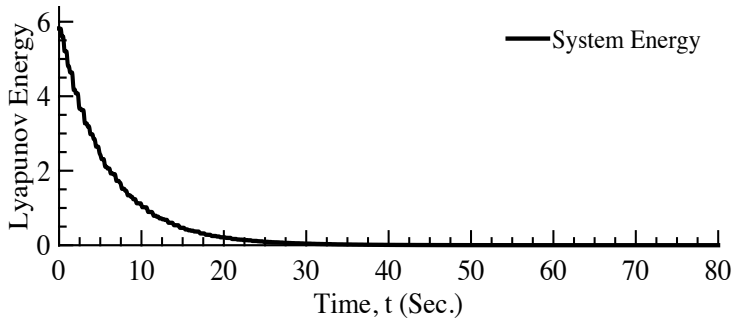

Figure 5.38. Energy dissipation using the control logic (4.7) - adding and subtracting ΔT = 3 N to two opposite corner cables respectively

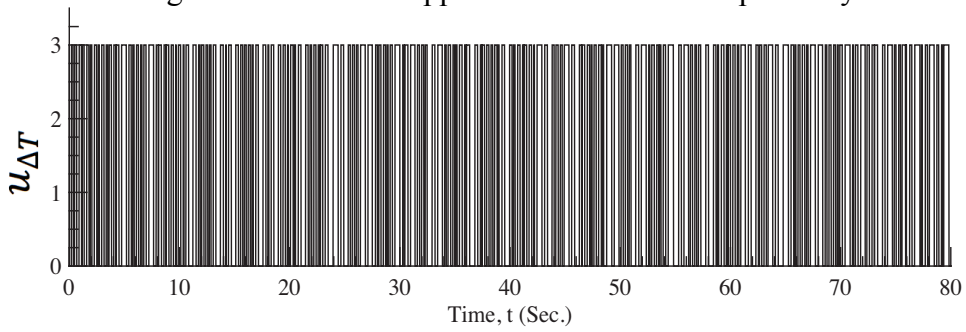

Figure 5.39. Forcing input using the control logic (4.7) - adding and subtracting ΔT = 3 N to two opposite corner cables respectively

From Fig. 5.38, we observe that introducing this new switching scheme successfully controlled the vibration within 50 seconds. This means the shear forces that are generated by the new configuration lowered the vibrating time by 10 seconds. Once again, we observe that the control

logic does not suppress the vibration in the first mode, but the modal displacements for the higher modes decay out within 50 seconds as shown in Fig. 5.40 below. However, the modal displacements for previous configuration (section 5.5.1) takes 60 seconds to do that – see Fig. 5.31. The modified control logic (4.12) results are shown in Figs. 5.41 – 5.43; the time constant of the low-pass filter and the saturation constant were chosen as $\tau = 0.15$ seconds and $\varepsilon = 0$.

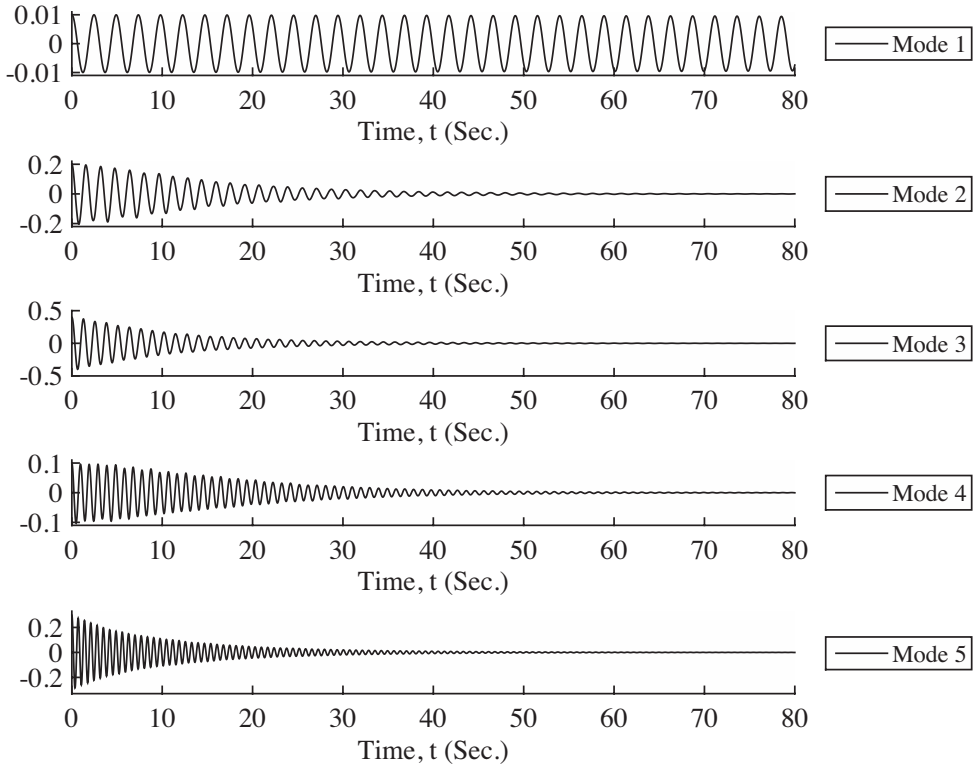

Figure 5.40. Modal displacements using the control logic (4.7) - adding and subtracting ΔT = 3 N to two opposite corner cables respectively

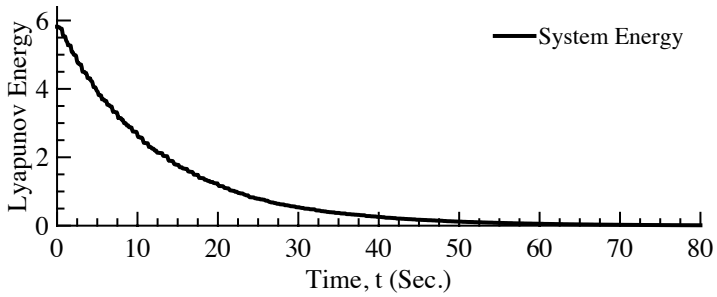

Figure 5.41. Energy dissipation using the modified control logic (4.12) with $\varepsilon = 0$ - adding and subtracting ΔT = 3 N to two opposite corner cables respectively

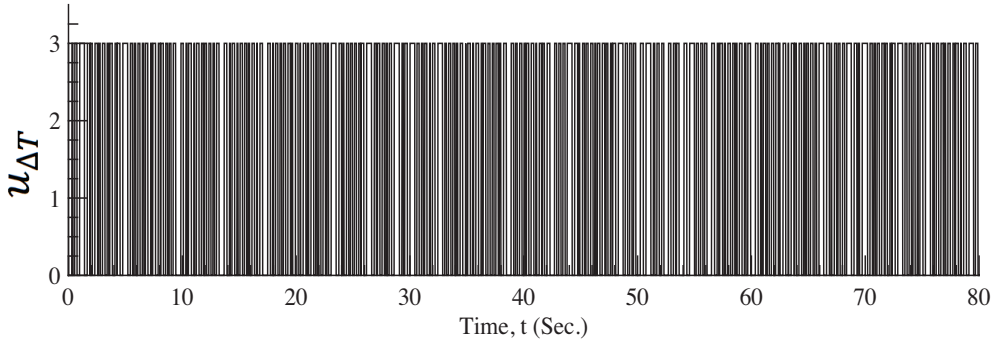

Figure 5.42. Forcing input using the modified control logic (4.12) with $\varepsilon = 0$ - adding and subtracting ΔT = 3 N to two opposite corner cables respectively

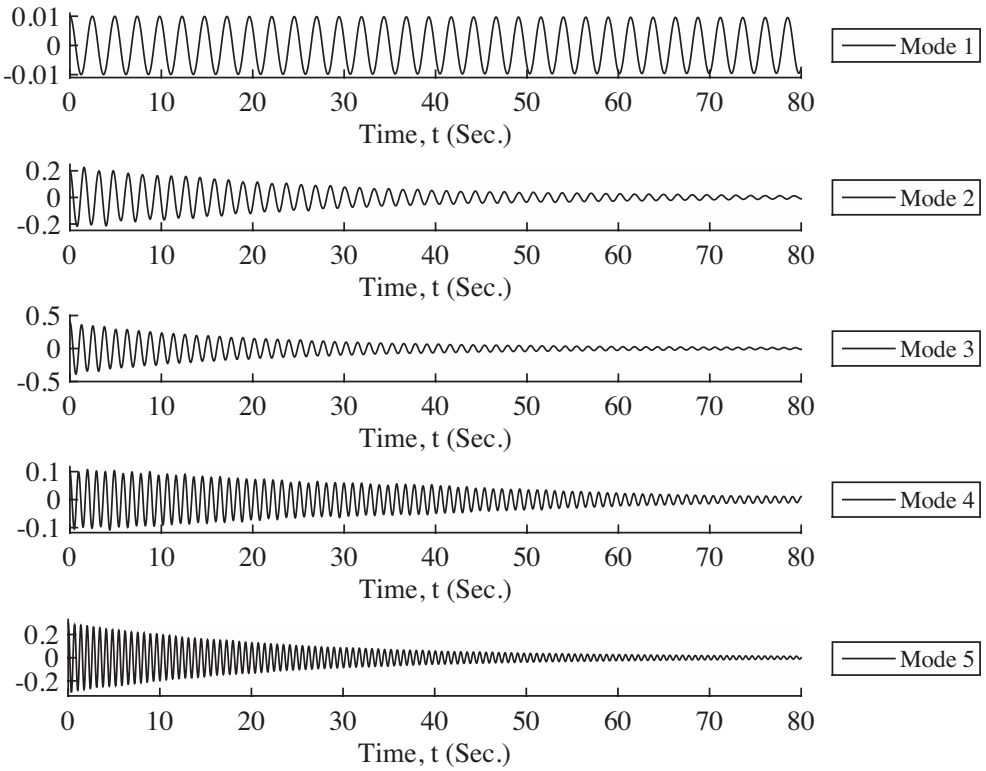

Figure 5.43. Modal displacements using the modified control logic (4.12) with $\varepsilon = 0$ - adding and subtracting ΔT = 3 N to two opposite corner cables respectively

Once again, adding the saturation effect to the modified control logic (4.12) using the saturation constant $\varepsilon = 0.09$, we observe that the control efficacy decreased as shown in Figs. 5.44 – 5.46.

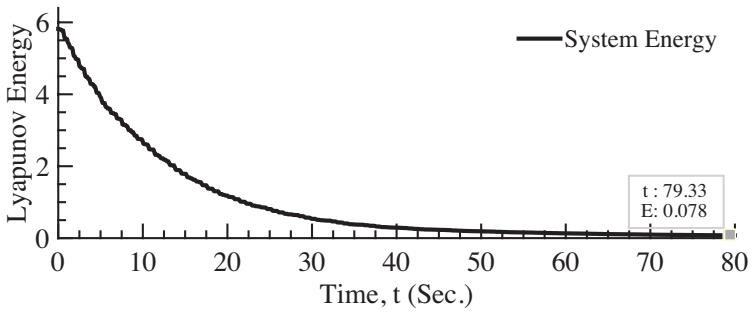

Figure 5.44. Energy dissipation using the modified control logic (4.12) - adding and subtracting ΔT = 3 N to two opposite corner cables respectively

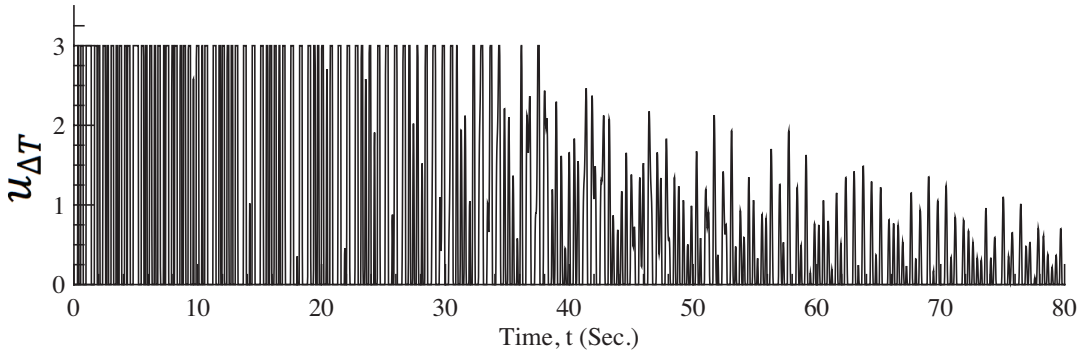

Figure 5.45. Forcing input using the modified control logic (4.12) - adding and subtracting ΔT = 3 N to two opposite corner cables respectively

From Fig. 5.44, we observe that introducing the new configuration reduce the system energy at time t = 79.33 seconds by 34% compared with the previous configuration – see Fig. 5.35. This proves that introducing the in-plane shear forces increase the control efficacy. However, there is no improvement occurred to suppress the first mode.

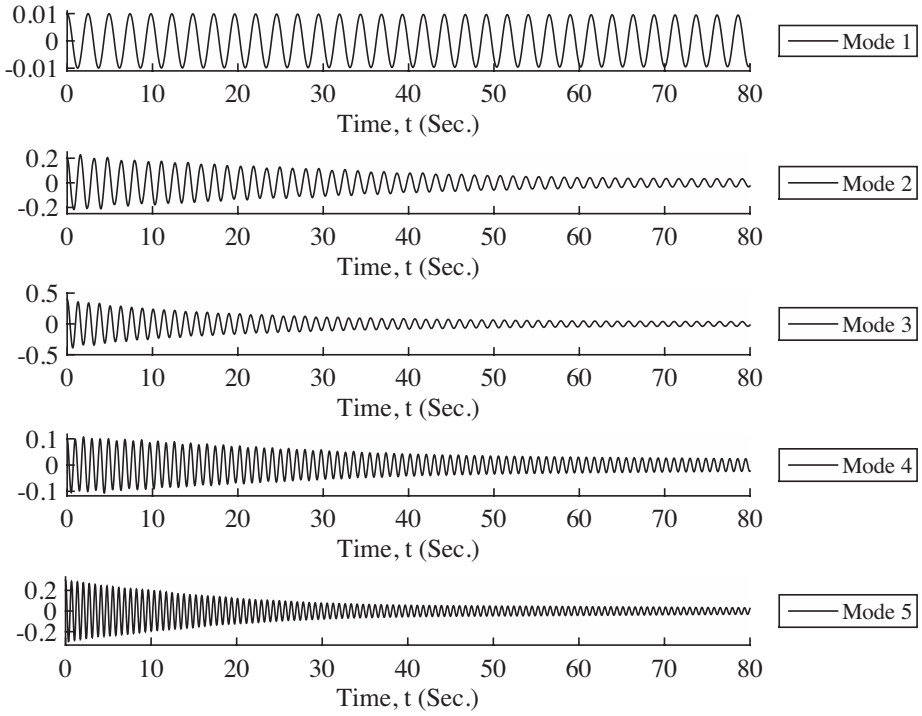

Figure 5.46. Modal displacements using the modified control logic (4.12) - adding and subtracting ΔT = 3 N to two opposite corner cables respectively

5.5.3 Using Multiple ΔT Values With Randomly Switching

In this subsection, we modify the idea of the switching forces by introducing multiple values for the switching forces, ΔT, instead of a single value. This new approach helps in adding lower ΔT force to the system when the higher ΔT force cannot be applied (to do a positive work by removing energy from the system). These multiple ΔT values are; 1, 2, and 3 N that are labeled as ΔT_1, ΔT_2, and ΔT_3 respectively. The control logic (4.7) results are shown in Figs. 5.47 – 5.49 using the initial conditions in (5.113).

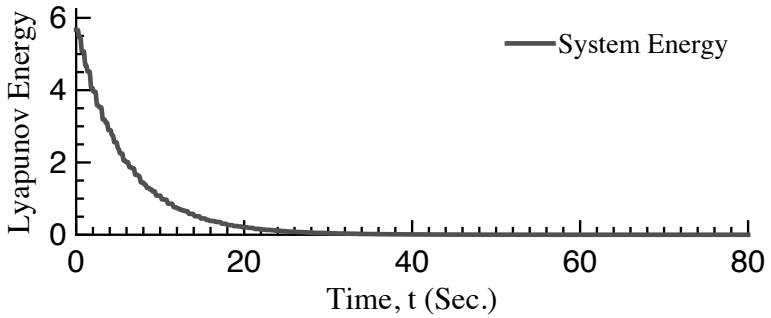

Figure 5.47. Energy dissipation using the control logic (4.7) - multiple ΔT values with randomly switching

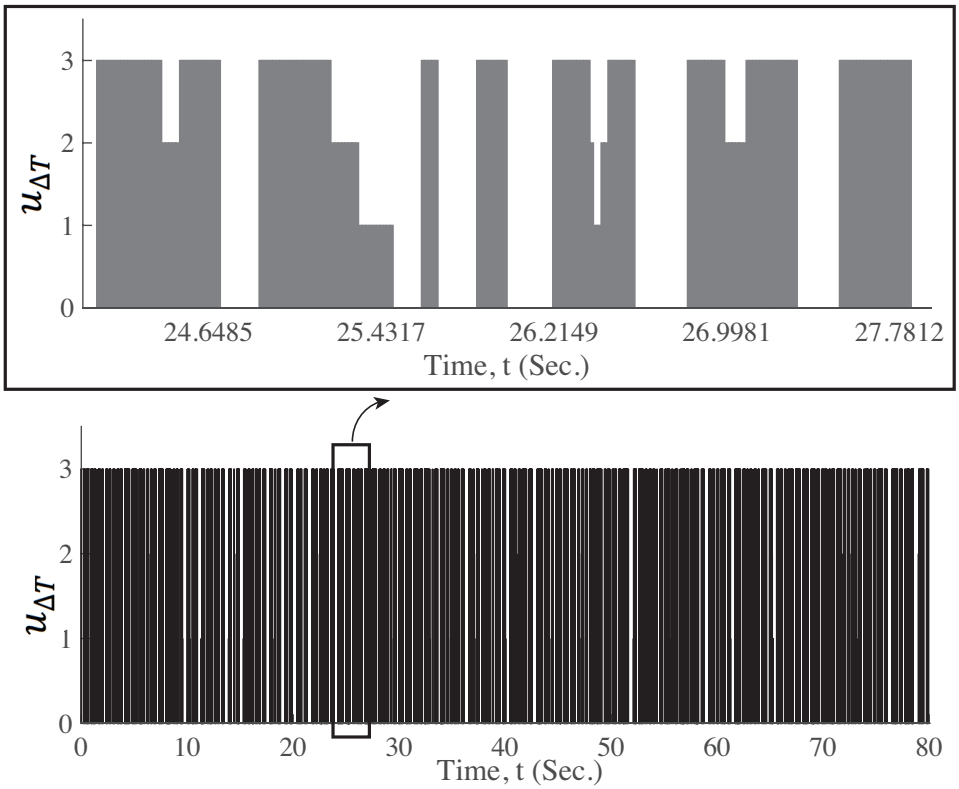

Figure 5.48. Forcing inputs using the control logic (4.7) - multiple ΔT N values with randomly switching

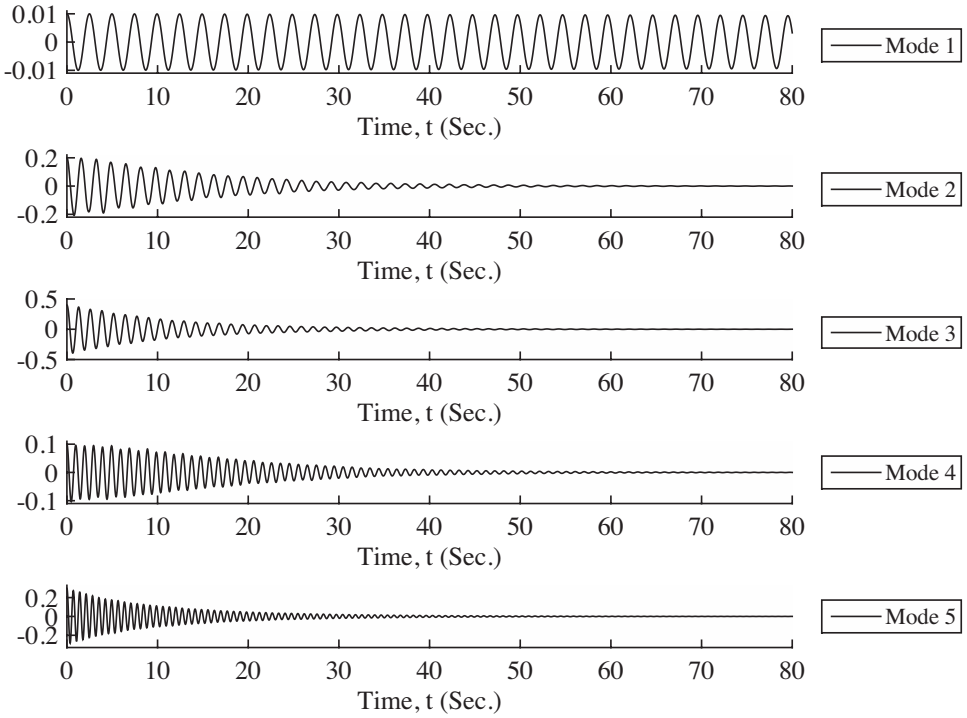

Figure 5.49. Modal displacements using the control logic (4.7) - multiple ΔT values with randomly switching

Form Figs. 5.47 - 5.49, we can observe that the new approach is successfully controlled the vibration and the lower inputs forces (ΔT = 1 and 2 N) are applied when the higher (ΔT = 3 N) value cannot be added. The modified control logic in Equation (4.12) using a low-pass filter with a time constant $\tau = 0.15$ seconds and a saturation with $\epsilon = 0.09$ is then examined and the results are shown in the figures below.

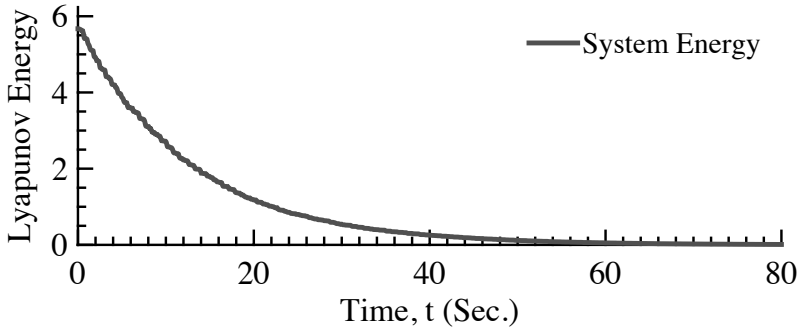

Figure 5.50. Energy dissipation using the modified control logic (4.12) with $\epsilon = 0$ - multiple ΔT values with randomly switching

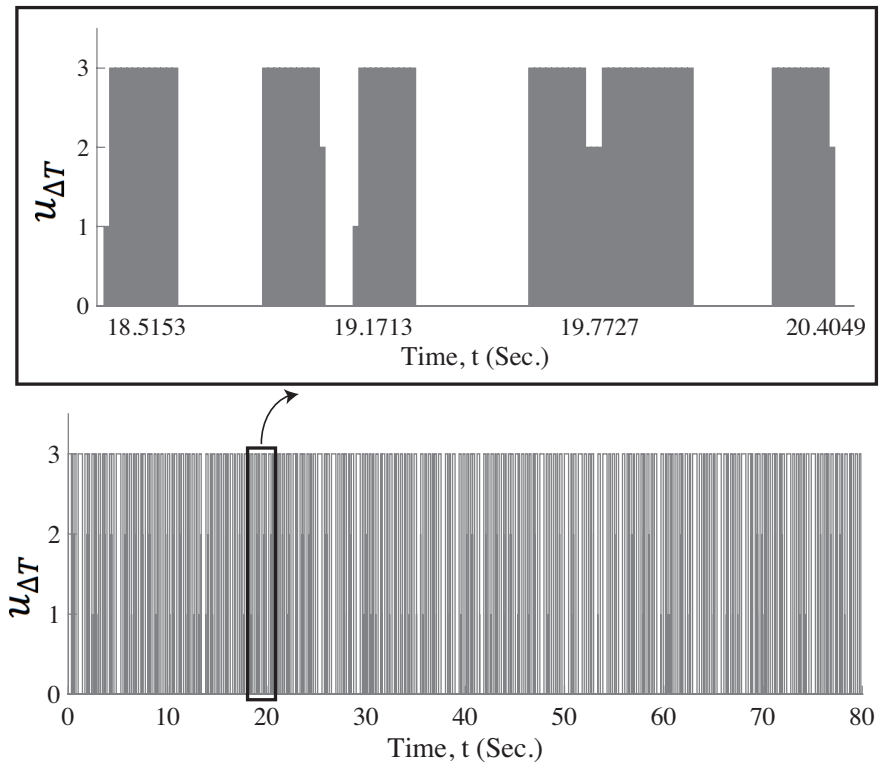

Figure 5.51. Forcing inputs using the modified control logic (4.12) with $\epsilon = 0$ - multiple ΔT N values with randomly switching

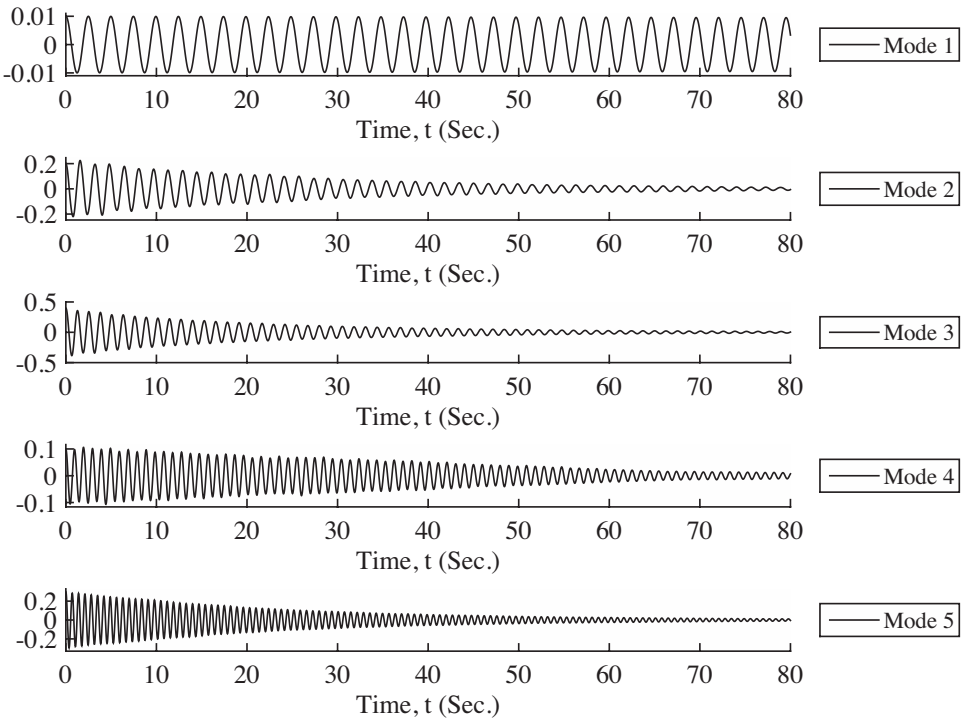

Figure 5.52. Modal displacements using the modified control logic (4.12) with $\epsilon = 0$ - multiple ΔT values with randomly switching

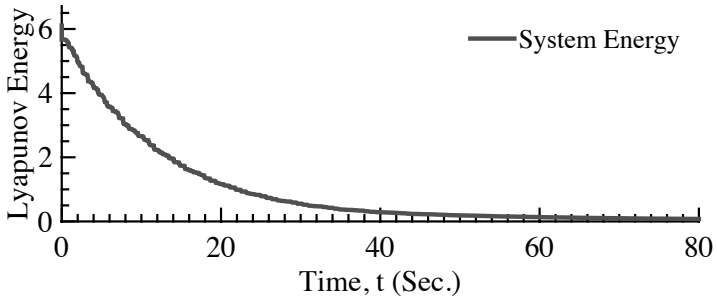

Figure 5.53. Energy dissipation using the modified control logic (4.12) - multiple ΔT values with randomly switching

Comparing Figs 5.53 and 5.35, we can observe that the dissipation of the energy (using multiple ΔT values with randomly switching) is improved. For instance, in previous case (section 5.5.1) the energy at time t = 79.33 seconds was 0.1188, however, using this scheme the energy converged to zero.

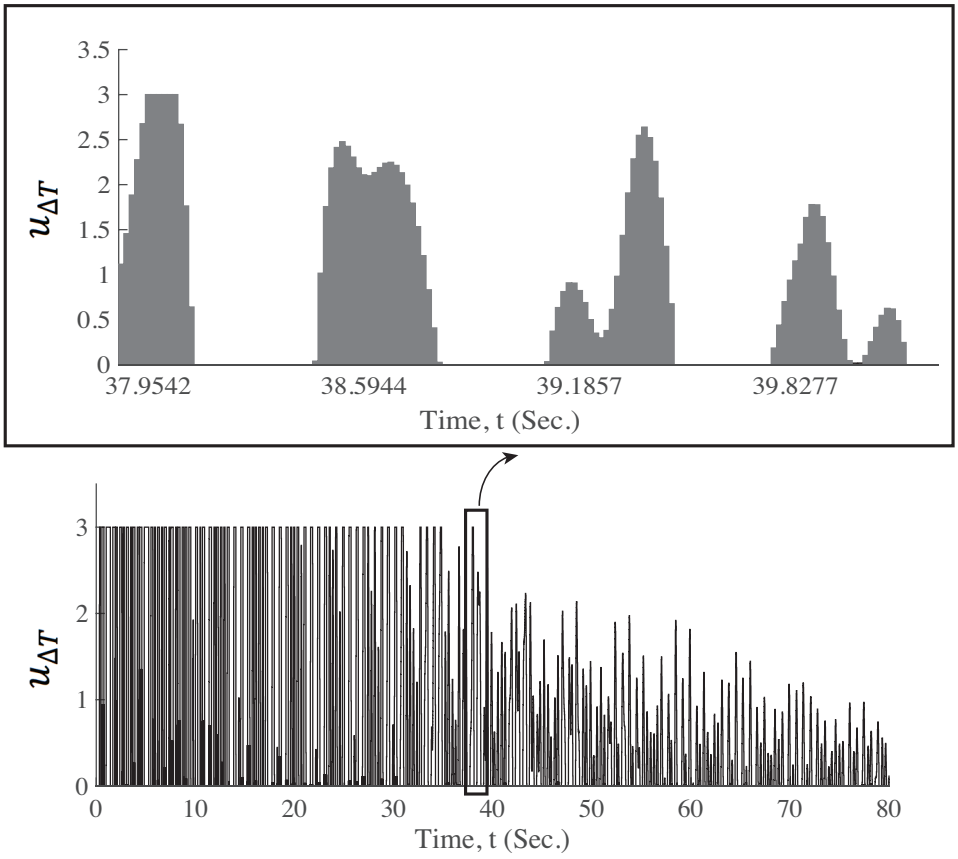

Figure 5.54. Forcing inputs using the modified control logic (4.12) - multiple ΔT N values with randomly switching

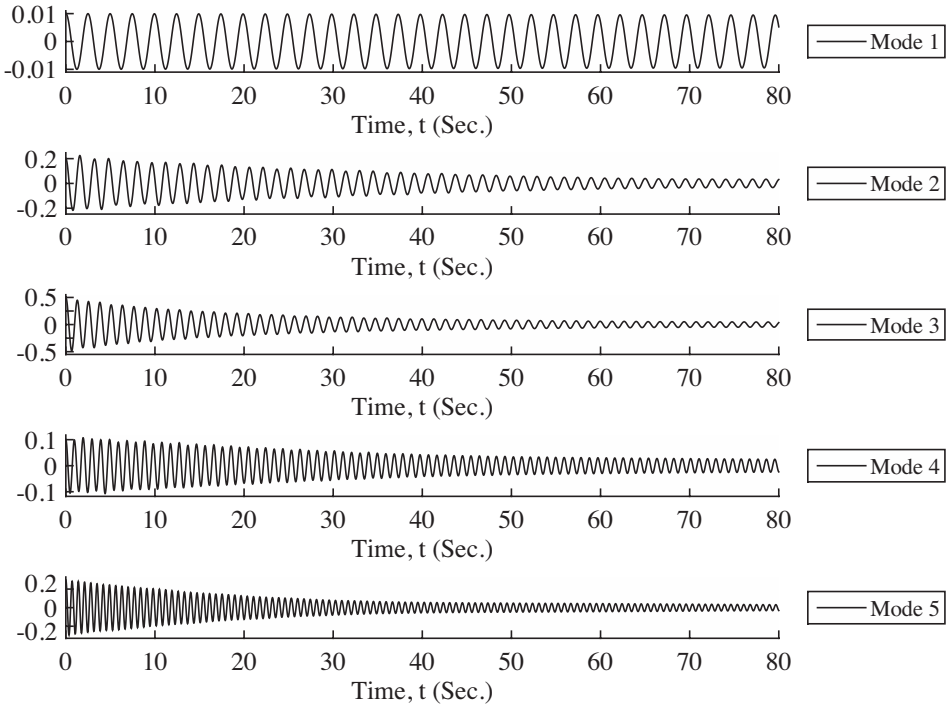

Figure 5.55. Modal displacements using the modified control logic (4.12) - multiple ΔT values with randomly switching

5.5.4 Using Multiple ΔT Values With Systematic Switching

In this subsection, we improve the multiple ΔT values with the random switching approach by introducing a systematic switching between the multiple ΔT values. The new logic is applied to the system starting from ΔT = 0 N and then increased up to ΔT = 3 N with increment equal to 1 N. Then logic starts to decrease ΔT by the same increment until it reaches zero. In addition, between these two increasing and decreasing, the control logic can decrease or increase ΔT based on system need. Therefore, using this new scheme is more convenient in the application because instead of instantaneously switches from ΔT = 0 N to 3 N when the force is needed, the controller performing it gradually with smaller increment until the forces reach its maximum values. To investigate the efficiency of this scheme, a simulation is done using same initial condition and properties as in the previous cases and the results are shown in Figs. 5.56 – 5.64.

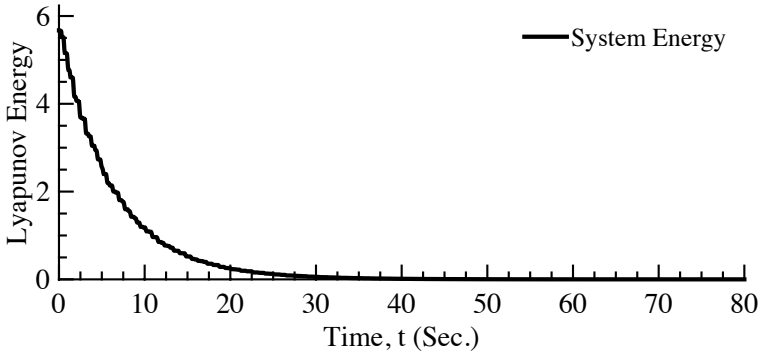

Figure 5.56. Energy dissipation using the control logic (4.7) - multiple ΔT with systematic switching

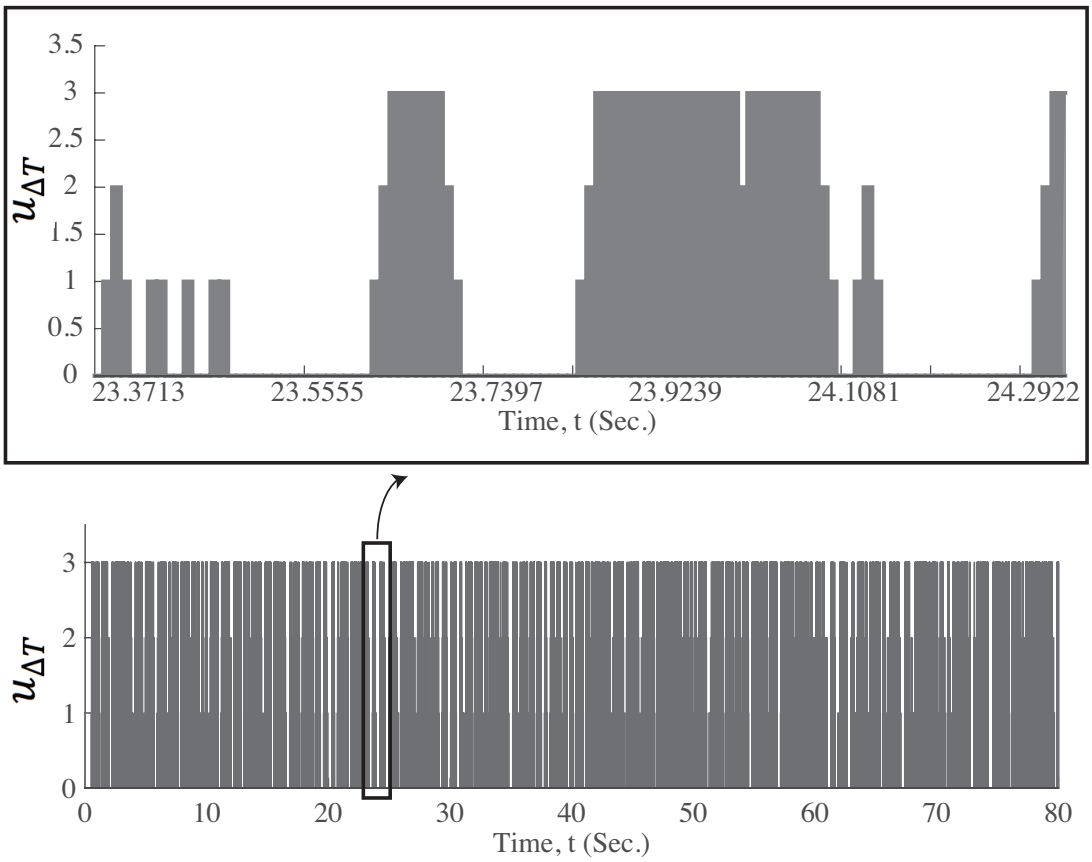

Figure 5.57. Forcing inputs using the control logic (4.7) - multiple ΔT N with systematic switching

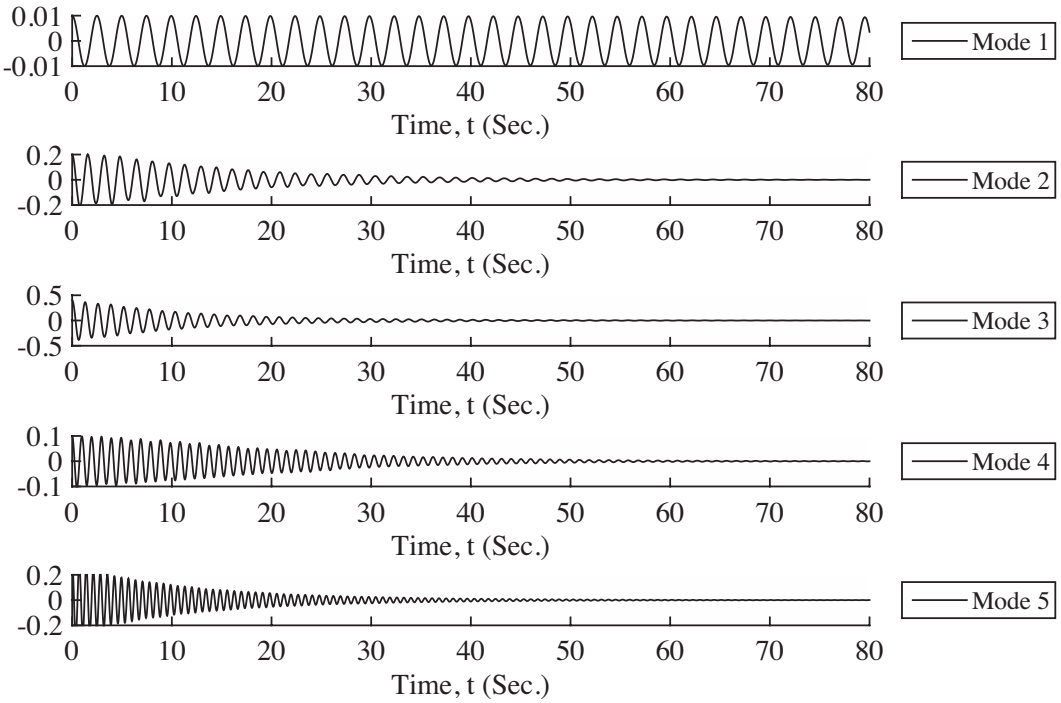

Figure 5.58. Modal displacements using the control logic (4.7) - multiple ΔT with systematic switching

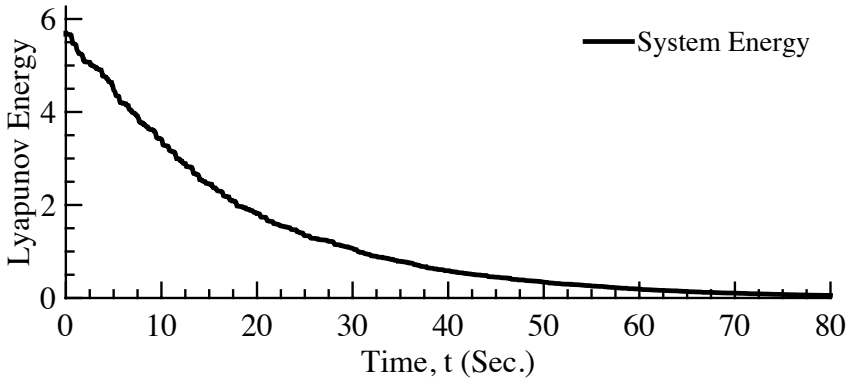

Figure 5.59. Energy dissipation using the modified control logic (4.12) with $\varepsilon = 0$ - multiple ΔT with systematic switching

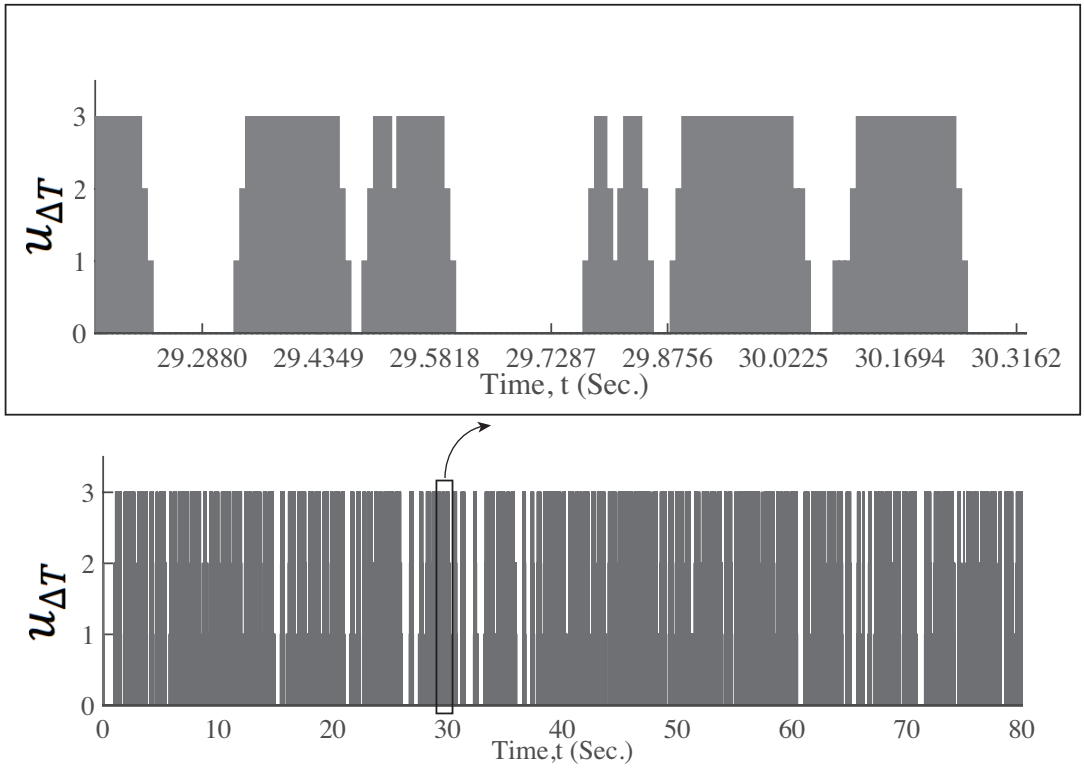

Figure 5.60. Forcing inputs using the modified control logic (4.12) with $\varepsilon = 0$ - multiple ΔT N with systematic switching

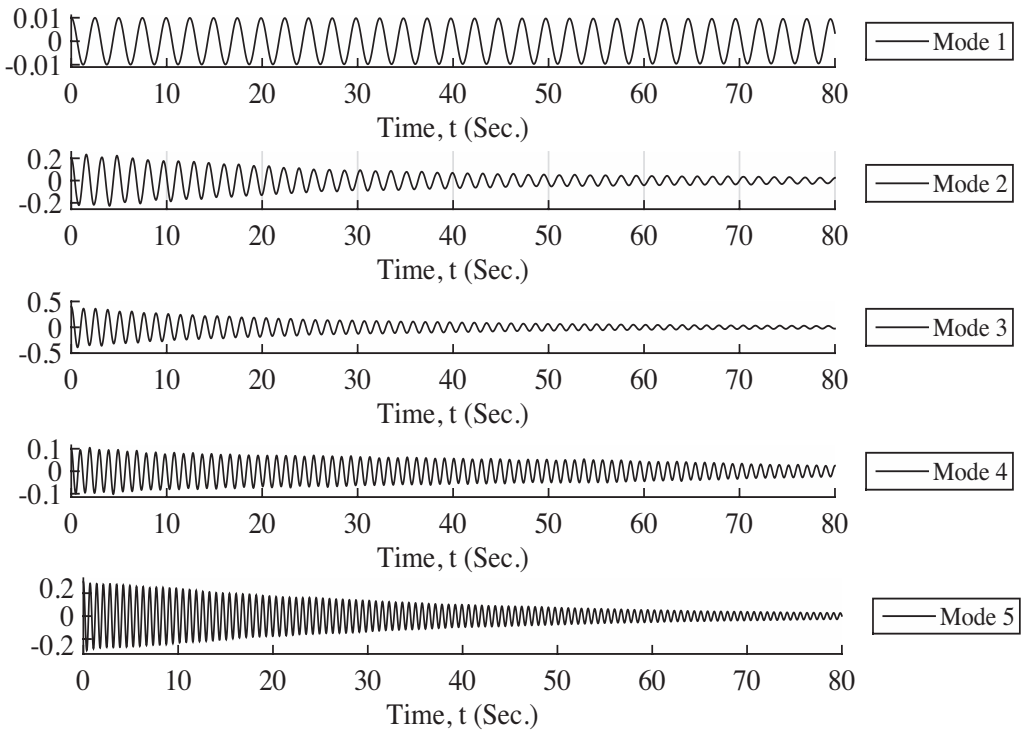

Figure 5.61. Modal displacements using the modified control logic (4.12) with $\varepsilon = 0$ - multiple ΔT with systematic switching

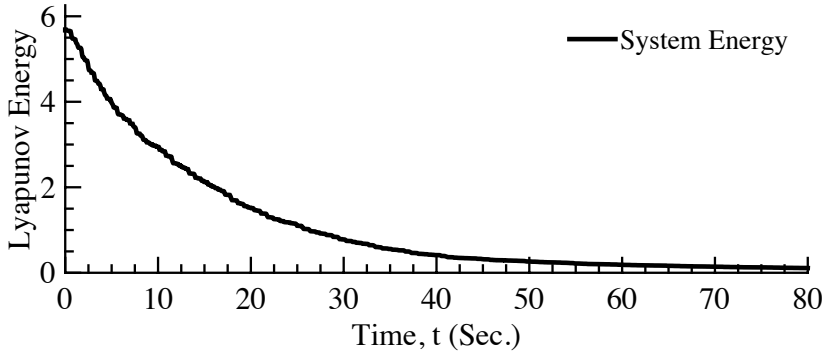

Figure 5.62. Energy dissipation using the modified control logic (4.12) - multiple ΔT with systematic switching

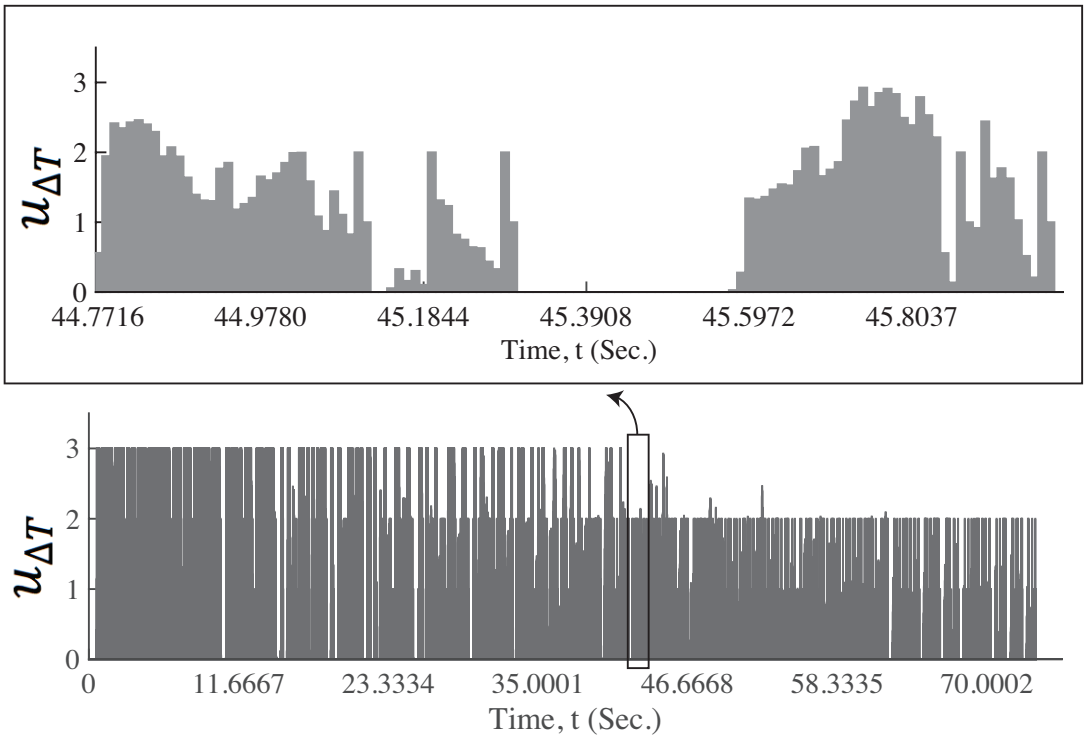

Figure 5.63. Forcing Inputs using the modified control logic (4.12) - multiple ΔT with systematic switching

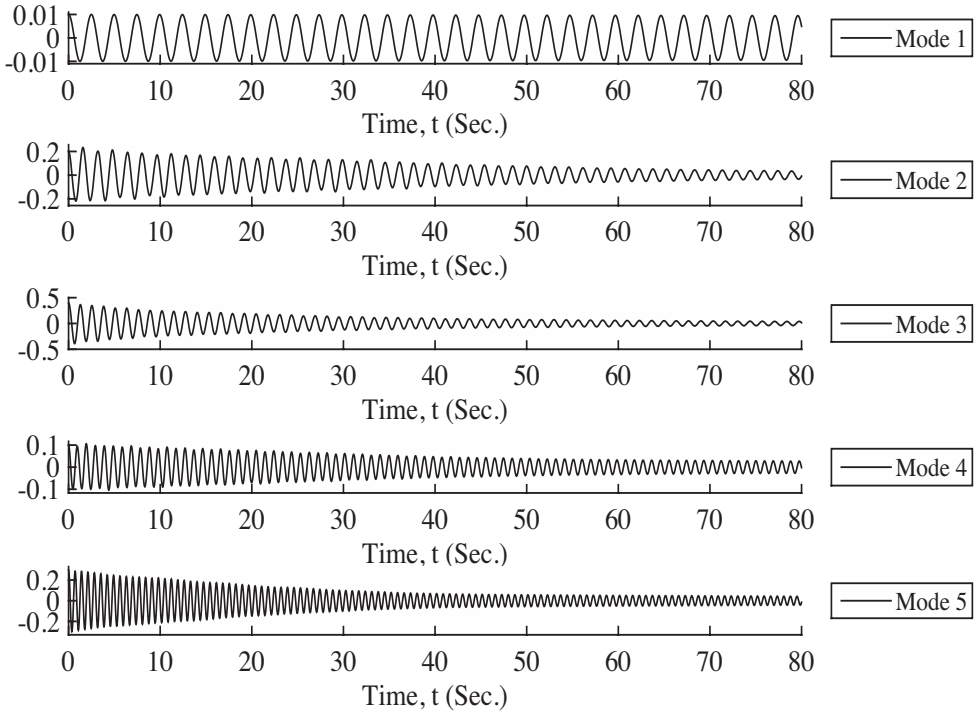

Figure 5.64. Modal displacements using the modified control logic (4.12) - multiple ΔT with systematic switching

From previous results (Figs. 5.56 – 5.64), we observe that the new approach is succeeded in controlling the vibration of the plate with similar performance of the randomly switching scheme. Therefore, we can conclude that using systematic switching with multiple ΔT values is effectively controlling the vibration of the plate. These results can be improved by reducing the value of time constant τ that filters the high frequencies or the saturation constant ϵ to cutoff the added forces.

5.5.5 Summary

The in-plane stress distributions are altered as the in-plane forces applied. As a result, the out-of-plane stiffness matrix is changed (due to the fact that the in-plane stresses can alter the out-of-plane dynamics according to Equations (2.39) and (2.40)), which can be observed from the frequency analysis results (section 5.4). Using this fact, the control logic that is presented in section 4.1 is proposed to use state feedback algorithm to switch the in-plane forces on and off to suppress the vibration.

In this chapter, we propose a web-of-cable structure around the plate as a mechanism to suppress the out-of-plane vibration. Using the control logic introduced in section 4.1, controlling the vibration of the higher modes is proven. However, the first mode could not be suppressed using multiple switching schemes. In the first scheme, a single switching is done by adding ΔT to the corner cables tension, T. The second scheme (adding ΔT to two corner cables and subtracting from the other two corner cables) improves the efficacy of the control strategy, but no sensible improvement on suppression of the vibration of the first mode is observed. Introducing the third and the fourth schemes also does not show any improvement to control the first mode. However, the switching strategy that introduced in both schemes improves the results for the higher modes. Introducing the web-of-cable structure does not control the vibration on the first mode due to the fact that the rate of change in the first mode frequency is not the same as in the higher modes when ΔT is applied to the corner cable tensions – see Table 5.12. These results can be improved by increasing ΔT value that is applied to the corner cables tension or by increasing the number of cables around the boundaries (boundary cables).

Chapter 6

Conclusion

In this work, we extend the approach that was presented in [48] to control the vibration of cantilever beam using end-force to a plate structure using in-plane forces. The underlying goal of the work is to control the vibration of space structures that can be used for space-based image acquisition.

In chapter 2, we reviewed the dynamics of a thin plate without and with in-plane forces. These dynamic equations were derived using the equilibrium approach based on classical plate theory with assumptions similar to those in thin beam or Euler-Bernoulli beam theory. After we presented the dynamics of the plate we introduced a few approaches for vibration analysis in chapter 3. Specifically, we examined two different approximation methods and compared the results with the analytical solution for simply supported boundary conditions. The solutions for the dynamic equations are divided into two parts: the first part assumes that the plate is subjected to uniform stress distributions, in the second part, the plate is assumed to have non-uniform stress distributions.

In chapter 4, we demonstrate a control strategy based on the in-plane uniformly distributed control forces to reduce the lateral vibration of the thin rectangular plate. The control scheme uses state feedback to switch the in-plane forces. These forces were switched on and off

based on a control logic to remove energy from the system. The control scheme was implemented for two different boundary conditions, the simply supported boundary conditions and the elastic boundary conditions; the Rayleigh-Ritz approximation method and FEM were used for vibration analysis. After implementation of the basic control strategy, it was modified by adding a low-pass filter to reduce the bandwidth requirement of the actuator. The control logic is also modified by adding a saturation, which reduces the amount of added forces when the system vibration has reduced below a certain level. After we established the stability of the system mathematically, we verified it by simulating the results for both the unmodified and modified control logic.

In chapter 5, we applied both the unmodified and modified control logic to control the vibration of a thin rectangular plate supported by a web-of-cables structure. The web-of-cables structure connects the thin rectangular plate to four fixed pulleys and provides the in-plane forces that are needed to remove the energy from the plate. To achieve that, we first designed the web-of-cables structure and investigated the deformations that are caused by changing the corner cables tension. After we got the information of the deformed and undeformed web-of-cables structures, we used them to perform the in-plane stress distributions analysis. The pre-stress information was used to carryout the out-of-plane vibration analysis. Finally, from the out-of-plane vibration analysis we derived the dynamic models that are used to perform the control scheme. The control logic in this chapter was applied to control the switching of the corner cables additional tensions, which affects the web-of-cables structure. The web-of-cables structure adds concentrated forces to the edges of the thin rectangular plate, which create a non-uniform stress distribution inside the plate. The control scheme was verified using different cases as follows: increasing the tension of all four corner pulleys, increasing the tension of two corners

and decreasing the tension of the other two, using multiple tension levels with a random switching, and finally using multiple tension levels with systematic switching. Form the simulation results of these cases we were able to show that we successfully controlled the vibration of the higher modes of the thin rectangular plate using the control scheme. However, introducing the web-of-cable structure to suppress the vibration was not successful in suppressing the vibration of the first mode. Clearly, future work will be required to modify the control scheme to suppress the vibration of the fundamental frequency, which has more serious effects on the space-based image acquisition than the high frequencies. For instance, redesign the web-of-cables structure by including more cables around the plate boundaries (boundary cables) worth investigation; it can provide more in-plane forces that can increase the controller efficacy. Another way to increase the effects of the boundary forces on the fundamental frequency can be done by increase the boundary forces magnitude, which can be done by increasing the corner cables tension.

BIBLIOGRAPHY

BIBLIOGRAPHY

[1] Z. Celep, "On the vibration and stability of a free-free beam subjected to end-loads," Journal of sound and vibration, vol. 61, no. 3, pp. 375–381, 1978.

[2] M. Sasaki and S. Chonan, "Vibration and stability of elastically supported circular plates under conservative and non-conservative loads," Journal of sound and vibration, vol. 103, no. 1, pp. 99–108, 1985.

[3] K. Higuchi and E. Dowell, "Dynamic stability of a completely free plate subjected to a controlled non-conservative follower force," Journal of sound and vibration, vol. 132, no. 115-128, 1989.

[4] S. Adali, "Stability of a rectangular plate under non-conservative and conservative forces," Int. J. Solids Structures, vol. 18, no. 12, pp. 1043–1052, 1982.

[5] Q. H. Zuo and H. L. Schreyer, "Flutter and divergence instability of non-conservative beams and plates," Int. J. Solids Structures, vol. 33, no. 9, pp. 1355–1367, 1996.

[6] M. A. Langthjem and Y. Sugiyama, "Dynamic stability of columns subjected to follower loads: a survey," Journal of sound and vibration, vol. 238, no. 5, pp. 809–851, 2000.

[7] G. Skidmore and W. L. H. JR., "Modal-space active damping of beam-cable structure: theory and experiment," Journal of sound and vibration, vol. 101, no. 2, pp. 149–160, 1985.

[8] Y. P. Park, "Dynamic stability of a free Timoshenko beam under a controlled follower force," Journal of sound and vibration, vol. 113, no. 3, pp. 407–415, 1987.

[9] J. H. Kim and J. H. Park, "On the dynamic stability of rectangular plates subjected to intermediate follower forces," Journal of sound and vibration, vol. 209, no. 5, pp. 882–888, 1998.

[10] J. H. Kim and J. H. Park, "Dynamic stability of a completely free circular cylindrical shell subjected to a follower force," Journal of sound and vibration, vol. 231, no. 4, pp. 989–1005, 2000.

[11] M. E. Magana, P. Volz, and T. Miller, "Nonlinear decentralized control of a flexible cable-stayed beam structure," ASME, vol. 119, pp. 523–526, October 1997.

[12] G. Herrmann, "Dynamics and stability of mechanical systems with follower forces," National Aeronautics and Space Administration, Washington, D.C., Novvember 1971.

[13] Arreola-Licas, J. A. Franco-Villafane, G. Baez, and R. A. Mendez-Sanchez, "In-plane vibrations of a rectangular plate: Plane wave expansion modelling and experiment," Journal of sound and vibration, vol. 342, pp. 168–176, 2015.

[14] K. Khorshidi, E. Rezaei, A. A. Ghadimi, and M. Pagoli, "Active vibration control of circular plates coupled with piezoelectric layers excited by plane sound wave," Applied Mathematical Modeling, vol. 39, pp. 1217–1228, 2015.

[15] A. N. Djanan, B. N. Nbebdjo, and P. Woafo, "Electromechanical control of vibration on a plate subjected to a non-ideal excitation," Mechancs Research Communication, vol. 54, pp. 72–82, 2013.

[16] Q. Hu, Y. Jia, and S. Xu, "Dynamics and vibration suppression of space structures with control moment gyroscopes," Acta Astronautica, vol. 96, pp. 232–245, 2014.

[17] Z. Qiu and D. Ling, "Finite element modeling and robust vibration control of two-hinged plate using bonded piezoelectric sensors and actuators," Acta Mechanica Solida Sinica, vol. 27, no. 2, April 2014.

[18] H. Beferani and A. R. Saidi, "Effects of in-plane loads on vibration of laminated thick rectangular plates resting on elastic foundation: An exact analytical approach," European Journal of Mechanics A/Solids, vol. 42, pp. 299–314, 2013.

[19] Kucuk, K. Yildirim, and S. Adali, "Optimal piezoelectric control of a plate subject to time-dependent boundary moments and forcing function for vibration damping," Computers and Mathematics with Application, vol. 69, pp. 291–303, 2015.

[20] S. Carra, M. Amabili, R. Ohayon, and P. M. Hutin, "Active vibration control of a thin rectangular plate in air or in contact with water in presence of tonal primary disturbance," Aerospace Science and Technology, vol. 21, pp. 54–61, 2008.

[21] H. N. Shirazi, H. R. Owji, and M. Rafeeyan, "Active vibration control of an FGM rectangular plate using fuzzy logic controllers," Procedia Engineering, vol. 14, pp. 3019–3026, 2011.

[22] Israr, "Model for vibration of crack plates for use with damage detection methodologies," Jornal of Space Technology, vol. 1, no. 1, June 2011.

[23] E. T. Falanges, J. A. Dworak, and S. Koshigoe, "Controlling plate vibrations using piezoelectric actua- tors," August 1994.

[24] M. H. Hsu, "Vibration characteristics of rectangular plates resting on elastic foundations and carrying any number of sprung masses," International Journal of Applied Science and Engineering, vol. 4, no. 1, pp. 83–89, 2006.

[25] O. N. Ashour, “Nonlinear control of plate vibrations,” Doctor of Philosophy Thesis, January 2001.

[26] J. Kovarova, J. Dupal, and M. Schlegel, “Vibration control of plate structures,” Engineering mechanics, vol. 14, no. 1/2, pp. 23–36, 2007.

[27] Chien-ChingMa and C.-C. Lin, “Experimental investigation of vibrating laminated composite plates by optical interferometry method,” AIAA journal, vol. 39, no. 3, March 2001.

[28] K. Gupta, H. Kaur, and A. Kumar, “Vibration of visco-elastic orthotropic parallelogram plate with linear thickness variation in both directions,” International of Acoustics and vibration, vol. 16, no. 2, 2011.

[29] N. M. Werfalli and A. A. Karound, “Free vibration analysis of rectangular plates using galerkin-based finite element method,” International Journal of Mechanical Engineering, vol. 2, no. 2.

[30] Y. Yaman, T. Caliskan, V. Nalbantoglu, E. Prasad, and D. Waechter, “Active vibration control of a smart plate,” ICAS2002 Congress, 2002.

[31] S. Hatami, M. Azhari, and M. M. Saadatour, “Stability and vibration of elastically supported axially moving orthotropic plates,” Iranian Journal of Science and Technology, vol. 30, no. B4, 2006.

[32] Y. B. Zhao, G. W. Wei, and Y. Xiang, “Plate vibration under irregular internal supports,” International Journal of Solids and Structures, vol. 39, Novvember 2000.

[33] J. H. Williams, E. R. C. Marques, and S. S. Lee, “Modes of vibration on square fiberglass epoxy composite thick plate,” NASA National Aeronautics and Space Administration Scientific and Technical Information Branch, September 1986.

[34] D. Zhou and T. Ji, “Free vibration of rectangular plates with continuously distributed spring-mass,” International Journal of Solids and Structures, Novvember 2005.

[35] P. A. Farrell and T. G. Ryall, “Vibration of a rectangular cantilever plate,” Department of defence science and technology organisation aeronautical research laboratory, 1990.

[36] Frendi, L. Maestrello, and A. Bayliss, “Coupling between plate vibration and acoustic radiation,” NASA Contract Nos. NASI-18605 and NASI-19480, December 1992.

[37] Y. Achkire and A. Preumont, “Active vibration control of cable-stayed bridges,” Earthquake Engineering and Structural Dynamics, vol. 25, pp. 585–597, 1996.

[38] Leissa, Vibration of plates. American Institute of Physics, 1993.

[39] S. S. Rao, Vibration of continous system. Wiley, 2013.

[40] F. Braghin, S. Cinquemani, and F. Resta, "A new approach to the synthesis of modal control laws in active structural vibration control," Journal of Vibration and Control, vol. 19, no. 2, pp. 163–182, 2012.

[41] M. G¨ardsback and G. Tibert, "Deployment control of spinning space webs," Journal of guidance, control, and dynamics, vol. 32, no. 1, 2009.

[42] H. Sakamoto, K. Park, and Y. Miyazaki, "valuation of membrane structure designs using boundary web cables for uniform tensioning," Acta Astronautica, vol. 60, pp. 846–857, 2007.

[43] H. Sakamoto and K. C. Park, "Localized vibration isolation strategy for low-frequency excitations in membrane space structures," Journal of Vibration and Acoustics, vol. 128, pp. 790 –797, 2006.

[44] S. A. Lane and T. W. Murphey, "Overview of the innovative space-based radar antenna technology program," Journal Of spacecraft and rockets, vol. 48, no. 1, January 2011.

[45] S. K. Keon and T. W. Murphey, "Fundamental design of tensioned precision deployable space structure applied to an x-band phased array," American institute of Aeronautics and Astronautics, 2012.

[46] G. Greschik and J. M. Mejia-Ariza, "Error control via tension for an array of flexible square antenna panels," American institute of Aeronautics and Astronautics, 2010.

[47] Preumont and F. Bossens, "Active tendon control of vibration of truss structure: Theory and experiments," Journal of Intelligent Material System and Structure, vol. 11, pp. 91–99, 2000.

[48] S. Nudehi, R. Mukherjee, and S. W. Shaw, "Active vibration control of a flexible beam using a buckling- type end force," Journal of Dynamic Systems, Measurement, and Control, vol. 128, pp. 278–286, June 2006.

[49] F. K. Bogner, R. L. Fox, and L. A. Schmit, Jr., " The Generation of Interelement-Compatible Stiffness and Mass Matrices by the Use of Interpolation Formulas," *proceeding of 1st Conference on Matrix Methods in Structural Mechanics* (AFFDL-TR-66-80), Wright –Patterson Air Force Base, Dayton, OH, 1965.